University of California

Los Angeles

Joint Channel Estimation and Decoding For Wireless Channels

A dissertation submitted in partial satisfaction

of the requirements for the degree

Doctor of Philosophy in Electrical Engineering

by

Christos Komninakis

2000

The dissertation of Christos Komninakis is approved.

Gregory J. Pottie

Ali H. Sayed

Kirby A. Baker

Richard D. Wesel, Committee Chair

University of California, Los Angeles

2000

To my family.

TABLE OF CONTENTS

1 Introduction **1**

1.1 Overview of Wireless Channels 2

1.2 Overview of Dissertation Topics 5

I TURBO-CODES IN FLAT FADING 8

2 Trellis Turbo-Codes and the Forward-Backward Algorithm **9**

3 Flat Rayleigh Fading **15**

3.1 Markov model for the phase 16

3.2 Quantized phase estimation 20

4 Algorithms for Joint Data and Channel Estimation **25**

4.1 Forward-Backward phase estimation 25

4.1.1 Supertrellis algorithm 27

4.1.2 Algorithm on separate trellises 31

4.2 Channel capacity 38

4.2.1 Simplified finite-state Markov channel (FSMC) model 38

4.2.2 Bounds on the capacity of a FSMC 40

4.2.3 Performance in the FSMC relative to capacity 42

5 Diversity Reception in Flat Fading **48**

5.1 Transmission and channel model 49

5.2 General iterative receiver 51

5.2.1 Quantized phase approach 53

5.2.2 Optimum filtering approach 57

5.3 Simulation results 62

5.3.1 Capacity with receiver diversity 64

5.4 Conclusions 67

II MIMO SYSTEMS IN FREQUENCY-SELECTIVE FADING 71

6 MIMO Frequency-Selective Channel 72

6.1 Introduction 72

6.2 MIMO channel model 75

7 Receiver Structure and Performance 81

7.1 Receiver structure 81

7.1.1 Kalman tracking and channel prediction 83

7.1.2 DFE design 85

7.2 Baseline adaptive systems 88

7.3 Simulation results 90

7.4 Coding 96

7.5 Conclusions 101

8 Conclusions and Future Work 102

A Estimation from Pilot Symbols 104

B Proof of Theorem 1 . . . . **108**

References **111**

LIST OF FIGURES

2.1 Generic diagram of parallel trellis turbo-code. 10

2.2 Schematic diagram of the symbol turbo-decoder 14

3.1 Correlation coefficient for the amplitude and the phase of the fading process $\{a_t\}$ for $f_D T = 0.05$. 17

3.2 BER of turbo-code in different $f_D T$, and for estimation vs. perfect knowledge of amplitude fading. 19

3.3 Mean-Squared Error (MSE) of channel estimation for a Rayleigh fading channel with $f_D T = 0.05$ under two scenarios: optimum filtering and knowledge of the correct quantized sector. 24

4.1 Addition of angles in fading 26

4.2 Block diagram of system employing iterative decoder. 27

4.3 Supertrellis and non-iterative pilot filtering performance in Clarke's channel with $f_D T = 0.05$. 29

4.4 The turbo-code used as a running example in this dissertation, with overall rate of 1 bit/sec/Hz. 32

4.5 Transmitter block diagram for pilot-aided turbo-code. 32

4.6 Basic SISO building blocks of the receiver. 33

4.7 Receiver expansion in the processing time axis. 35

4.8 BER of turbo-code, for $f_D T = 0.01$ and for different pilot insertion ratios. 36

4.9 BER of turbo-code, for $f_D T = 0.05$ and for different pilot insertion ratios. 37

4.10 Bounds on C_{FSMC} for i.i.d. 4-PSK inputs. 42

4.11 BER vs. E_b/N_o, for the turbo-code in the FSMC with $K = 8$ quantized phases derived from $f_D T = 0.05$. 43

4.12 Capacity bounds and simulated BER in Markov channel for various pilot insertion rates. 44

5.1 Block diagram of the transmitter in a pilot-aided trellis turbo-coded system. 49

5.2 Flat fading channel with L branches of receiver diversity. 50

5.3 Receiver block diagram for turbo-decoder with diversity and iterative channel estimation. 52

5.4 Transition probabilities for $f_D T = 0.05$ (left) and $f_D T = 0.01$ (right), for $K = 8$ quantized phases. 54

5.5 BER of turbo-code, for $f_D T = 0.01$ for the two channel estimation methods, and given perfect CSI. 63

5.6 BER of turbo-code, for $f_D T = 0.05$ for the two channel estimation methods, and given perfect CSI. 64

5.7 Capacity (with Gaussian inputs) for i.i.d. Rayleigh fading channels with receiver diversity orders of $L = 1$ and $L = 2$. Perfect channel knowledge at the receiver is assumed. 66

5.8 BER performance of turbo-code in flat Rayleigh fading with $f_D T = 0.01$, with diversity orders of $L = 2$ and $L = 1$. 69

5.9 BER performance of turbo-code in flat Rayleigh fading with $f_D T = 0.05$, with diversity orders of $L = 2$ and $L = 1$. 70

6.1 The interfering ISI channels in a $(2, 2)$ MIMO system. 76

7.1 MIMO Receiver block diagram. 82

7.2 MIMO DFE block diagram. 86

7.3 Performance of $(2, 2)$ system vs. SNR in slower channel variation. . . 92

7.4 Performance of $(2, 2)$ system vs. SNR in faster channel variation. . . . 93

7.5 Performance of $(1, 1)$ system vs. SNR in AR(1) channel. 94

7.6 Performance of $(1, 1)$ system vs. SNR, in real Ricean channel with $f_D T = 0.01$. 95

7.7 SNR required for the $(2, 2)$ system to reach SER $= 10^{-3}$ for different channel conditions. 96

7.8 BER performance for the $(2, 2)$ system with three different codes with 8 states. 99

A.1 Collection of the derotated observables corresponding to pilots into the vector $\tilde{\mathbf{y}}$ for $D = 5$, $Z = 3$, $L_0 = 2$. 106

LIST OF TABLES

4.1 Simulation results for the pilot-aided turbo-code in the FSMC derived from $f_D T = 0.05$. 46

Acknowledgments

As this work is coming to an end, I can only remember the good and joyous moments of my graduate life at UCLA. The things I learned, including but certainly not limited to receiver design and channel estimation, the people I met and the friends I made I will cherish forever.

First and foremost, I want to extend my sincere thanks to my advisor, Professor Rick Wesel, for making this period of time a pleasure. Since I joined his research group (as a ”founding member”, so to speak) he has proven to be the best advisor a student could ever hope for, with a passion for good, solid research work, persistence for clear understanding and expression of both the questions and the answers, and a level of energy and optimism that never ceases to amaze me. To those who thought that the birth of his son, Kevin, (pictures of whom he shows prior to every presentation) would slow him down a bit, he replied by almost doubling the size of our group. I cannot thank him enough for the help, the encouragement, and those discussions that boosted my understanding of the problems every single time. I am sure his influence will serve me well in years to come, and wish I can have as rewarding a relationship as I had with him with all the people I work with in the future.

To the older generation of Rick’s group, fellow-students Christina Fragouli, Xueting Liu and Wei Shi, thanks for the cooperation, the help, and the laughs on the sixth floor of the Engineering Building. I wish them all the best for their personal and professional lives. Particularly to Christina, I am grateful for the time we spent together, as well as for the thoughts and discussions we have had, many of which can be found in this dissertation.

To the newest members of the group, Mark Shane, Adina Matache, Cenk Köse and Weidong (Tom) Sun, my best wishes: you are all in good hands, just keep hanging in there.

Sincere thanks also go to the members of my committee, Professors Kirby Baker, Greg Pottie and Ali Sayed, who have taken time out of their busy schedules to attend my Quals and read this dissertation. Professor Pottie's insightful comments on my prospectus helped improve my research work very much, and are greatly appreciated. And Professor Sayed's help and guidance in the second part of this dissertation were invaluable; and his classes on estimation theory were a pleasure to attend. Also, many thanks to Professor Lieven Vandenberghe for helping out on a specific optimization problem and introducing me to non-linear programming.

I have enjoyed working (and taking breaks) in the same building as my friends Peyman Meshkat (best wishes for his new business in Chicago) and Javier Garcia-Frias (good luck in Delaware, with the tenure and the snow). Also, my thanks for the good times to my soccer teammates Erik Berg, John Lach, Curt Schurgers, Mario Novell (also my roomate for a while), Alexis Bernard, Hua Lu, Art Torosyan, Hanli Zhou, Ranny Badra, Scott Siegrist and Matthieu Tisserand.

My good friends in LA, George Kondylis and his wife Tassoula helped me out a lot when I first came to LA; I thank them for that, and wish them good luck at their new home in northern California. To them and to Vaggelis Petsalis, thanks for the many good times and their friendship, as well as for those amazing barbecue weekends. Also, I want to thank my friends Harry Contopanagos and Sissy Kyriazidou, for all their help and sharing the anxiety of the last few months. And to their little daughter Leda, my best wishes.

To my close friends outside of LA, George Papadopoulos in New York and Konstantis Adam in Berkeley, my thanks for putting up with me, both over the phone and in person whenever I was dropping by; I have always appreciated the hospitality. And to my buddies back in Greece, Panos Vassiliadis, Spyros Skiadopoulos, Pavlos Milas and Antonis Valakas, thanks for those emails that kept the group close from thousands of miles apart.

Finally, not much would have been possible in my life without the love and unconditional support I receive from my family, my father Aristidis, my mother Maria and brother George, as well as my grandmother Eirini. I know they are all proud of me right now, and I love them all very much. My happiness associated with the completion of my graduate work is somewhat diminished by the fact that I cannot share it with them. It is to them, my family, that I dedicate this dissertation.

Vita

1972	August 10: Born, Athens, Greece.
1990–1996	B.S. Electrical and Computer Engineering, National Technical University of Athens, Athens, Greece.
1997	Summer Intern, TI-DSP R&D, Texas Instruments, Dallas, TX.
1997–1998	Research Assistant, Electrical Engineering Department, UCLA.
1998	M.S. in Electrical Engineering, University of California at Los Angeles, Los Angeles, CA.
1998–2000	Research Assistant, Electrical Engineering Department, UCLA.
2000	Ph.D. in Electrical Engineering, University of California at Los Angeles, Los Angeles, CA.

Publications

C. Komninakis, C. Fragouli, A. H. Sayed, and R. D. Wesel, "Multi-Input Multi-Output Fading Channel Tracking and Equalization using Kalman Estimation", submitted to *IEEE Transactions on Signal Processing*, November 2000.

C. Fragouli, C. Komninakis, and R. D. Wesel, "Minimality under Periodic Puncturing", submitted to *International Conference on Communications, ICC 2001*, Helsinki, Finland, June 11-15, 2001.

C. Komninakis and R. D. Wesel, “Joint Iterative Channel Estimation and Decoding in Flat Correlated Rayleigh Fading”, accepted to *Journal on Selected Areas in Communications, special issue: The Turbo Principle - From Theory to practice*.

C. Komninakis, C. Fragouli, A. H. Sayed, and R. D. Wesel, “Adaptive Multi-Input Multi-Output Fading Channel Equalization using Kalman Estimation”, in *International Conference on Communications, ICC 2000*, New Orleans, Louisiana, June 18-22, 2000.

C. Komninakis and R. D. Wesel, “Pilot-Aided Joint Data and Channel Estimation in Flat Correlated Fading”, in *Communication Theory Symposium* of *Globecom 99*, Rio de Janeiro, Brazil, December 5-9, 1999.

C. Komninakis, C. Fragouli, A. H. Sayed, and R. D. Wesel, “Channel Estimation and Equalization in Fading”, in *33rd Asilomar Conference on Signals, Systems and Computers*, Pacific Grove, CA, October 24-27, 1999.

C. Komninakis, L. Vandenberge, and R. D. Wesel, “ Capacity of the Binomial Channel, or Minimax Redundancy for Memoryless Sources”, (correspondence) submitted to *IEEE Transactions on Information Theory*, November 2000.

C. Komninakis and R. D. Wesel, “Non-Pilot-Aided Iterative Decoding for Joint Data Recovery and Channel Estimation in Fading” in *33rd Asilomar Conference on Signals, Systems and Computers*, Pacific Grove, CA, October 24-27, 1999.

R. D. Wesel, X. Liu, C. Komninakis, and J. M. Cioffi, “Constellation Labeling for Linear Encoders,” submitted to *IEEE Transactions on Information Theory*, submitted April 1999.

C. Komninakis and R. D. Wesel, “Iterative Joint Channel Estimation and Decoding in Flat Correlated Rayleigh Fading”, in *7th International Conference on Advances in Communications and Control (COMCON)*, Athens, Greece, 28 June-2 July, 1999.

R. D. Wesel, C. Komninakis, and X. Liu, “Towards Optimality in Constellation Labeling”, in the proceedings of the *Communication Theory Mini Conference at Globecom 97*, Phoenix, AZ, November 3-8, 1997.

Abstract of the Dissertation

Joint Channel Estimation and Decoding For Wireless Channels

by

Christos Komninakis

Doctor of Philosophy in Electrical Engineering

University of California, Los Angeles, 2000

Professor Richard D. Wesel, Chair

This dissertation is composed of two main parts. The first and largest part deals with joint phase estimation and turbo-decoding in a flat Rayleigh fading channel. At the region of low SNR where turbo-codes operate, and particularly if the variation of the Rayleigh channel is quite large –i.e., large Doppler– the task of channel estimation becomes quite challenging and should be done jointly with turbo-decoding for better results. To this end, a Markov model is developed for a discretized version of the channel phase (since this is a bigger problem for PSK transmission than amplitude variation) and then the Forward-Backward algorithm is used on the phase trellis implied by this Markov model to acquire the channel phase iteratively, while performing turbo-decoding. Clearly, as the iterations proceed, the reliability of the coded symbols increases, causing them to act somewhat as pilots and facilitate the phase estimation process also.

This channel estimation scheme combines well with spectrally efficient trellis turbo-codes and offers comparable performance to existing pilot averaging techniques at half the bandwidth. To assess the proximity of the performance to channel capacity, upper bounds to the capacity of idealized Markovian channel models are developed, and it is demonstrated that performance as close as 1.3 dB from these upper bounds to capacity without explicit CSI is possible. Also, this technique for iterative quantized phase estimation is extended to the case where antenna diversity is available at the receiver, and the performance improvement due to diversity is shown to be almost as much as the increase in channel capacity.

The second part of this dissertation addresses joint channel estimation and equalization for a general system with n_T transmitter and n_R receiver antennas, impaired by co-channel interference and ISI. A Kalman filter is used to track the frequency-selective channel, which is modeled as a first-order vector autoregressive process. The Kalman filter is aided by delayed decisions from a MIMO m.m.s.e. DFE, which equalizes and decouples the transmitted signals, based on channel estimates received from the Kalman filter. This approach works much better than conventional adaptive algorithms such as LMS and RLS, at the expense of higher complexity. Furthermore, suitable coding options for that equalization and interference cancellation scheme are briefly discussed.

CHAPTER 1

Introduction

Research interest in the field of wireless communications has grown steadily in recent years, and this trend is very likely to continue well into the future. From the physical layer point of view, the goal is to devise schemes and techniques that increase the information rate and improve the robustness of a communication system under the harsh conditions of the wireless environment. The wireless communication channel is the source of various impairments to a digital communication system, due to factors such as the relative mobility of transmitter and receiver, multipath propagation, interference from other users of the frequency spectrum, and time-variation, more commonly known as fading.

In this dissertation, based on widely accepted statistical models for the wireless channel, we explore receiver design and algorithms aimed at combating the detrimental effects of wireless propagation. More specifically, the focus is on two relatively recent advances in communication theory and practice, namely turbo-codes [1] and the use of multiple transmitter and receiver antennas to boost the data rate [2]. Both are treated here from the viewpoint of combining the procedures of channel estimation with the decoding and equalization mechanisms respectively, something that is often overlooked in the literature, relying on the assumption that channel state information is somehow available at the receiver.

While this assumption might be reasonable in operating conditions of slow time-variation and high signal-to-noise ratios (SNR), it is becoming increasingly outdated as more powerful transmission and coding techniques emerge and broadband applications require higher information rates. In those situations of low operating SNR and high spectral efficiency, the channel estimation problem needs to be considered jointly with that of decoding and equalization at the receiver. In particular, the iterative nature of the turbo-decoding algorithm opens the possibility of integrating channel estimation and decoder iterations, such that the two processes can benefit from each other. There is great potential for performance improvement rather than obtaining one-shot channel estimates and keeping the decoding process isolated.

For the problem of multiple antennas, this dissertation provides a solution to improve the equalization and interference cancellation performance by allowing for knowledge of largely invariant channel parameters to aid the estimation process, rather than employing general adaptive equalization algorithms. Based on a first-order autoregressive model for the MIMO channel time-variation, a Kalman filter is used to track the channel and an finite MIMO decision-feedback equalizer (DFE) to equalize it, aided by channel estimates from the Kalman filter and a prediction module.

1.1 Overview of Wireless Channels

For straightforward communication system design, an ideal channel is one that exhibits constant frequency response over the transmission band, and thus produces an undistorted replica of the transmitted signal at the receiver, possibly delayed and scaled. In other words, if the transmitted signal $s(t)$ has an equivalent lowpass frequency representation $S(f)$, occupying total bandwidth W, then the equivalent lowpass frequency response $C(f)$ of an ideal channel is:

$$C(f) = |C(f)| \cdot e^{j\angle C(f)} = C \cdot e^{j2\pi\tau f} \tag{1.1}$$

for all frequencies in the band W of interest. If $s(t)$ goes through the above ideal channel, the received signal will be:

$$r(t) = C \cdot s(t - \tau). \tag{1.2}$$

Of course, real world transmission media, such as the mobile wireless channel, have imperfections, which impair reliable transmission of information. The task of the receiver becomes more complicated when those impairments are *a priori* unknown and/or changing with time. Although the physical phenomena causing signal distortion are very complex and often non-linear, their effects upon the transmitted signal can be quite accurately modeled by a linear, possibly time-variant system. This dissertation uses widely accepted linear, time-varying models of the wireless channel to study various receiver structures, and lumps the effects of thermal and environmental noise into the model as Additive White Gaussian Noise (AWGN).

The challenges posed by the wireless channel to digital communication are mainly due to relative mobility of transmitter and receiver, coupled with multipath propagation. The net effects upon a transmitted pulse in general are dispersion and fading. Dispersion refers to the widening in time of a transmitted pulse, causing it to overlap with pulses transmitted at adjacent times, a phenomenon known as intersymbol interference (ISI). In the frequency domain this occurs when the transmission rate is high enough, such that the transmitted bandwidth exceeds the coherence bandwidth of the channel. So, if the transmission bandwidth is broad enough, the channel is bound to be frequency-selective and thus dispersive. Fading describes the fluctuation of the signal attenuation with time, which can be very severe and is due to motion or other changes in the environment.

Significant time variability is not always associated with dispersion. In fact, at lower transmission rates (narrowband transmission) the channel usually exhibits fast time variation, but little frequency selectivity. This situation is described as flat fading, whereby the channel introduces a time-varying attenuation that affects all frequency components of the transmitted signal equally. For increasing transmission rates, the fading is typically slower with respect to the transmission period, but the channel often becomes dispersive. Hence, in a relatively wideband transmission the channel frequency response varies with frequency across the bandwidth of the digitally modulated signal (as well as in time), causing slowly time-varying ISI between adjacent symbols, in what is called frequency-selective fading.

In broad terms, the time variability of a flat fading wireless channel depends on the relative velocity between transmitter and receiver or moving scatterers in the environment, with respect to the transmission rate. A common way to quantify this is to refer to the Doppler rate $f_D T$, which is defined as the product of the maximum Doppler frequency shift (f_D) experienced by a mobile receiver and the transmission symbol period T. Equivalently, this is the ratio of f_D to the transmission baud rate.

Higher Doppler rates lead to faster varying channels, where the time correlation between successive channel gains is smaller. Thus, the channel gain becomes less than a specified level more often but stays at this low level (a fade) for a shorter time duration. On the one hand, this increases the *time diversity* of the channel, which can be exploited with coding and interleaving, because in a given time interval more independent looks at the channel are available. On the other hand, faster variation makes the task of channel estimation all the more difficult, particularly in a high-noise environment, in which powerful channel codes –such as turbo-codes– operate. In the limit of independent channel coefficients no estimation is possible.

For a frequency-selective fading channel the problem of time-variation, although still significant, becomes less critical for two main reasons. First, as explained before, the time-variation is usually slower with respect to the transmission rate. Second, one more source of diversity, *frequency diversity* is available in this case, since different parts of the transmitted power spectrum experience different attenuation due to the frequency selective channel. One means to exploit frequency diversity is equalization, whereby the goal of the receiver is to intelligently combine information carried by all taps of the linear filter modeling the channel. When those taps are also time varying, the equalizer has to adapt as the channel changes. Hence, for equalization of a time-varying frequency-selective channel to be effective, accurate channel estimation and tracking is required.

1.2 Overview of Dissertation Topics

In accordance with the basic distinction between flat and frequency-selective fading channels outlined in the previous section, this dissertation consists of two main parts. The first deals with joint channel estimation and turbo-decoding in a flat fading channel, and discusses ways to achieve reliable communication at rates close to channel capacity, both with and without antenna diversity at the receiver. The second part considers tracking and equalization (and, briefly, coding) for a frequency-selective multi-input multi-output (MIMO) Ricean channel, whereby one or more antennas are employed at the transmitter and receiver.

Chapter 2 briefly reviews symbol interleaved trellis turbo-codes and the Forward-Backward algorithm used to decode them. This algorithm is a powerful tool that can also be applied to estimation problems based on an appropriate hidden Markov model (HMM). Chapter 3 introduces a widely accepted statistical model for the frequency-flat Rayleigh fading channel encountered in narrowband transmission in a rich scattering environment. Identifying acquisition of the channel phase as a more significant problem for PSK turbo-codes than amplitude fading leads to the introduction of a Markov model that approximates both the values and the statistical properties of the fading phase. Then, it is possible to construct a trellis representing this Markov phase model, with states representing intervals of the continuous channel phase.

Building on those premises, Chapter 4 discusses algorithms for joint phase estimation and turbo-decoding, using an adapted version of the Forward-Backward algorithm as the phase estimation tool. Two main classes of algorithms are described and simulated in various flat Rayleigh fading channels: a computationally intensive supertrellis, combining the channel and code trellises into a supertrellis, and a more effective approach based on separate trellises that describe the channel and the constituent codes. Performance is evaluated via simulation and also assessed in an absolute sense with respect to channel capacity. For this purpose a sequence of progressively tighter upper bounds on the constrained capacity of a purely Markov simplification to the Rayleigh fading channel is derived, and performance of a turbo-code with joint iterative channel estimation and decoding is demonstrated to approach these capacity bounds.

Chapter 5 extends the algorithms for joint phase estimation and turbo-decoding to the case where antenna diversity of order L is available at the receiver. Performance is assessed via simulations, and compared against performance achieved with iterative optimum filtering for channel estimation. The discussion is again limited to flat Rayleigh fading channels, and the performance gain due to receiver spatial diversity is found to match the gain promised by the capacity improvement.

Finally, the second part of the dissertation (Chapters 6 and 7) addresses the problem of channel tracking and equalization for multi-input multi-output (MIMO) time-variant frequency-selective channels. These channels model the corrupting effects of intersymbol interference (ISI), co-channel interference (CCI), and noise. Chapter 6 derives a first-order autoregressive model to describe the MIMO channel variation, such that tracking can be performed by a Kalman filter.

Chapter 7 describes the proposed receiver, in which hard decisions to aid the Kalman tracking algorithm come from a MIMO finite-length minimum-mean-squared-error decision-feedback equalizer (MMSE-DFE), which performs the equalization task. Since the optimum DFE for a wide range of channels produces decisions with a delay $\Delta > 0$, the Kalman filter tracks the channel with a delay. A channel prediction module bridges the time gap between the channel estimates produced by the Kalman filter and those needed for the DFE adaptation. The proposed algorithm offers good tracking behavior for multi-user fading ISI channels at the expense of higher complexity than conventional adaptive algorithms. The coding problem for such a transmission scenario is also briefly discussed. Applications include synchronous multiuser detection of independent transmitters, as well as coordinated transmission through many transmitter/receiver antennas, for increased data rate.

Finally, Chapter 8 discusses how the work in both parts of this dissertation connects with various areas of active research in the field of communication theory, particularly in recent years. Also, the future work that will greatly enhance the results herein is outlined.

The main contributions of the work presented in this dissertation are:

- A Markov model for the channel phase of a flat Rayleigh fading channel.
- Two algorithms for joint iterative phase estimation and turbo-decoding, also applicable when receiver diversity is available.
- A sequence of upper bounds on the capacity of systems with pilot assisted phase estimation, based on the Markov phase model above.
- An algorithm for channel tracking and equalization of frequency-selective, multiple-input multiple-output (MIMO) channels, based on Kalman estimation and finite length MIMO MMSE DFE.

Part I

TURBO-CODES IN FLAT FADING

CHAPTER 2

Trellis Turbo-Codes and the Forward-Backward Algorithm

Since their introduction [1] in 1993, parallel concatenated codes (in short “turbo-codes”) and their variants, such as serially concatenated codes, have captured the interest of the coding community and are being incorporated in the next generation of standards. This is due to their impressive error correcting capabilities with reasonable complexity, offering reliable communication within fractions of a dB from channel capacity, at least in the AWGN channel [3], and in the perfectly interleaved, ideally phase-coherent flat Rayleigh fading channel [4]. This dissertation examines the performance of turbo-codes in flat Rayleigh fading, without assuming knowledge of the channel at the receiver.

In particular, in an effort to achieve high spectral efficiency, this dissertation concentrates on trellis turbo-codes. In other words the transmitted signals are selected from constellations of higher cardinality than BPSK. For completeness, Fig. 2.1 shows a schematic diagram of a symbol-interleaved trellis turbo-code, designed following the guidelines in [5].

The symbol interleaved turbo-codes used in this dissertation are special cases of the diagram in Fig. 2.1. Whether a connection is active or not is determined by exhaustive computer searches over all possible constituent encoders, as described in [5] and [6], where tables of good constituent codes are given. The conventions about naming the

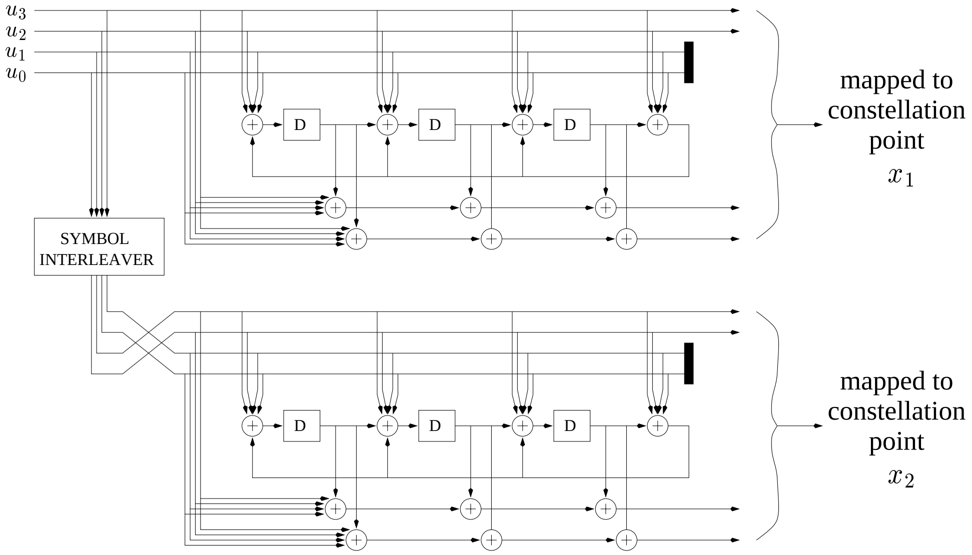

u_3
u_2
u_1
u_0
D
D
D
SYMBOL INTERLEAVER
mapped to constellation point x_1
D
D
D
mapped to constellation point x_2

Figure 2.1: Generic diagram of parallel trellis turbo-code. Which of the connections shown are active is the subject of constituent encoder design. Notice that for an even number of input bits, flipping two groups of bits after symbol interleaving permits to use the *same* constituent code at both the upper and lower encoder. In this way, different bits are punctured in both encoders, thus all bits are systematic only once.

octal polynomials that describe the constituent codes are discussed in [7]. The main point of this symbol-interleaved design for high spectral efficiency turbo-codes is to preserve the order of the input bits $u_0, \ldots, u_{k-1}$ and interleave them as a group, or, in other words as a symbol $u \in$ GF(2^k), hence the symbol interleaver. After each constituent encoder, the output bits are mapped to a constellation point x, which is then transmitted through the channel.

Because of the symbol-oriented description of those trellis turbo-codes, the constituent decoders (Soft-Input Soft-Output modules, –SISO– in [8], [9]) exchange extrinsic information about symbols $u = [u_0, u_1, \ldots, u_{k-1}]$ (and not bits $u_0, \ldots, u_{k-1}$) through the interleaver/deinterleaver pair. So, the soft information $P(u; I)$ and $P(u; O)$ exchanged between the decoders with symbol turbo-decoding (see Fig. 2.2) is in vector form, because the symbols $u \in \mathrm{GF}(2^k)$ can take more than two values. In bit decoding, scalars are enough to convey the log-likelihood ratio of each bit $u_i \in \mathrm{GF}(2)$. It can be shown that symbol decoding is exactly equivalent to the bit-oriented decoding of trellis turbo-codes described in [7], but devoid of the additional assumption that bits within a symbol $u \in \mathrm{GF}(2^k)$ are conditionally independent given the whole observed sequence. The absence of this implicit assumption in symbol turbo-decoding generally improves performance [10], while the coding scheme of Fig. 2.1 eliminates puncturing constraints placed on the constituent encoders and interleaver by [11].

In any case the basic tool for decoding is the Forward-Backward algorithm [12], which is briefly described below. In its initial form in [12] this algorithm provides maximum *a posteriori* (MAP) decoding of trellis codes, but its iterative use for the decoding of turbo-codes has revived interest in it as a powerful estimation tool, not only for codes but also for any hidden Markov model (HMM —see [13] and [14]). It is an algorithm that operates on blocks of data.

Specifically, given the whole sequence y_1^N of N observations $\{y_t\}_{t=1,\dots,N}$ from an HMM with inputs u, states $S \in \mathcal{S} = \{m : \; m = 0, 1, \dots, |\mathcal{S}| - 1\}$ and outputs x (the y's can be noisy observations of the coded symbols x from a code with inputs u), the posterior probability of the input symbol u_t at every time instant t is:

$$
\begin{aligned}
P(u_t = u | y_1^N) &= G \cdot P(u_t = u, y_1^N) = && (2.1)\\
&= G \cdot \sum_{(m',m) \in E(u)} P(S_{t-1} = m', S_t = m, y_1^N) && (2.2)\\
&= G \cdot \sum_{(m',m) \in E(u)} \Bigg\{ \underbrace{P(S_{t-1} = m', y_1^{t-1})}_{\alpha_{t-1}(m')} \cdot \underbrace{P(S_t = m, y_t |\, S_{t-1} = m')}_{\gamma_t(m',m)} \cdot \\
&\qquad \underbrace{P(y_{t+1}^N |\, S_t = m)}_{\beta_t(m)} \Bigg\} && (2.3)
\end{aligned}
$$

where G is an irrelevant constant $G = 1/P(y_1^N)$, and:

$$E(u) = \{(m', m) : \exists \text{ state transition } (S_{t-1} = m' \rightarrow S_t = m) \text{ with input } u_t = u\} \tag{2.4}$$

is the set of transitions between states that produce the desired input symbol u. For $t = 1, \ldots, N$, and for $m = 0, 1, \ldots, |\mathcal{S}| - 1$, the "forward" variables $a_t(m)$ and the "backward" variables $\beta_t(m)$ are computed through the recursions:

$$\alpha_t(m) = \sum_{m'} \alpha_{t-1}(m') \cdot \gamma_t(m', m) \tag{2.5}$$

$$\beta_t(m) = \sum_{m'} \gamma_{t+1}(m, m') \cdot \beta_{t+1}(m'), \tag{2.6}$$

For the above recursions, knowledge of the initial and final states S_0 and S_N is needed. Thus, for every N-symbol block, the encoder is forced to terminate at the zero state, which implies that for every block it is $S_0 = S_N = 0$. Therefore, the following initialization of the forward and backward variables is necessary for the recursions:

$$\alpha_0(m) = \Pr(S_0 = m) = \begin{cases} 1 & \text{if } m = 0 \\ 0 & \text{otherwise} \end{cases} \tag{2.7}$$

In a similar fashion:

$$\beta_N(m) = \Pr(S_N = m) = \begin{cases} 1 & \text{if } m = 0 \\ 0 & \text{otherwise} \end{cases} \tag{2.8}$$

For a single trellis code, (2.1) can be used to perform MAP decoding, but in the iterative decoding of turbo-codes, sketched in Fig. 2.2, certain modifications are necessary to preserve the independence of information used by constituent decoders as much as possible. For straightforward MAP decoding of the symbol u_t it is enough to identify the u that maximizes the quantity:

$$\sum_{(m',m) \in E(u)} \alpha_{t-1}(m') \cdot \gamma_t(m', m) \cdot \beta_t(m). \tag{2.9}$$

For the forward and backward recursions [9] for the α's and β's respectively, the crucial quantity to be computed is:

$$\begin{aligned}
\gamma_t(m', m) &= \Pr\left(S_t = m, y_t \mid S_{t-1} = m'\right) \\
&= \Pr\left(S_t = m \vert\, S_{t-1} = m'\right) \cdot \Pr\left(y_t \mid S_t = m, S_{t-1} = m'\right) \quad (2.10) \\
&= \Pr\left(u \ : \ S_{t-1} = m' \rightarrow S_t = m\right) \cdot \Pr\left(y_t \mid x(m' \rightarrow m)\right), \quad (2.11)
\end{aligned}$$

where $x(m' \rightarrow m)$ is the output symbol of the code (or, in general, the noiseless observable of the Hidden Markov Model) corresponding to the state transition $m' \rightarrow m$. Eq. (2.11) shows that $\gamma_t(m', m)$ is essentially the product of the probability of the state transition and the probability of the observation given that the state transition took place. When the algorithm is used iteratively, as in Fig. 2.2, the first part of (2.11) is the *extrinsic* probability about the input, denoted $P(u; I)$ in the literature [3] and provided by the other constituent decoder.

While for MAP decoding of a single code, the same $\gamma_t(m', m)$ (including the *a priori* input probability term $P(u; I)$) is used both for the recursions (2.5)-(2.6) and for the MAP decision (2.9), iterative symbol decoding of turbo-codes works differently: $P(u; I)$ is included in the $\gamma_t(m', m)$ used to perform the recursions (2.5)-(2.6), but is omitted when producing the updated extrinsic probability $P(u; O)$ to be fed to the other decoder. This is given by:

$$P(u; O) = \sum_{(m', m) \in E(u)} \alpha_{t-1}(m') \cdot \tilde{\gamma}_t(m', m) \cdot \beta_t(m), \quad (2.12)$$

where $\tilde{\gamma}_t(m', m) = \Pr\left(y_t \mid x(m' \rightarrow m)\right)$. This avoids direct circulation of the same soft information between the two constituent decoders.

Finally, note that for reasons of computational complexity and numerical stability in practice the algorithm is not used in its multiplicative form outlined above. Instead, logarithms of the quantities α, β and γ are used, and this allows additions to replace

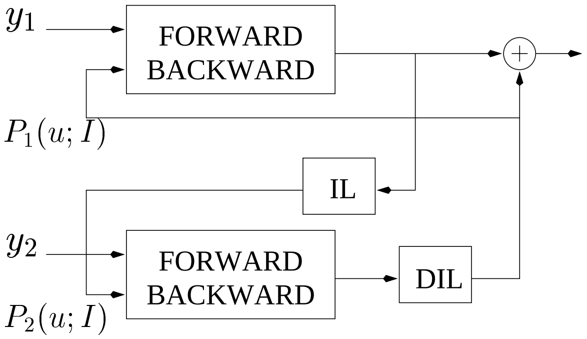

Figure 2.2: Schematic diagram of the turbo decoder, using two Forward-Backward algorithms (SISO modules in [9]) exchanging soft information about the input u to the encoder, through a uniform interleaver and a deinterleaver. At the end of the iterations, the extrinsic information produced by the two SISOs is added and the u with the maximum sum is decoded.

multiplications and the $\max^*$ operation to replace summation. The $\max^*$ operation is defined as:

$$\max^*\{z_1, z_2\} = \max(z_1, z_2) + \log\left(1 + e^{-|z_1 - z_2|}\right). \tag{2.13}$$

The additive correcting function $\log\left(1 + e^{-|z_1 - z_2|}\right)$ applied to the result of the plain $\max$ operation can be omitted with a small degradation in performance [3]. In this case, the algorithm is only performing operations known as add-compare-select, which have very efficient hardware implementations. In all simulations presented in this dissertation we use the symbol-oriented Forward-Backward algorithm described in this chapter, and specifically the additive version of the algorithm with the $\max^*$ operation of (2.13).

CHAPTER 3

Flat Rayleigh Fading

A widely accepted statistical model for non-dispersive wireless fading channels has been introduced in [15], and is commonly referred to as Clarke's fading model. According to this model, after matched filtering and proper sampling, the discrete representation of the received signal at time t is:

$$y_t = a_t \cdot x_t + n_t,\ t = 0, 1, 2, \dots \tag{3.1}$$

where x_t is the transmitted constellation point (in this chapter from an M-PSK constellation), $\{n_t\}$ is an i.i.d. (white) complex Gaussian noise process, with variance $\sigma^2 = N_o/2$ per dimension, and $\{a_t\}$ is the correlated channel fading process, modeled as a circular complex Gaussian random process. This model assumes absence of line of sight (worst case fading) and a continuum of scatterers in the vicinity of the omnidirectional mobile receiver antenna, in other words a rich scattering environment.

Under those conditions, the channel coefficient at time t is $a_t = X_t + jY_t = |a_t|e^{j\phi_t^a}$, where $\{X_t\}$ and $\{Y_t\}$ are mutually uncorrelated, zero-mean Gaussian processes, each with correlation properties determined by the Doppler frequency f_D, see [16]:

$$R_c(\tau) = E[X_t X_{t+\tau}] = E[Y_t Y_{t+\tau}] = \gamma^2 \mathcal{J}_o(2\pi f_D \tau) \tag{3.2}$$

where $\mathcal{J}_o(\cdot)$ is the zero-order modified Bessel function of the first kind, and $\gamma^2 = 0.5$ for normalized power. This autocorrelation gives rise to the well-known U-shaped normalized power spectral density in Jakes [17]:

$$S_{xx}(f) = S_{yy}(f) = \begin{cases} \dfrac{1}{2\pi f_D T} \dfrac{1}{\sqrt{1 - \left(\dfrac{f}{f_D T}\right)^2}}, & |f| < f_D T \\ 0, & \text{otherwise} \end{cases} \tag{3.3}$$

If $\{X_t\}$ and $\{Y_t\}$ are zero-mean (worst case—no line of sight), the marginal distributions of $|a_t|$ and ϕ_t^a are Rayleigh and uniform respectively, hence the term "Rayleigh fading". Specifically, the marginal pdf of the phase is $P_{\phi^a}(\phi) = 1/2\pi$, for $\phi \in [-\pi, \pi)$, while the amplitude marginal pdf for normalized unit power is $P_{|a|}(r) = 2r\, e^{-r^2}$, for $r \geq 0$.

3.1 Markov model for the phase

Clarke's model for the channel fading process is realistic and has been found to quite accurately match field measurements of physical channels. However, the autocorrelation properties of the amplitude process $\{|a_t|\}$ and, mainly, the phase process $\{\phi_t^a\}$, which poses the primary problem in PSK transmission, are non-Markovian and hence difficult to analyze and exploit with the Forward-Backward algorithm. Based on the spectrum of (3.3), the correlation coefficient $\rho_{|a|}(\tau)$ for the fading amplitude and $\rho_{\phi^a}(\tau)$ for the phase of the fading process $\{a_t\}$ are shown in Fig. 3.1. Observe that the autocorrelation is decreasing with the time-lag, as expected, but not in an exponential fashion, as in a truly Markov process.

To utilize the power of the Forward-Backward algorithm in estimation we derive a suitable finite-state Markov model for the channel phase, depending on the Doppler rate $f_D T$, similar to the one in [18] for the fading amplitude. The issue of whether approximating Clarke's fading process [17] with a first-order Markov process is reasonable or not was answered in the affirmative in [19] for the fading amplitude, but the

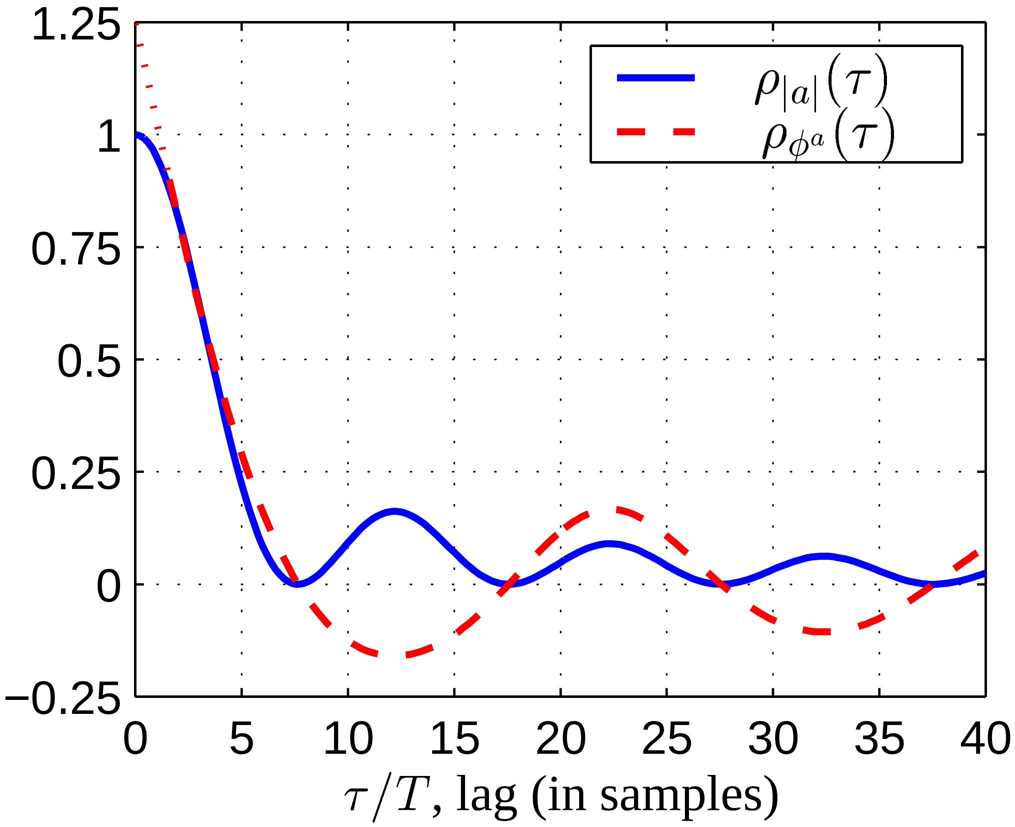

Figure 3.1: Correlation coefficient for the amplitude and the phase of the fading process $\{a_t\}$ for $f_D T = 0.05$. The approximation used in [16] to derive $\rho_{\phi^a}(\tau)$ for the phase is problematic at small lags, hence the dotted part of the curve.

result also carries over to the channel phase process, which is of interest here. Specifically, for the amplitude fading $r_t = |a_t|$ of a phase-coherent channel it is shown in [19] that the ratio $I(r_t; r_{t-2}|\ r_{t-1})/I(r_t, r_{t-1}; r_{t-2})$, which is a measure of deviation from Markovity for the channel amplitude $\{r_t\}$, is very small, and becomes smaller with decreasing Doppler rate. A similar result can be shown for the fading phase process $\{\phi_t^a\}$. Besides, it is intuitively obvious that a Markov model with a sufficiently high number of states can mimic the statistics of any process arbitrarily well, although the number of states necessary in our case to make the model very accurate would be beyond practical interest. In this dissertation, we limit the number of states K to a small integer multiple of the cardinality of the PSK constellation for simplicity.

The receiver can form a K-state Markov model for the quantized version Q_t of the phase fading process ϕ_t^a, where $\{Q_t\}, t = 0, 1, 2, \ldots$ is a time-homogeneous, discrete-time, stationary Markov chain, taking values in the finite state space $\mathcal{Q} = \{q_0, q_1, \ldots, q_{K-1}\}$, a set of "quantized channel phase distortion states" q_i:

$$q_i = \frac{2\pi i}{K},\ i = 0, 1, 2, \ldots, K-1, \tag{3.4}$$

in the following fashion, introducing a quantization operator $\Pi(.)$:

$$Q_t = q_i \Leftrightarrow \Pi(\phi_t^a) = q_i \Leftrightarrow \phi_t^a \in \left[q_i - \frac{\pi}{K}, q_i + \frac{\pi}{K}\right).$$

The transition probabilities $P_{q_i,q_j},\ i,j = 0, 1, \ldots, K-1$ of the Markov chain are independent of t by stationarity, and can be computed for known Doppler rate $f_D T$ from the joint pdf of two successive sampled fading phases:

$$\begin{aligned} P_{q_i,q_j} &= \Pr(Q_{t+1} = q_j \mid Q_t = q_i) && (3.5) \\ &= \frac{\int_{q_i-\pi/K}^{q_i+\pi/K} \int_{q_j-\pi/K}^{q_j+\pi/K} p(\phi_t^a, \phi_{t+1}^a) d\phi_t^a d\phi_{t+1}^a}{\int_{q_i-\pi/K}^{q_i+\pi/K} p(\phi_t^a) d\phi_t^a} && (3.6) \end{aligned}$$

where the marginal pdf is uniform, and the joint pdf is [16]:

$$p(\phi_t^a, \phi_{t+1}^a) = \frac{1-\rho^2}{4\pi^2}\left[\frac{\sqrt{1-B^2} + B(\pi - B\cos^{-1}(B))}{(1-B^2)^{3/2}}\right]$$

where $B = \rho \cdot \cos(\phi_{t+1}^a - \phi_t^a)$, and $\rho = \mathcal{J}_o(2\pi f_D T)$.

The model described above is essentially an approximation in a dual sense: First, it maps all real fading angles $\phi^a \in [-\pi, \pi)$ to a finite number of "quantized fading phase states" q_i, $i = 0, 1, \ldots, K-1$. Moreover, the model approximates the dynamics of the continuous process $\{\phi_t^a\}_{t=0,1,\ldots,\infty}$ with a discrete Markov chain, taking values in the finite-state space $\mathcal{Q}$ and having stationary probabilities $p_i = 1/K$ and transition probabilities P_{q_i,q_j}. It should be noted, however, that the channel estimation algorithm (based on the Forward-Backward algorithm) in Rayleigh fading does not perceive the channel phase as quantized to the K values of (3.4); the algorithms of Chapters 4 and 5 remain aware of the continuous nature of ϕ_t^a, but are based on the assumption that ϕ_t^a is uniformly distributed in a sector of length $2\pi/K$, given that it belongs in that sector. Hence, the finite-state Markov model is merely a way to reduce the infinite cardinality of the set of possible phases ϕ_t^a to K "phase states", such that reliabilities can be assigned to them by the Forward-Backward algorithm.

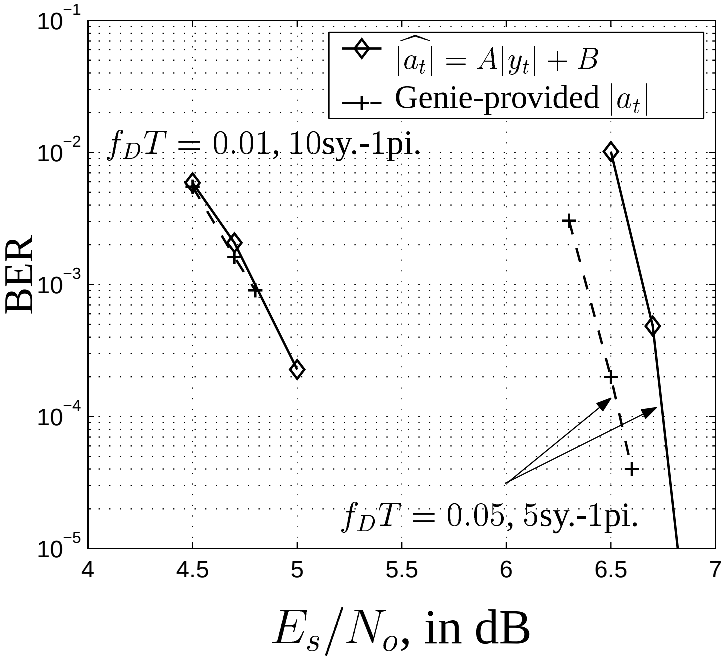

Figure 3.2: BER of turbo-code, in different f_DT, for different pilot insertion ratios. Performance with affine fading amplitude estimation from the received amplitude is very close to the case when the receiver has access to genie-provided channel amplitude $|a_t|$.

A Markov model closely related to the one described above was derived in [18] to model the amplitude fading of a phase-coherent Rayleigh fading channel. In that paper, several channel amplitude levels corresponded to binary symmetric channels (BSCs) with different crossover probabilities, thereby creating a Finite-State Markov Channel (FSMC). Here we recognize the phase distortion in a Rayleigh channel as a more severe problem for PSK transmission than amplitude fading.

This qualitative observation, along with the difficulty of obtaining coherent phase reference in a high Doppler, low SNR environment, indicates that the main channel estimation effort for PSK turbo-codes should be devoted to acquiring phase coherence rather than exact estimates for the fading amplitude $|a_t|$. Thus, the two receivers derived in the next chapter create the finite-state Markov (FSM) model outlined above and use it to estimate the channel phase with the Forward-Backward algorithm [12]. For the fading amplitude estimation they rely on a simple MMSE, symbol-by-symbol affine estimator from the received amplitude of the form $\widehat{|a_t|} = A|y_t| + B$. As shown in Fig. 3.2, this method for amplitude estimation, combined with Forward-Backward phase estimation on the FSM phase model, performs only slightly worse than when having perfect channel amplitude knowledge at the receiver. This result supports the decision to use a simple estimator for the fading amplitude and reserve the power of the Forward-Backward algorithm for phase estimation.

3.2 Quantized phase estimation

The performance of turbo-codes in flat fading was examined in [4]. In [20] and [21] it was recognized that additional performance benefits are possible when moving from “one-shot” channel estimation (e.g. from pilots) to iterative estimation, integrated with turbo decoding. Specifically, in [20] and [21] the channel estimators perform optimum (Wiener) filtering of symbols at each iteration (only pilots at first, and all symbols in subsequent iterations taking into account their reliability), thus exploiting extrinsic information produced by the turbo decoder about coded symbols.

In this section, we also apply the principle of iterative channel estimation, but not with filtering of pilots and coded symbols. Instead, we employ the Forward-Backward algorithm for “quantized phase” estimation based on the FSM model derived in section 3.1. In section 4.1.1 joint phase estimation and turbo decoding proceed along a supertrellis, constructed by merging the trellises of the code and the Markovian channel state structure. In section 4.1.2 we demonstrate better performance by using a separate Forward-Backward algorithm to estimate the phase state, operating on the trellis of the FSM phase model and exchanging soft information with the constituent decoder SISO [9].

Notice that in both approaches the Forward-Backward algorithm operates on the K-state Markov phase model, and obtains soft phase estimates in the form of a probability distribution on the K phase states at each time instant (implicitly in the supertrellis, explicitly with the separate trellises). Fig. 3.3 demonstrates the rationale behind this choice of “quantized phase” estimation: at the low SNR where turbo-codes operate, it is advantageous to have a phase estimate with small precision but high reliability (as is possible with the Forward-Backward algorithm on a finite-state phase model) rather than continuous valued estimates of limited reliability, like those provided by optimum filtering, which exhibits higher MSE.

Under the assumption of knowing the correct phase state (i.e. sector), which is a reasonable assumption with the Forward-Backward algorithm, Fig. 3.3 indicates that at low SNR and high Doppler (or, equivalently more sparse pilot spacing under the chosen Doppler of $f_D T = 0.05$) the “quantized phase” estimation approach outperforms Wiener filtering solutions in the estimation MSE sense, even with the coarse, symbol-by-symbol amplitude estimation $\widehat{|a_t|} = A|y_t| + B$. In fact, it is this amplitude error that accounts for most of the estimation MSE, as seen from the fact that beyond $K = 32$ no additional MSE gain is obtained by increasing the number of “quantized phase states.” Of course, at high SNR optimum linear pilot filtering works better than our non-linear “quantized phase” estimation, even if this is assumed to always identify the correct sector.

However, “quantized” estimation seems to have an advantage in the very noisy region of operation of turbo-codes, insofar as the channel estimation MSE is an indication of turbo-code bit error rate performance. For a fixed SNR, the sequence of thin curves shows decreasing MSE from linear filtering for increasing pilot density. This can be thought of as the improvement to channel estimation expected as the Wiener filter acquires more knowledge about the transmitted data through the turbo iterations. Even in this case, (e.g. when every third symbol becomes perfectly known, i.e. $D = 2$, the lowest thin curve in Fig. 3.3) if the non-linear phase estimation guesses the correct sector it promises slightly less MSE at low SNR.

For the derivation of the MSE in the cases of $D > 0$, please refer to Appendix A. The dotted curve, corresponding to the MSE of estimation when *all* coded symbols are known (essentially for $D = 0$, or estimation of a_k from all observables $y_t = a_t + n_t, t = -\infty, \dots, \infty$) is only included in the plot to mark the best estimation MSE that could be hoped for, if all data symbols were known. Of course, in that case there would be no need for decoding, and thus no need for channel estimation either. It comes as no surprise that this scenario (all symbols known) induces the lowest estimation MSE. The analytical expression for it is derived from a well-known result for optimal discrete-time smoothing (see, for instance, [22]).

Given *all* observations $y_t, t = -\infty, \dots, \infty$ of a process $\{y_t\}$, the optimum (i.e. linear least-mean-square) l.l.m.s. estimator of the process $\{a_t\}$ is the so-called non-causal Wiener filter:

$$K(e^{j\omega}) = \frac{S_{ay}(e^{j\omega})}{S_y(e^{j\omega})}, \tag{3.7}$$

and the corresponding minimum mean-squared error (m.m.s.e) is:

$$E|\tilde{a}_t|^2 = \frac{1}{2\pi}\int_{-\pi}^{\pi}\left(S_a\left(e^{j\omega}\right) - \frac{|S_{ay}(e^{j\omega})\,|^2}{S_y\left(e^{j\omega}\right)}d\omega\right) \tag{3.8}$$

In our case, the noise is additive ($y_t = a_t + n_t$) with power spectral density $S_n(f) = N_o = \sigma_n^2$, so the power spectra involved in the m.m.s.e. are:

$$\begin{aligned} S_{ay}(f) &= S_a(f) = \frac{1}{\pi\sqrt{f_d^2 - f^2}}, \quad |f| \leq f_d, & (3.9)\\ S_y(f) &= S_a(f) + S_n(f) = S_a(f) + N_o, & (3.10)\end{aligned}$$

where $f_d = f_D T$ is the discrete Doppler frequency.

So, the m.m.s.e. becomes (with $f = \omega/2\pi$):

$$\begin{aligned} \text{m.m.s.e.} &= \int_{-1/2}^{1/2} \frac{N_o \cdot S_a(f)}{N_o + S_a(f)}\,df & (3.11)\\ &= N_o \cdot \int_{-f_d}^{f_d} \frac{1}{1 + N_o\pi\sqrt{f_d^2 - f^2}}\,df & (3.12)\\ &= \frac{2}{\pi}\cdot\left(\frac{\pi}{2} + \frac{2\beta}{\sqrt{1-\beta^2}}\cdot \text{arctanh}\left(\frac{\beta - 1}{\sqrt{1-\beta^2}}\right)\right), & (3.13)\end{aligned}$$

where $\beta = \frac{1}{\pi\sigma_n^2 f_d} = \frac{1}{\pi N_o f_D T}$. Observe the synergistic effect of increasing Doppler rate and noise power in the expression for the m.m.s.e., which indicates that the estimation task becomes increasingly difficult for a more-noisy, faster-varying channel. Conversely, for $f_D T \to 0$ (no variation) and/or $\sigma_n \to 0$ (no noise) the estimation MSE with an optimum smoothing filter of infinite length goes to zero, as expected intuitively.

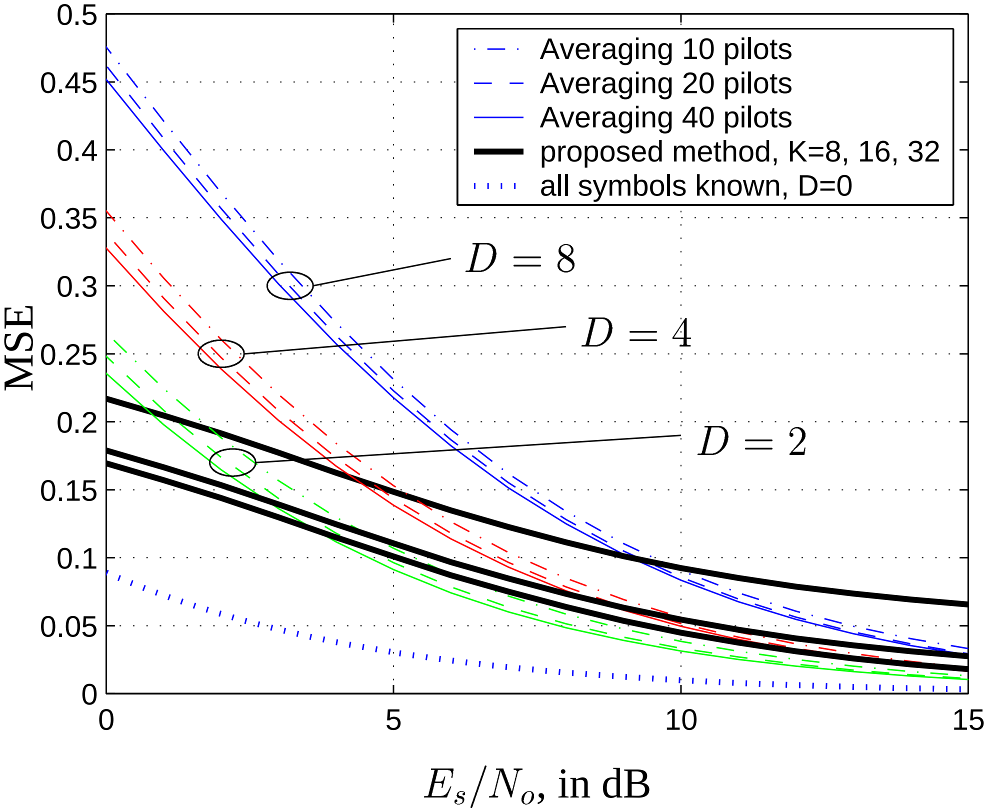

Figure 3.3: Mean-Squared Error (MSE) of channel estimation for a Rayleigh fading channel with $f_D T = 0.05$ under two scenarios: thin lines represent MSE after Wiener filtering of 10, 20, or 40 pilot symbols spaced one every D data symbols, while thick lines show the MSE resulting from simple affine amplitude estimation using only the received amplitude, and uniform phase uncertainty within a sector of $2\pi/K$ radians, $K = 8, 16, 32$, given that the correct sector is known. Note that this largely corresponds to the estimation procedure followed in the sequel. Observe that for low SNR the second approach is better. Of course, the dotted thin curve of the MSE when all symbols are known (could be thought of as "$D = 0$") is the best of all, but this serves only as an indication of the lowest MSE that can be hoped for.

CHAPTER 4

Algorithms for Joint Data and Channel Estimation

Optimal decoding in flat fading —either minimum bit error rate (MAP) decoding or maximum likelihood sequence detection (MLSD)— requires either explicit or implicit estimation of the channel. This chapter describes the FSM-model-based receiver algorithms in detail and presents simulation results.

4.1 Forward-Backward phase estimation

For "quantized phase" estimation with the Forward-Backward algorithm either on a supertrellis or on separate trellises the basic quantities needed are the probabilities $P_{q',q}$ of the channel phase transitioning from state (sector) q' to q (given in (3.5)-(3.6)) and the likelihoods $P(y_t \mid Q_t = q, x_t = x)$. At time t, the received complex symbol is $y_t = |y_t| \cdot e^{j\phi_t^y}$, where the total received angle ϕ_t^y is the sum of three distinct angles:

$$\phi_t^y = \phi_t^x + \phi_t^a + \phi_t^*, \tag{4.1}$$

as shown in Fig. 4.1. In this figure, ϕ_t^x is the transmitted constellation point angle, as the constituent trellis M-PSK code transitions from state c' to c, i.e., $x_t(c' \to c) = 1 \cdot e^{j\phi_t^x}$. The fading angle ϕ_t^a is defined from the fading scale factor $a_t = |a_t| \cdot e^{j\phi_t^a}$, and ϕ_t^* is the noise-induced additional angle, having distribution $P(\phi^*)$:

$$P(\phi^*; \lambda) = \frac{e^{-\lambda^2}}{2\pi} \cdot \left[1 + \sqrt{\pi}\lambda \cos\phi^* e^{(\lambda\cos\phi^*)^2} \text{erfc}(-\lambda\cos\phi^*)\right], \tag{4.2}$$

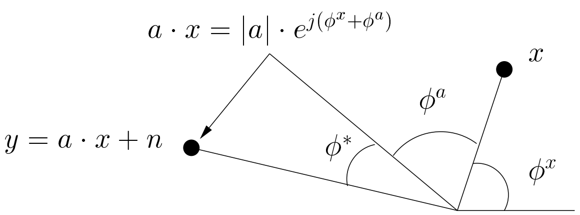

Figure 4.1: Addition of angles in fading

where erfc$(\cdot)$ is the complementary error function and the parameter λ of the distribution depends on the fading amplitude: $\lambda = \frac{|a|}{\sigma\sqrt{2}}$. Since the true fading amplitude is unknown, the receiver uses the symbol-by-symbol MMSE affine estimator $\widehat{|a_t|} = A|y_t| + B$ (with coefficients A and B depending only on the SNR of operation). Then it is straightforward to compute the desired likelihood of the received phase $\angle y_t = \phi_t^y$ given the channel phase state q and the transmitted point x:

$$\begin{aligned}
&\Pr\left(y_t \mid Q_t = q, x_t = x(c' \to c)\right) = && (4.3)\\
&\quad = \Pr\left(\phi_t^y = \theta \mid \Pi(\phi_t^a) = q, \lambda_t = \lambda, \phi_t^x = \angle x(c' \to c)\right) && (4.4)\\
&\quad \overset{\text{def}}{=} f(\theta \mid q, \lambda, x) && (4.5)\\
&\quad = \Pr\left(\phi_t^x + \phi_t^a + \phi_t^* = \theta | \ \Pi(\phi_t^a) = q, \lambda, \phi_t^x = \angle x\right) && (4.6)\\
&\quad = \Pr\left(\phi_t^a + \phi_t^* = \theta - \angle x \mid \phi_t^a \sim \mathcal{U}\left[q - \frac{\pi}{K}, q + \frac{\pi}{K}\right]\right) && (4.7)\\
&\quad = \frac{K}{2\pi} \cdot \int_{\theta-\angle x - q - \frac{\pi}{K}}^{\theta - \angle x - q + \frac{\pi}{K}} P(\phi^*; \lambda) d\phi^* && (4.8)
\end{aligned}$$

where $P(\phi^*; \lambda)$ was given in (4.2) and λ is approximated by:

$$\hat{\lambda}_t = \frac{A|y_t| + B}{\sigma\sqrt{2}} \qquad (4.9)$$

Thus, using the transition probabilities $P_{q',q}$ from (3.6) for the quantized channel phase, and $f(\theta \mid q, \lambda, x)$ from (4.8) we proceed to derive the joint algorithms on the supertrellis and on the separate trellises for the code and the channel.

4.1.1 Supertrellis algorithm

An initial approach to joint estimation and decoding is to combine the Markov model for the quantized fading phase discussed in Chapter 3 with the trellis describing the code, to form a *supertrellis*. In essence, the receiver observes the output of a finite-state machine (i.e., the encoder output x_t) multiplied with the output of a Markov process (i.e., the "fading phase state" Q_t) under AWGN. At time t, the state S_t of the supertrellis is an ordered pair consisting of the channel state Q_t and the code state C_t, giving $S_t = (Q_t, C_t) = (q, c) = m$, with $m = 0, 1, \ldots, 2^\nu K - 1$, for a code with ν memory elements.

Fig. 4.2 shows the block diagram of the turbo-coded system. Each constituent encoder at the transmitter produces $\log_2 M$ bits, mapped onto an M-PSK constellation. The symbols are transmitted into the fading channel in blocks of N, to preserve the fading phase correlation for the receiver supertrellises. Thus, the switches A and A' flip every NT seconds, where N is the turbo-code blocklength and T the baud period.

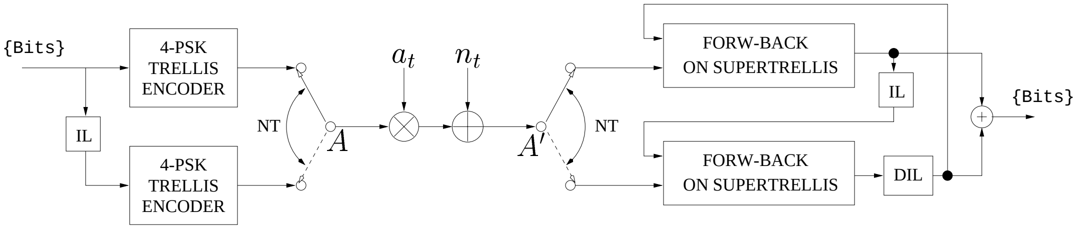

Figure 4.2: Block diagram of system employing iterative decoder.

The receiver consists of two identical modules that run the Forward-Backward algorithm and exchange soft information about the data through a uniform interleaver-deinterleaver pair. Each of them performs *joint* data and channel estimation internally, but provides the other estimator with extrinsic information only for the data, since the two blocks of constellation points (pertaining to unscrambled and scrambled data) are transmitted successively into the channel and undergo independent fading. Thus, information about the channel produced by one of the estimators would be irrelevant to the other. However, within each block of N symbols, the channel is correlated, which facilitates the joint estimation of channel phase and data.

The crucial quantity to compute in each supertrellis for iterative decoding [9], is:

$$\begin{aligned}\gamma_t(m', m) &\overset{\text{def}}{=} \Pr\left(y_t, S_t = (q, c) \mid S_{t-1} = (q', c')\right) = && (4.10)\\ &= \Pr\left(S_t = (q, c) \middle| S_{t-1} = (q', c')\right) \cdot \Pr\left(y_t \,|\, S_{t-1} = (q', c'), S_t = (q, c)\right) && (4.11)\end{aligned}$$

For the first term of (4.11) we have:

$$\begin{aligned}&\Pr\left(S_t = (q, c) \mid S_{t-1} = (q', c')\right) =\\ &= \Pr\Big(\Pi(\phi_t^a) = q \,|\, \Pi(\phi_{t-1}^a) = q'\Big) \cdot \Pr\left(u_t \text{ such that } C_t = c \,| C_{t-1} = c'\right) && (4.12)\\ &= P_{q',q} \cdot P(u_t; I), && (4.13)\end{aligned}$$

where $P(u_t; I)$ denotes the extrinsic information about the input u_t provided by the other soft decoder, and $P_{q',q}$ is the transition probability (3.5) of the quantized channel phases. The second term of (4.11) is clearly $f(\theta \mid q, \lambda, x)$ as defined in (4.5)-(4.8).

Note that the algorithm described above can be used with or without pilot symbols. The transition metric $\gamma_t(m', m)$ of (4.10) connects only superstates (m', m) with valid code state transitions $(c' \to c)$. In the case of pilots injected in the coded data stream, the code state does not change, and the only valid supertrellis branches are those with $c = c'$. Here we only present simulation results with no pilot symbols.

Fig. 4.3 presents the simulated BER performance of the system depicted in Fig. 4.2 under Rayleigh fading with $f_D T = 0.05$. The constituent codes are identical, 8-state, recursive systematic rate-1/2, Gray-labeled 4-PSK codes, with maximum effective Hamming distance. They are fully described by the octal parity polynomials $h_0 = 15$ and $h_1 = 17$. The number of quantized phases was $K = 8$, resulting in 64-state

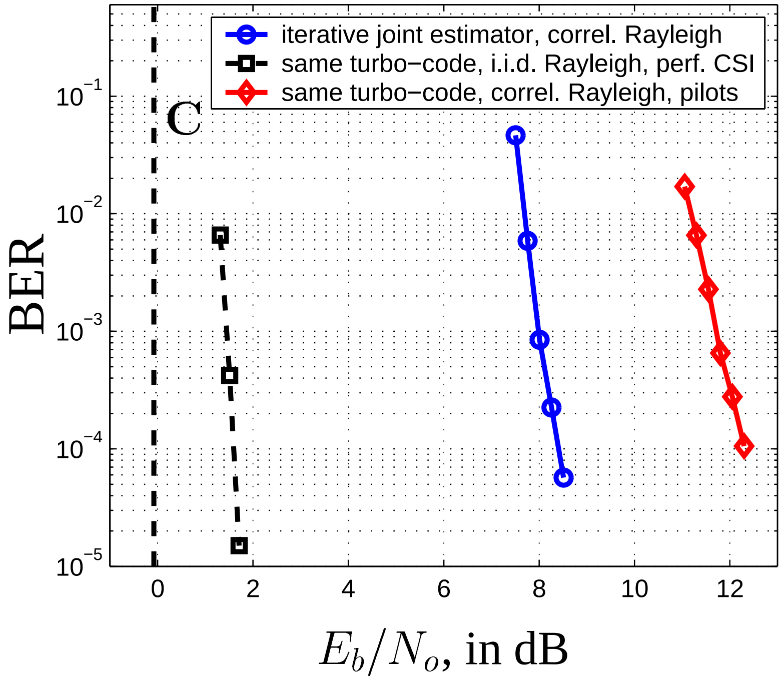

Figure 4.3: Supertrellis and non-iterative pilot filtering performance in Clarke's channel with $f_D T = 0.05$. The dashed curve shows performance of the same turbo-code in the same channel with ideal interleaving and perfect CSI at the receiver. The dashed vertical line marks the capacity in this ideal case.

supertrellises, and the blocklength was $N = 5000$ symbols. For this relatively high Doppler rate the performance is about 6.5 dB worse than when the same turbo-code operates under the ideal assumptions of perfect interleaving and perfect CSI (dashed curve). However, this gap is not very informative, since the constrained capacity of the two channels considered with uniform i.i.d. 4-PSK inputs is quite different at this high Doppler.

The vertical dashed line ("C" in Fig. 4.3) marks the capacity of the idealized scenario of perfectly known a_t at receiver. It is simply $I(X;Y|A)$, a weighted average of the AWGN capacity under the Rayleigh distribution $p_A(a) = 2a\,e^{-a^2}$, giving

$E_b/N_o = -0.08$ dB for the rate $1/2$ of interest. The capacity is smaller when CSI is unavailable at the receiver and has to be estimated from received values (much smaller for larger Doppler rates, and zero in the limit of i.i.d. fading). A more detailed discussion about constrained 4-PSK capacity under fading follows in section 4.2.2. To demonstrate the difficulty of obtaining accurate CSI in a practical system at high Doppler, we also simulated a pilot-symbol assisted system [23] with the same turbo-code. Specifically, a more sophisticated variant of pilot averaging in [24], using 3 pilot symbols every 5 data symbols performs almost 4 dB worse than our joint iterative estimator with no pilot symbols at all. Even if we plot against E_s/N_o disregarding the sacrifice of $3/8 = 37.5\%$ in rate of the pilot system [24], the supertrellis system is still almost 2 dB better. The reason is that essentially every coded symbol with the supertrellis iterations becomes somewhat a pilot, as its reliability increases.

The supertrellis receiver designed and simulated in this section has advantages and limitations. An obvious advantage is its ability to work without external acquisition circuitry or pilot symbols at relatively high Doppler rate. The low rate of each constituent code (here $1/2$) compensates for the absence of pilot symbols, allowing the supertrellis algorithm to determine whether a change in the received phase is due to the code or to a change in the channel. Thus, although this scheme does not lose rate directly because of pilots that bear no information, it is the rate reduction inherent in the constituent encoder design that makes channel estimation possible. On a higher level this can be viewed as incorporating the training in the code design, instead of explicitly injecting pilot symbols in the coded data stream of a higher rate code.

The main limitation is computational complexity, since the number of states in each supertrellis is the product of the code states and the number of phase intervals K. If M-PSK is used, then $K \geq 2 \cdot M$ for reasonable phase estimation. This leads to at least 64-state supertrellises with 4-PSK and 128-states with 8-PSK for 8-state constituent codes. Another limitation concerns diversity. The channel estimation procedure along the supertrellis precludes channel interleaving, because the algorithm relies on the correlation between successive phases. Hence, only implicit diversity, due to the interleaver between constituent codes, is provided.

4.1.2 Algorithm on separate trellises

In this section we derive and simulate a better structure for joint channel estimation and turbo decoding based on the Forward-Backward algorithm running on separate trellises for the channel phase and the code. Unlike the supertrellis algorithm presented in section 4.1.1, the joint iterative receiver in this section relies on known pilot symbols [23] for initial and subsequent channel estimates. For a powerful high-rate channel code, we designed a trellis turbo-code with overall rate of 1 bit/sec/Hz, where the constituent encoders are the best 8-state, rate-2/2 code fragments (see [5]-[10]), each producing one systematic and one parity bit per 2-bit input, and their outputs are mapped onto a Gray-labeled 4-PSK constellation, as shown in Fig. 4.4. This turbo-code will be the running example in this section and in the next chapter.

Observe that the trellis turbo encoder depicted in Fig. 4.4 is similar to the generic form discussed in Chapter 2 and [10]. Despite the difference in generating the parity bits, the encoder in Fig. 4.4 can be shown to be exactly equivalent to the generic form in Fig. 2.1 of Chapter 2. The specific constituent encoders, described by the set of octal polynomials $\{h_0 = 13, h_1 = 7, h_2 = 1, h_3 = 17\}$, corresponding to the feedback, the entrance of the two input bits, and the generation of the output bit respectively were identified by exhaustive search conducted as in [10]. The interested reader can find more details about constituent encoder design for trellis turbo-codes in [6] and [7].

Fig. 4.5 shows the transmitter block diagram. Notice the difference between the turbo interleaver (TIL), which is a random interleaver obtained as in [6, Ch. 4], and the

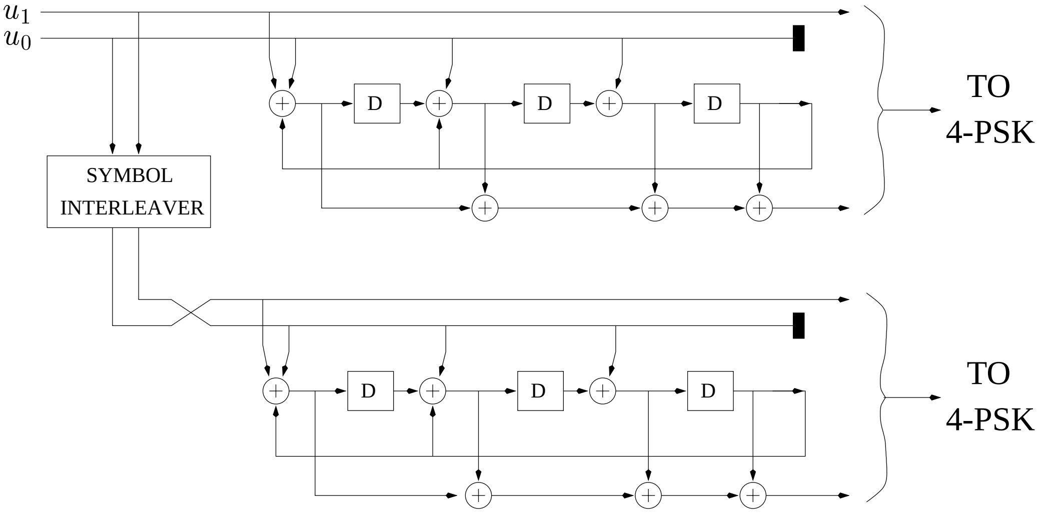

Figure 4.4: The turbo-code used in this section and Chapter 5, with overall rate of 1 bit/sec/Hz and rate-2/2, 8-state constituent encoders.

channel interleaver (CIL), which can be a regular block interleaver. Pilots are injected into the coded data stream at a rate of $Z \geq 1$ pilots every D coded PSK symbols, and the blocklength is $N = 4100$. Thus, for every $2N$ input bits, a total of $2N\frac{D+Z}{D}$ symbols are transmitted in flat Rayleigh fading.

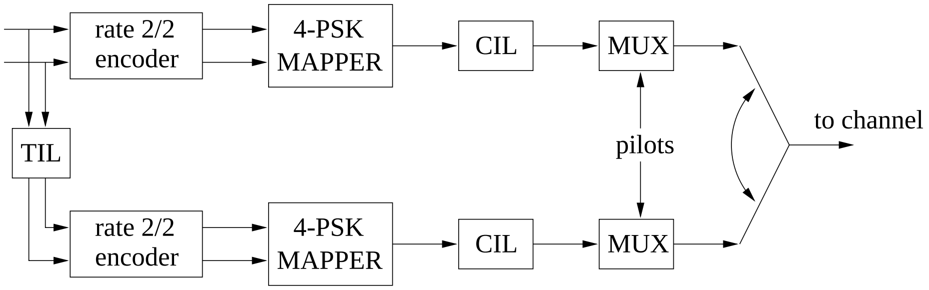

Figure 4.5: Transmitter block diagram for pilot-aided turbo-code.

Fig. 4.7 shows the receiver block diagram expanded in the direction of processing time, only to show the potential for a parallel or pipelined implementation. Each of the two main building blocks, denoted **Q** and **C**, implements the Forward-Backward algorithm (Q-SISO and C-SISO) on a separate trellis that describes the Markov channel phase and the code respectively, exploiting extrinsic information taken from the other block after the appropriate interleaving/deinterleaving operation – T(D)IL or C(D)IL. These two Soft-Input-Soft-Output (SISO) modules and their input/output functionality are depicted in Fig. 4.6. In the customary SISO notation of [9] $P(\cdot\ ;\ I)$ is extrinsic information about a certain quantity (the channel phase state q or the input symbol u or the output symbol x) *entering* the SISO block, while $P(\cdot\ ;\ O)$ is the updated extrinsic information about the pertinent quantity (again q, u or x) at the *output* of the corresponding Forward-Backward (SISO) block.

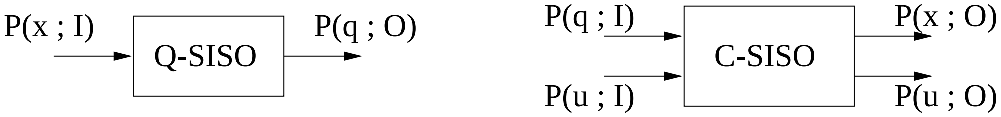

Figure 4.6: Basic SISO building blocks of the receiver.

The states are quantized channel phases q for Q-SISO and code states c for C-SISO, and the crucial quantity to compute is $\gamma_t(\text{state}_{t-1}, \text{state}_t)$. Specifically, for Q-SISO:

$$\begin{aligned}
\gamma_t(q', q) &= \Pr\left(y_t, Q_t = q \mid Q_{t-1} = q'\right) \\
&= \sum_x \Pr\left(y_t, Q_t = q, x_t = x \right| Q_{t-1} = q') \\
&= P_{q',q} \cdot \sum_x \Pr(x_t = x) \cdot \Pr\left(y_t \mid Q_t = q, x_t = x\right) \\
&= P_{q',q} \cdot \sum_x P(x\ ;\ I) \cdot f\left(\theta \mid q, \lambda, x\right), \qquad (4.14)
\end{aligned}$$

where the phase state transition probability $P_{q',q}$ is precomputed for known Doppler via (3.5)-(3.6), and θ is the received angle. The function $f\ (\theta \mid q, \lambda, x)$ is defined as in (4.5). Note that the Q-SISO operates on the whole received block of symbols, coded and pilots alike, but only outputs $P(q\ ;\ O)$ for the coded symbols, because information for the channel state during a pilot transmission is irrelevant to the C-SISO. Thus, at a time when a pilot is processed, the above summation is trivial (only one possible x has non-zero probability) and $P(q\ ;\ O)$ is not produced; just the $\alpha(q)$ and $\beta(q)$ quantities are updated in the channel trellis. For the C-SISO, we proceed with a similar computation, simpler in this case, since only coded data are processed and there is only one operating mode:

$$\begin{aligned}
\gamma_t(c', c) &= \Pr\left(y_t, C_t = c \mid C_{t-1} = c'\right) \\
&= \sum_q \Pr\left(y_t, C_t = c, Q_t = q \middle| C_{t-1} = c'\right) \\
&= \Pr\left(u \middle| c' \to c\right) \cdot \sum_q \Pr(Q_t = q) \cdot \Pr\left(\phi_t^y = \theta \middle| Q_t = q, x_t = \angle x(c' \to c)\right) \\
&= P\left(u\ ;\ I\right) \cdot \sum_q P(q\ ;\ I) \cdot f\left(\theta \mid q, \lambda, x(c' \to c)\right). \qquad (4.15)
\end{aligned}$$

Again, here $P\left(u\ ;\ I\right)$ is the extrinsic information about the information symbol u (composed of 2 bits) passed by the other C-SISO, while $P(q\ ;\ I)$ is the extrinsic information about the channel state, provided by the Q-SISO.

The performance of the proposed receiver has been checked in two flat fading channels, with Doppler rates 0.01 and 0.05, and the results are shown in Figures 4.8 and 4.9 respectively, for various pilot insertion rates. For comparison purposes, the plots include the performance of the same turbo-code when perfect CSI is available at the receiver. The vertical lines show the SNR where capacity equals the transmitted rate, assuming perfect CSI at the receiver (which is a lower bound to the SNR where capacity equals the transmitted rate when realistic channel estimation is performed through pilots). If not explicitly stated otherwise, the simulation was performed by considering $K = 8$ channel states at the receiver. From the two cases shown, setting $K = 16$ offers no improvement for $f_D T = 0.01$, but some improvement for $f_D T = 0.05$. The solid performance curves with different pilot spacing D provide some insight into the question of what pilot density is required for a given channel dynamic, as this

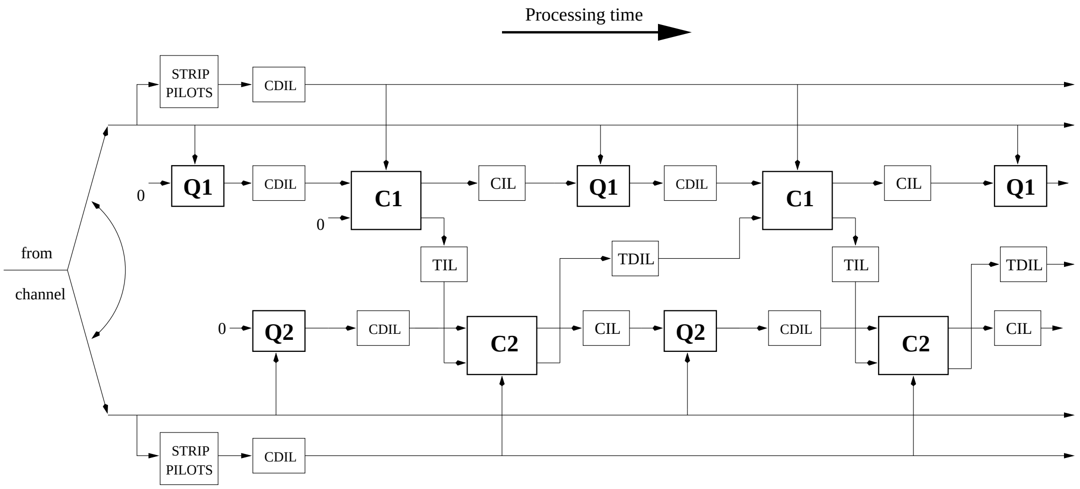

Figure 4.7: Receiver expansion in the processing time axis. Notice the possibility of parallel or pipelined operation.

is expressed by the Doppler rate $f_D T$.

Note that in the slower changing channel ($f_D T = 0.01$) the performance is about 1.5 dB away from the case when perfect CSI is available. The performance difference from perfect CSI is much more pronounced (about 4.5 dB) in Fig. 4.9, because the channel is less strongly correlated when $f_D T = 0.05$, which makes the estimation task more difficult, so the corresponding SNR (or capacity) penalty resulting from the lack of perfect channel estimates is larger. In general it is difficult to determine quantitatively exactly how the channel capacity is affected by the channel dynamics in order to quantify the intuitive statement made above. Detailed discussion on the effect of the rate of change of the channel on the capacity for a simplified, purely Markovian channel model related to Clarke's flat Rayleigh fading is the topic of the next section. Nevertheless, observe that a small number of pilots permits an increase in the overall rate of the system with separate trellises to 1 bit/sec/Hz, (excluding the pilots) relative to the rate of $1/2$ bit/sec/Hz for the supertrellis receiver. Furthermore, the complexity

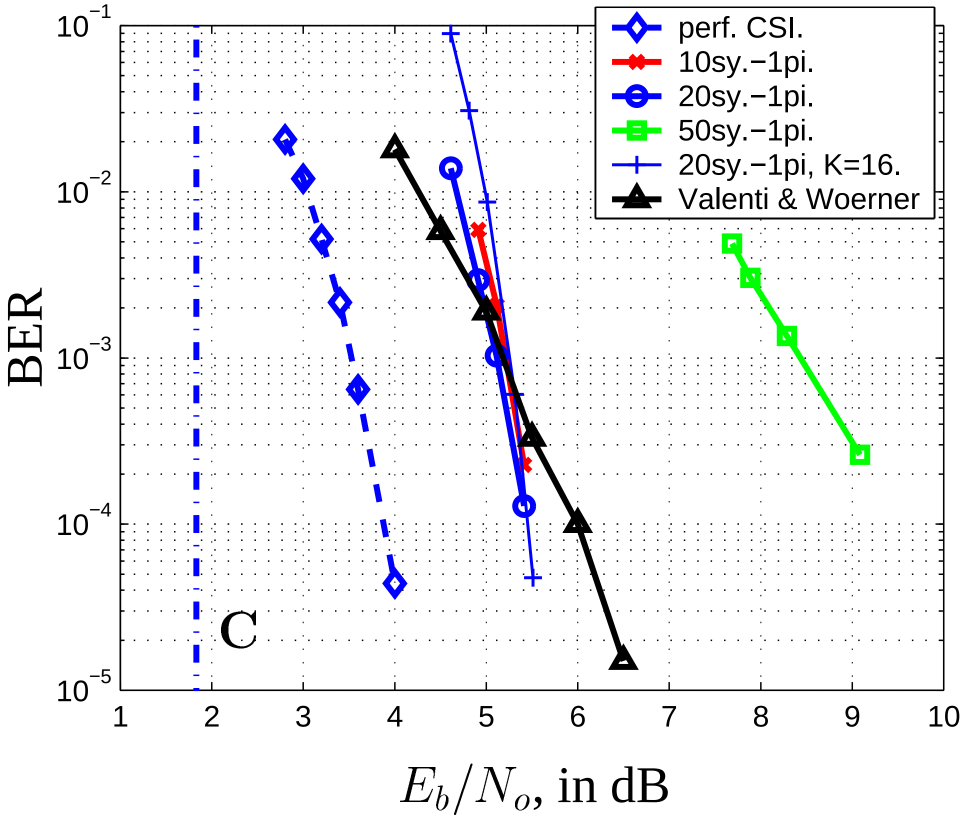

Figure 4.8: BER of turbo-code, for $f_D T = 0.01$ and for different pilot insertion ratios. Performance lags behind the perfect CSI case by about 1.5 dB. For perspective, the curve marked with triangles is the performance reported in [21], with a similar turbo-coded system with half the spectral efficiency as the one presented here.

of the separate trellises approach is much smaller (the Q-SISO has $K = 8$ or 16 states and the C-SISO 8 states), and the BER performance improves. However, these positive impacts on the rate, complexity and performance come at the expense of larger latency, due to channel interleaving.

Specifically, the two methods for joint channel estimation and turbo-decoding discussed in this section demand the following in terms of complexity and latency, for every decoder iteration (in parentheses the numbers in our 4-PSK simulations):

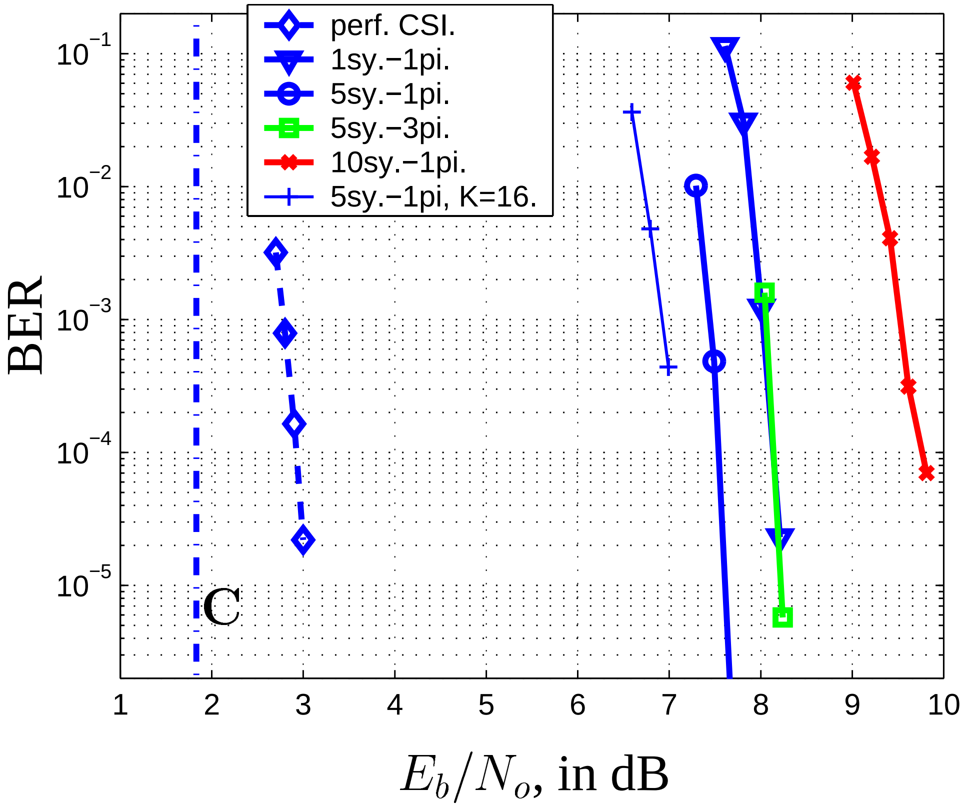

Figure 4.9: BER of turbo-code, for $f_D T = 0.05$ and for different pilot insertion ratios.

- supertrellis: two Forward-Backward algorithms, each on a supertrellis with $2^\nu \cdot K$ states (64 states), and $2K$ branches (16 here) emanating from each state. This number can be reduced, by pruning less likely transitions to phase-states far apart from the current one, particularly for small Doppler rates. This receiver suffers no extra latency from channel interleaving.

- separate trellises: less complexity, four Forward-Backward algorithms in all. Two for the two fully connected K-state Q-SISOs $(K = 8)$, and two for the 2^ν-state C-SISOs $(\nu = 3)$. Higher latency, because of channel interleaving at the transmitter and deinterleaving at the receiver. Here we implemented those block interleavers to be of equal size to the turbo-code blocklength N, but this is not necessary, particularly for high Doppler rates. The turbo-code latency is obviously unavoidable.

Finally, for comparison, the complexity of a pilot-averaging system obtaining one-shot channel estimates without iteration is just two 2^{ν}-state C-SISOs per iteration, plus the additional one-time cost of pilot filtering per block. The latency from channel interleaving is the same as in the separate trellises scenario. Thus, one-shot Wiener filtering of pilots has much less complexity but misses the benefit of interaction of the estimation and the decoding procedures, which assist each other in our joint estimation schemes.

4.2 Channel capacity

4.2.1 Simplified finite-state Markov channel (FSMC) model

For Clarke's flat Rayleigh channel of (3.1), where the process $\{a_t\}$ is stationary and ergodic, the definition of the capacity in Gallager [25] applies:

$$C = \lim_{N\to\infty} \frac{1}{N} \cdot I\left(X^N; Y^N\right) \tag{4.16}$$

where X^N and Y^N denote sequences of channel inputs and outputs respectively. Here we are interested in the constrained capacity for inputs from a finite uniform constellation, such as the 4-PSK we use. If the decoding delay is constrained to be small enough relative to the decorrelation time of the channel, then no positive rate is achievable, and outage probability, not capacity, becomes the correct performance measure [26]. In this discussion decoding delay will not be constrained, hence the capacity definition (4.16) is valid.

However, direct computation of the capacity of Clarke's channel (3.1), with the process $\{a_t\}$ having autocorrelation and power spectral density given by (3.2) and (3.3) is an open problem, although work has been done considering a piecewise constant channel or exponential autocorrelation, see [27]. Another body of work has determined the capacity of any finite-state Markovian channels (FSMC) in [28] and more generally in [29]. This is useful, because in practice a FSMC becomes a good model that mimics any channel statistics, if the number of states is chosen large enough.

Here, we study the following FSMC —admittedly more benign than Clarke's, but largely equivalent, and capturing most of the performance-driving phenomena of (3.1):

$$y_t = e^{jQ_t} \cdot x_t + n_t,\ t = 0, 1, 2.\dots \tag{4.17}$$

where $\{Q_t\}_{t=0,1,\dots}$ is the discrete K-state Markov chain of section 3.1, taking the values (3.4). In other words, the FSMC of (4.17) induces no amplitude fading, but rotates the transmitted phase by a discrete amount, correlated in time according to the Markov model of section 3.1, and adds AWGN.

The channel models of (3.1) and (4.17) have differences and similarities. For instance, the process $\{Q_t\}$ is not strictly bandlimited, unlike Clarke's $\{a_t\}$ process. Moreover, the FSMC only adds discrete phase distortion and no amplitude fading, hence it is more benign. Despite those differences, results obtained for the FSMC largely carry over to the more realistic channel model of Clarke, uniformly shifted by about $1 - 1.5$ dB. The relative ordering of simulations remains unchanged. This, along with the mathematical tractability of the FSMC in terms of capacity bounds, is the reason we focus attention on the FSMC model of (4.17) in this section.

Note that to simulate in this FSMC, the only modification in the algorithms derived so far is the definition of $f(\theta \mid q, \lambda, x)$ of (4.5). Since the channel phase is now discrete, there is no need for integration as in (4.8) and λ is fixed. So for the FSMC:

$$f\left(\theta \mid q, \lambda, x\right) = P\left(\phi^* = \theta - q - \angle x; \lambda = \frac{1}{\sigma\sqrt{2}}\right) \tag{4.18}$$

with $P(\phi^*; \lambda)$ as given in (4.2). Simulating in the pure FSMC of (4.17) eliminates the (small) discrepancy of the Rayleigh simulation, in which the channel in fact follows Clarke's model, but the receiver models it as having Markovian transitions between phase sectors. Results from simulations in the FSMC are shown in section 4.2.3, after deriving the capacity bounds in section 4.2.2.

4.2.2 Bounds on the capacity of a FSMC

For the capacity of any stationary, ergodic FSMC the definition (4.16) still applies. The algorithm in [29] (generalizing the results of [28]) offers a way to compute the capacity of a FSMC like the one considered here. However, the computation needed to obtain the limiting distributions of vectors π_n and ρ_n, where $\pi_n(k) = p(Q_n = q_k \mid x^{n-1}, y^{n-1})$ and $\rho_n = p(Q_n = q_k \mid y^{n-1})$, $k = 0, 1, \ldots, K-1$ (see [29]) is infeasible for a number of states K in the Markov model beyond $K = 2$ or 4. However, this is insufficient for our purposes here, since $K \geq 8$ for 4-PSK is needed to maintain reasonable similarity between the real world fading of Clarke and the FSMC of (4.17).

A computationally much simpler solution is to upper-bound the constrained capacity of the FSMC described in the previous section. An obvious, easy to compute, but very loose upper bound of C_{FSMC} of this Markovian quantized phase-distortion channel is the constrained capacity given the current state Q of the channel:

$$C_{FSMC} = \lim_{N\to\infty} \frac{1}{N} \cdot I\left(X^N; Y^N\right) \leq \lim_{n\to\infty} I(X_n; Y_n \mid Q_n) \tag{4.19}$$

Clearly this is the constrained capacity of the AWGN channel with PSK inputs, depicted in Fig. 4.10 as $I_{UB}(D=0)$ versus symbol SNR, E_s/N_o. But it is possible to compute a sequence of progressively tighter upper bounds on C_{FSMC}, from the following theorem:

Theorem 1 *For any finite-state Markov channel (FSMC) with states Q, a sequence of* *progressively tighter and asymptotically tight upper bounds to the capacity C_{FSMC} is:*

$$I_{UB}(D) = \frac{1}{D} \cdot I\left(X_1^D; Y_1^D \mid Q_0, Q_{D+1}\right), D = 0, 1, 2, \ldots, \infty \qquad (4.20)$$

where, for $D = 0$ we define the upper bound to be given by (4.19), or $I_{UB}(0) = I(X; Y \mid Q)$. □

The proof of this theorem is relegated to the Appendix. From the proof it also becomes obvious how to obtain asymptotically tight lower bounds on C_{FSMC}, namely the quantities $I_{LB}(D) = I_{UB}(D) - \frac{2 \log K}{D}$, where K is the number of states of the Markov channel. Unfortunately, those bounds are not tight enough to be useful for the first few terms (i.e., for $D = 0, 1, 2$) that we evaluate numerically below.

In Fig. 4.10 we plot the loose upper bound $I_{UB}(0)$ of (4.19), as well as the tighter bounds $I_{UB}(1)$ and $I_{UB}(2)$ against the channel SNR, for three FSMC's, with constant unit amplitude and $K = 8$ phase states, derived from Rayleigh channels with Doppler rates of 0.01, 0.05 and 0.1. Observe the capacity reduction with increasing Doppler rates, which demonstrates the increasing difficulty of reliable channel estimation in faster varying channels, even in cases where the noise is negligible. In the limit of the uncorrelated channel, (i.i.d. discrete distortion phases) channel estimation is impossible, and the constrained PSK capacity is identically zero regardless of the SNR. Conversely, when the Doppler rate is 0.01, the bounds show small capacity losses with respect to perfect channel information ($I_{UB}(0)$), indicating that in this case very good channel estimates can be obtained due to the strong time correlation.

From a different viewpoint the bounds $I_{UB}(D)$, $D > 0$ are not just capacity bounds in a case with no pilot symbols available at the receiver. $I_{UB}(D)$ also upperbounds capacity for a pilot-aided system, whereby groups of $Z \geq 1$ pilot symbols are injected into the coded data stream, spaced D or more coded symbols apart. This is true because $I_{UB}(D)$ decreases in D, and no group of pilots can ever offer better estimates of the

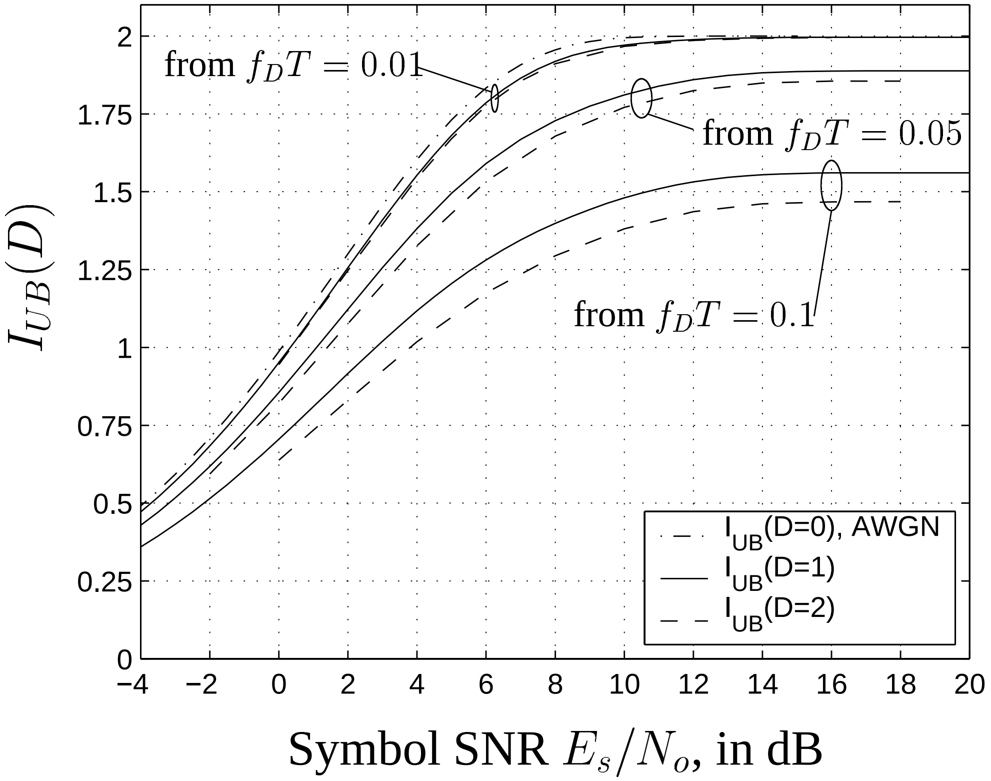

Figure 4.10: Bounds on C_{FSMC} for i.i.d. 4-PSK inputs, for Markov-phase channels derived from three different Rayleigh channels with Doppler rates $f_D T$, as described in Chapter 3.

channel for $t = 1, \ldots, D$ than noiseless knowledge of the channel states Q_0, Q_{D+1} at the outer edges of each group of D information symbols.

4.2.3 Performance in the FSMC relative to capacity

This section presents the BER performance of the algorithms discussed in section 4.1, simulated in the FSMC of (4.17). The only adaptation needed in the joint phase estimation and turbo decoding algorithms for the supertrellis as well as the separate trellises is shown in (4.18).

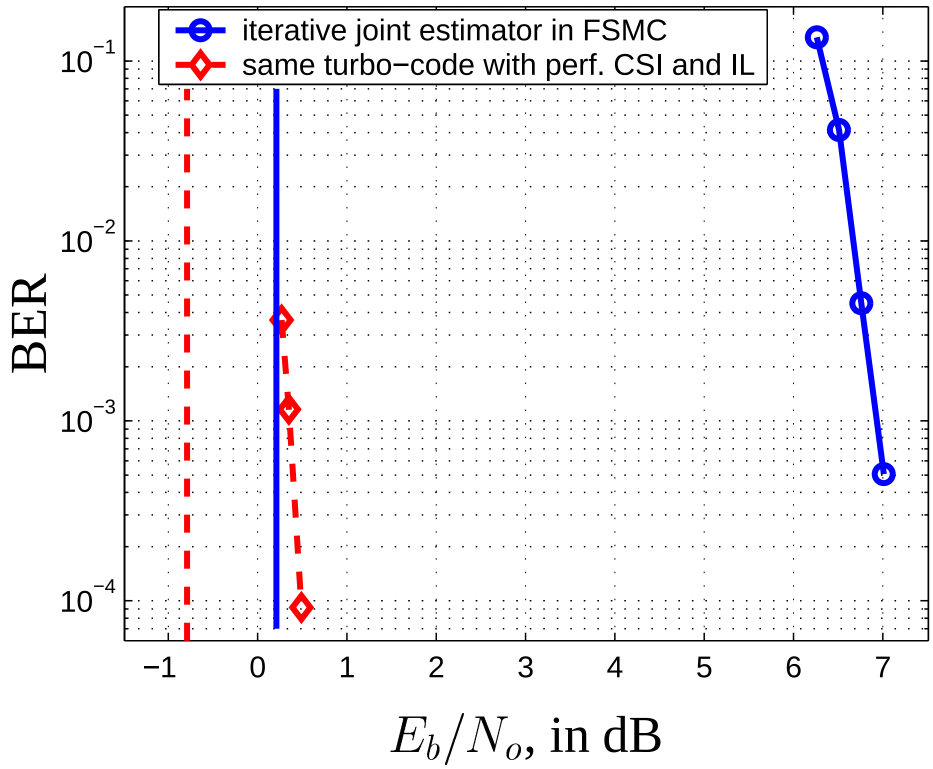

Figure 4.11: BER vs. E_b/N_o, for the turbo-code in the FSMC with $K = 8$ quantized phases derived from $f_DT = 0.05$. The solid vertical line shows the capacity bound $I_{UB}(2)$, while the dashed curve and line show performance and capacity respectively given perfect interleaving (IL) and CSI.

Fig. 4.11 shows the supertrellis simulation result. Note that both the solid curve (supertrellis in FSMC) and the dashed curve (same turbo code and channel with perfect interleaving and CSI at the receiver) are about 1 dB better than their Rayleigh counterparts in Fig. 4.3. Also, the solid vertical line marks the $E_b/N_o = 0.2$ dB of the capacity bound $I_{UB}(2)$, at rate $1/2$ bit/sec/Hz. This shows that the supertrellis receiver, due to the absence of pilots and channel interleaving performs quite far from the tightest capacity bound. In contrast, the same turbo-code with perfect interleaving and CSI performs very close to capacity, which is given by $I_{UB}(0)$ and marked by the vertical dashed line in Fig. 4.11.

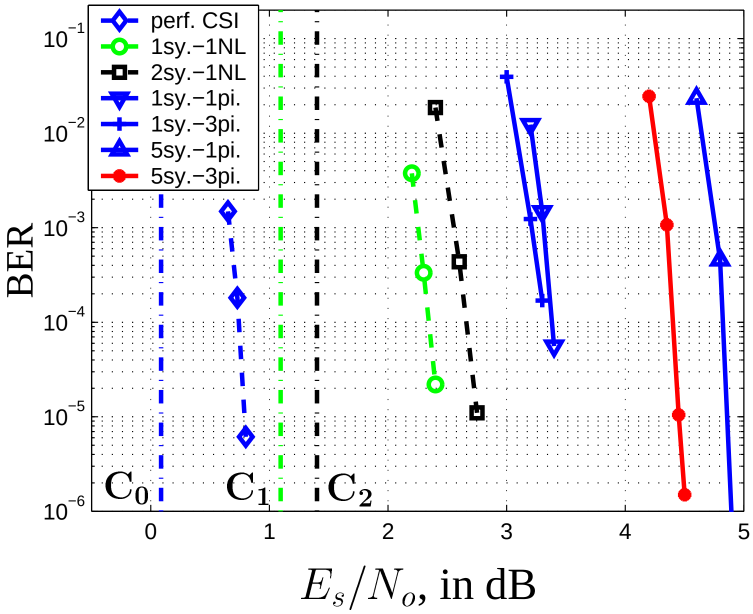

Figure 4.12: Capacity bounds and simulated BER in Markov channel for various pilot insertion rates. Vertical lines labeled C_0, C_1, C_2 mark the E_s/N_o where the capacity bounds $I_{UB}(D), D = 0, 1, 2$ respectively reach rate 1. Simulations with noiseless pilots (exact channel knowledge) every $D = 0, 1, 2$ coded symbols, for which C_0, C_1, C_2 are *exact* capacities, are plotted with dashed curves, marked with diamonds, circles and squares respectively. Solid curves are simulations with usual noisy pilots. SNR is plotted as E_s/N_o, to keep distance from capacity bounds consistent.

In Fig. 4.12 we show simulation results of the joint estimator on separate trellises in the Markov phase channel with $K = 8$ discrete phases, derived from $f_DT = 0.05$. The conventional simulations (solid curves) are with $D = 5$, and $D = 1$, namely injecting pilot symbols every 5, or every other coded data symbol. The dashed curves show simulation results when injecting one *noiseless* pilot, i.e., exact CSI, every $D = 1$ or 2 symbols. The dashed curve marked with “$\diamond$” shows performance with perfect CSI everywhere. All three of these simulation scenarios are idealized, since no noiseless pilots or perfect CSI can be available, but they are cases where the capacity bounds $I_{UB}(D), D = 0, 1, 2$ are no longer a bound, but the true capacity of these idealized transmission situations. Observe that the distance of the "noiseless" pilot simulated BER curves for $D = 1$ and 2 from the respective capacity bounds (dashed vertical lines marked C_1, C_2) is the same, a consistent 1.3 dB. Also note, that performance is plotted against symbol SNR E_s/N_o, unlike previous curves, in order to show the consistent SNR gap with respect to the capacity bounds.

The results of simulations in the Markov phase channel (those included in Fig. 4.12 and others) are summarized in Table 4.1 in the following fashion. The first column (D) shows how many consecutive information symbols are transmitted into the channel before $Z = 1$ or more (in the second column) consecutive pilot symbols are injected. In cases marked "noisy" in the third column, the pilot symbols are conventional pilots, offering noisy estimates of the channel at the edge-points of a D-symbol information block. Cases marked "noiseless" (NL) refer to the unrealistic scenario of a noiseless pilot, offering *exact* channel knowledge between groups of D symbols. For those cases the bounds $I_{UB}(D)$ are no longer bounds, but the exact capacity for this idealized transmission scheme. The fourth column of the table shows the E_s/N_o in dB, at which a BER of 10^{-4} is reached. The last two columns show the SNR gap between the simulated performance and performance with perfect CSI everywhere, and the SNR gap from the tightest appropriate capacity bound computed in section 4.2.2. Observe that the gap from the capacity bounds is *smaller* than that from perfect CSI, which shows that in this noisy, fast-varying channel the performance with perfect CSI is not achievable. For the first 3 rows, the correct capacity bound is $C_1 = 1.1$ dB, i.e., the E_s/N_o where $I_{UB}(D = 1)$ reaches rate 1. For all other rows, the tightest bound is $C_2 = 1.4$ dB, i.e., the SNR at which $I_{UB}(D = 2)$ reaches rate 1.

D	Z	pilot nature	SNR @ 10^{-4}	Gap from CSI	Gap from $C_{1,2}$
1	1	noisy	3.38 dB	2.58 dB	2.28 dB
1	3	noisy	3.26 dB	2.46 dB	2.16 dB
1	1	noiseless	2.4 dB	1.6 dB	1.3 dB
2	1	noiseless	2.7 dB	1.9 dB	1.3 dB
5	1	noisy	4.86 dB	4.06 dB	3.46 dB
5	3	noisy	4.4 dB	3.6 dB	3.0 dB
5	1	noiseless	3.4 dB	2.6 dB	2.0 dB
10	1	noisy	5.95 dB	5.15 dB	4.55 dB
10	3	noisy	5.51 dB	4.71 dB	4.11 dB
10	1	noiseless	4.81 dB	4.01 dB	3.41 dB

Table 4.1: Simulation results for the pilot-aided turbo-code in the FSMC derived from $f_D T = 0.05$.

The results in Table 4.1 are not surprising. They indicate steady improvement as the number of pilot symbols and the rate at which pilot groups are injected increase. Obviously the scenarios of the third and fourth row are closest to capacity, and the SNR gap increases as groups of pilots are further apart from each other (D increases). It must be noted that results in Fig. 4.12 and Table 4.1 are in terms of E_s/N_o and thus do not take into account the energy expended on pilots, because this makes their correspondence with the capacity bounds more clear. For instance, if shown against E_b/N_o, row 6 of Table 4.1 would be worse than row 5, because a lot of energy is wasted on evidently unnecessary pilot symbols.

On a related issue, for the case on the first row of Table 4.1 with $Z = 1$ and $D = 1$, BER of 10^{-4} is reached at $E_s/N_o = 3.38$ dB, or $E_b/N_o = 6.38$ dB, since the information rate is $1/2$ bit/symbol, as reduced by the pilots from the rate-1 turbo-code.

The same BER at the same information rate is achieved at $E_b/N_o \geq 7.0$ dB with the supertrellis receiver, see Fig. 4.11, because the turbo-code there is of rate-1/2. This performance improvement of at least 0.6 dB highlights the positive effect of channel interleaving in providing diversity for the separate trellises approach, despite the larger complexity of the supertrellis.

CHAPTER 5

Diversity Reception in Flat Fading

For a general multipath fading channel, reception errors usually occur when the time-varying signal attenuation introduced by the channel is large, or when the channel is in a deep fade. A good strategy to overcome this problem is to provide the receiver with several replicas of the information signal, transmitted over independently fading channels, and hence reduce the probability that all signal components will fade simultaneously [30]. The presence of conditionally independent replicas of the information-bearing signal at the receiver is called diversity. There are three common types of diversity: frequency, time and space. Frequency diversity is only possible if the transmission bandwidth exceeds the channel coherence bandwidth —i.e., it is not available in flat fading. An equalizer, a RAKE receiver [31, 32], or coded multicarrier transmission [33] can exploit frequency diversity. Time-diversity is often accomplished with coding and interleaving; trellis codes do the same in a bandwidth-efficient fashion. Spatial diversity is achieved by using multiple receiver antennas. This form of diversity avoids the bandwidth expansion implicit in frequency and (often) time diversity, but requires additional complexity in the RF and baseband portions of the receiver.

This chapter extends the algorithm for joint phase estimation and turbo-decoding on separate trellises, derived in Chapter 4, to the case where several ($L \geq 1$) branches of spatial diversity are available at the receiver, thus simultaneously exploiting antenna diversity and time-diversity with the turbo-code. In this scenario, the utilization of the L soft channel estimates provided by the quantized phase estimators to the turbo-decoder may be thought of as iterative ”soft diversity combining”. Achievable performance of turbo-codes using this estimation method is compared with the performance when the estimation method is iterative Wiener filtering of received symbols and then maximal ratio combining [30, Chp. 14] in the turbo-decoder. The discussion is again limited to flat Rayleigh fading channels, and simulation results help assess the BER performance with respect to the capacity gains promised by receiver diversity.

5.1 Transmission and channel model

To demonstrate joint iterative estimation and decoding of pilot-aided turbo-codes when receiver diversity is available, we use the same rate-1 bit/sec/Hz turbo-code as in section 4.1.2. Fig. 5.1 repeats the structure of the transmitter for convenience. The constituent encoders are the best 8-state, rate-2/2 code fragments, identified via exhaustive search as in [10], each producing one systematic and one parity bit per 2-bit input, and their outputs are mapped onto a Gray-labeled 4-PSK constellation, following the general turbo-trellis coding paradigm of Chapter 2. The encoders are the same as the ones in Fig. 4.4. Notice, that as in section 4.1.2, for each block of $2N$ input bits, the $N\frac{D+Z}{D}$ pilots and coded symbols form each constituent encoder are transmitted contiguously into the channel; the switch flips every $N\frac{D+Z}{D}T$ seconds, where T is the baud period.

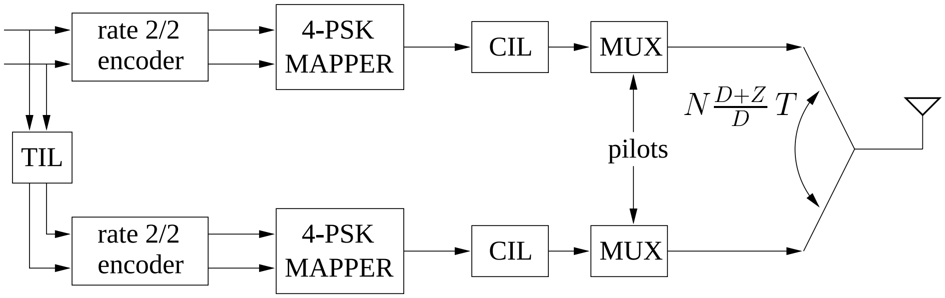

Figure 5.1: Block diagram of the transmitter in a pilot-aided trellis turbo-coded system.

The channel with one transmitter and $L \geq 1$ receiver antennas produces independent realizations of the fading coefficients and the noise at each of the receiver branches, as shown in Fig. 5.2.

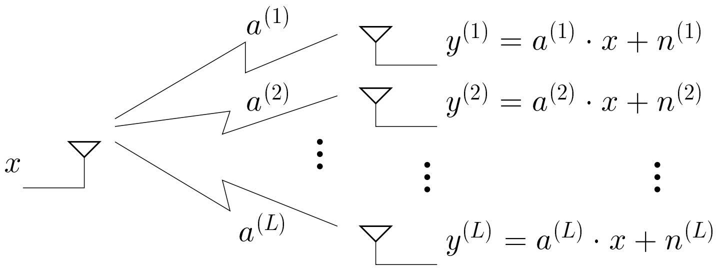
$a^{(1)}$
$y^{(1)} = a^{(1)} \cdot x + n^{(1)}$
$a^{(2)}$
$y^{(2)} = a^{(2)} \cdot x + n^{(2)}$
x
$a^{(L)}$
$y^{(L)} = a^{(L)} \cdot x + n^{(L)}$

Figure 5.2: Flat fading channel with L branches of receiver diversity.

Each of the diversity channels is modeled as an independent non-dispersive (flat) Rayleigh fading channel, correlated in time, based on Clarke's fading model [15], as explained in Chapter 3. According to this model, after matched filtering and proper sampling, the discrete representation of the received signal at time t and diversity branch i, $i = 1, \ldots, L$, is:

$$y_t^{(i)} = a_t^{(i)} \cdot x_t + n_t^{(i)}, \; i = 1, \ldots, L, \; t = 0, 1, 2, \ldots \tag{5.1}$$

where x_t is the transmitted constellation point. The channel coefficients and the noise are independent in the different channels, but the fading in each channel remains time-correlated:

$$Ea_{t_1}^{(i)}[a_{t_2}^{(j)}]^* = \mathcal{J}_o(2\pi f_D T |t_1 - t_2|) \cdot \delta(i-j) \tag{5.2}$$

$$En_{t_1}^{(i)}[n_{t_2}^{(j)}]^* = N_o \cdot \delta(t_1 - t_2) \cdot \delta(i-j) \tag{5.3}$$

and the noise process has variance $\sigma^2 = N_o/2$ per dimension. Each time-correlated channel fading process $\{a_t^{(i)}\}$, $i = 1, \ldots, L$ is modeled as a zero-mean circular complex Gaussian random process. The marginal distributions of $|a_t^{(i)}|$ and $\phi_t^{a^{(i)}} = \angle a_t^{(i)}$

for each i are Rayleigh and uniform respectively [17], hence the term “Rayleigh fading”. The correlation properties of each fading processes $a_t^{(i)}$, $i = 1, \ldots, L$ —see (5.2)— depend on the common Doppler rate $f_D T$ for all receiver branches, since they are probably mounted on the same physical device and move simultaneously.

5.2 General iterative receiver

Given the turbo-coded, pilot-aided transmission model of Fig. 5.1, the block diagram of a generic receiver with iterative channel estimation and diversity of order L is depicted in Fig. 5.3.

The blocks “D1” and “D2” are the constituent decoders (SISOs) for the turbo-code, and they implement the Forward-Backward algorithm. They exchange extrinsic information ($P(u; I), P(u; O)$) about the 2-bit input symbols u through the uniform random interleaver/deinterleaver pair TIL/TDIL. At the same time they produce extrinsic information $P(x; O)$ about the coded symbols x, in order to assist the channel estimation procedure on all diversity branches. Estimation is performed by the array of identical modules E1$_i$, E2$_i$, $i = 1, \ldots, L$. For the functionality of these estimation blocks, this chapter considers two options.

In the first approach, henceforth dubbed the “quantized approach”, (dashed feedback path in Fig. 5.3) no operation other than channel deinterleaving is performed on the probability vectors $P(x; O)$ before they are fed back into the estimator modules. They, in turn, produce probability vectors about the quantized channel phase, in exactly the same fashion as the Q-SISO blocks described in Chapter 4. In the second iterative estimation algorithm, the “filtering approach”, (solid feedback line in Fig. 5.3) the vector of soft information $P(x; O)$—each entry of this vector is the extrinsic probability of a possible constellation point x—passes through the nonlinearity “NonLin”,

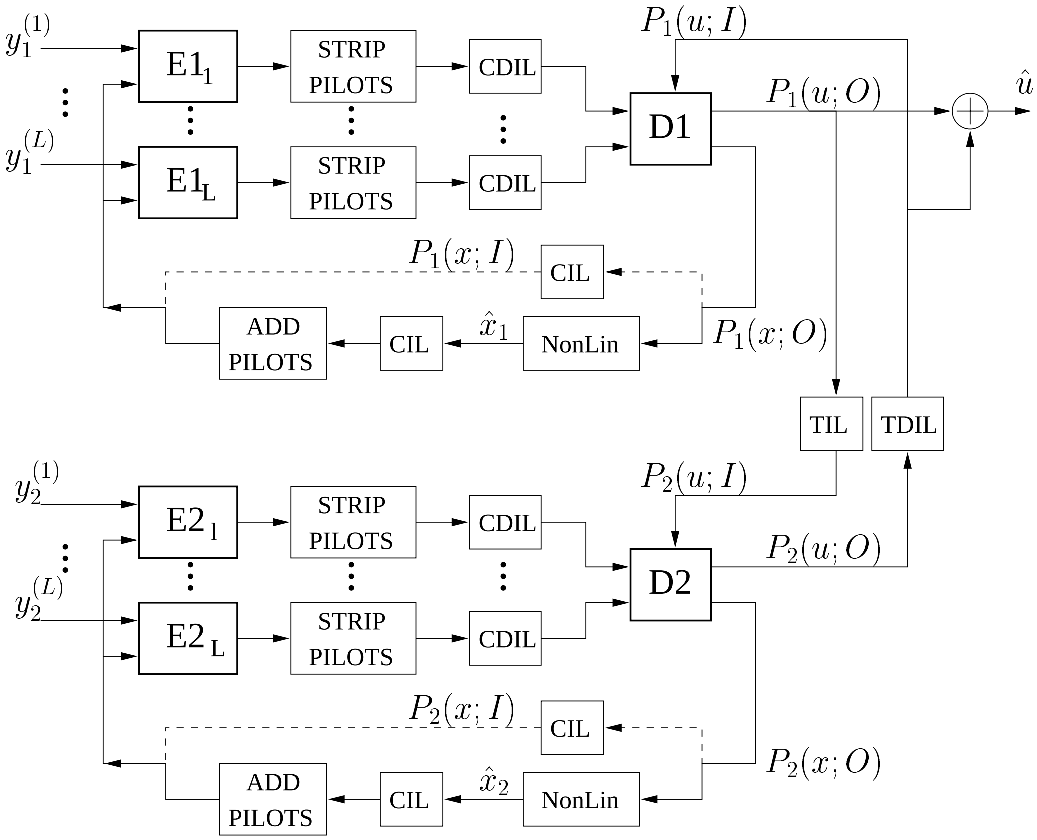

Figure 5.3: Receiver block diagram for turbo-decoder with diversity and iterative channel estimation.

which provides a coded symbol estimate $\hat{x}$. Then, those estimates $\hat{x}$ are deinterleaved and pilot symbols are injected into the stream, replicating the procedure followed at the transmitter. Then, this stream of estimated coded symbols x and pilots is used by the estimator modules, which perform optimal filtering in order to produce channel estimates $\hat{a}^{(i)}$, $i = 1, \ldots, L$ to be used by the turbo-decoders in the next iteration.

The next two sections explain both algorithms in detail, and discuss issues such as estimation in the first iteration, or the nature of the nonlinear operation “NonLin”. Description of both algorithms amounts to analyzing the functionality of the blocks denoted $\mathrm{E1}_i, \mathrm{E2}_i,\ i = 1, \ldots, L$ in Fig. 5.3 for both the “quantized approach” and the “filtering approach”, as well as the corresponding metric used by the constituent decoders “D1” and “D2” in conjunction with each channel estimation method.

5.2.1 Quantized phase approach

For PSK transmission the acquisition of phase coherence is a more critical problem than fading amplitude estimation, as discussed in Chapter 3. Thus, the quantized phase algorithm invests most of the computational effort into obtaining an accurate probability distribution $P_i(q; O)$ on the quantized phases $q = Q\left(\phi^{a^{(i)}}\right)$ of each diversity channel $i = 1, \dots, L$ via the Forward-Backward algorithm. Thus, each estimation module E1$_i$, E2$_i$ of Fig. 5.3 becomes a Q-SISO, described in Chapter 4. For an estimate of the fading amplitude $\left|a^{(i)}\right|$ each Q-SISO uses a simple, symbol-by-symbol optimum affine estimator from the received amplitude, namely:

$$\widehat{|a^{(i)}|} = A \cdot |y^{(i)}| + B, \quad i = 1, \dots, L \tag{5.4}$$

where A, B are real coefficients depending on the SNR (hence the same for all i), and they are computed to ensure unbiasedness and MMSE of the amplitude estimates.

For the phase estimation, each Q-SISO considers the quantized version of the channel phase $\phi^{a^{(i)}}$ into K phase intervals as in section 4.1.2. All the Q-SISOs (there are $2L$ of them in the receiver) create the same Markov model, which approximates the values and the statistical properties of each $\phi^{a^{(i)}}$. The transition probabilities between phase sectors depend on the common Doppler rate $f_D T$, and can be computed as in (3.5)-(3.6). Fig. 5.4 provides an example of the Markovian transition probabilities for the quantized phase, as derived for two Doppler rates.

Given the quantized version q of the channel phase $\left(q = \frac{2\pi j}{K},\ j = 0, 1, \dots, K-1\right)$, the i^{th} Q-SISO considers the real-valued phase $\phi^{a^{(i)}}$ to be uniformly distributed within the interval $\left[q - \frac{\pi}{K}, q + \frac{\pi}{K}\right]$. Then, recall from Fig. 4.1 that on each diversity branch

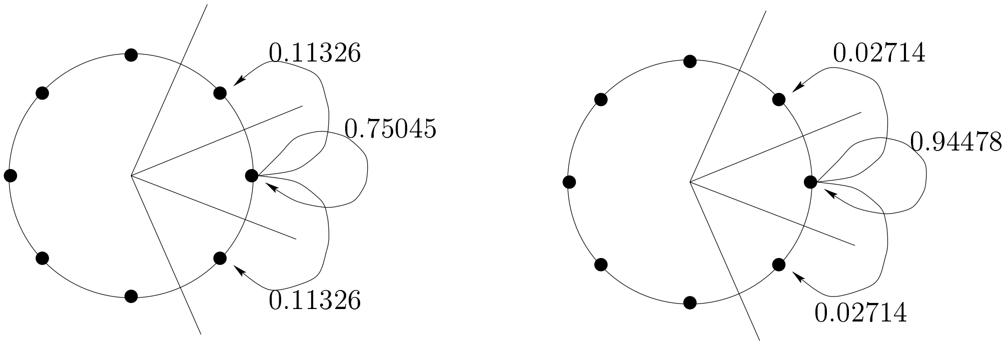

Figure 5.4: Transition probabilities for $f_D T = 0.05$ (left) and $f_D T = 0.01$ (right), for $K = 8$ quantized phases.

the received angle $\theta^{(i)} = \angle y_t^{(i)}$ at time t is the sum of the common transmitted angle $\angle x_t$, the fading angle $\phi_t^{a^{(i)}}$ and the noise induced angle $\phi_t^{*^{(i)}}$, distributed as in (4.2).

With that in mind, as in section 4.1.2, each Q-SISO runs the Forward-Backward algorithm on the trellis of the quantized Markovian channel phases, and produces probabilities $P_i(q; O)$ for those quantized phases q, on each diversity channel i, $i = 1, \dots, L$. To do that, following the derivation in (4.14) and using (4.5), it is straightforward for the i^{th} Q-SISO to compute the branch metric $\gamma_t^{(i)}(q', q)$ as follows:

$$\gamma_t^{(i)}(q', q) \overset{\text{def}}{=} \Pr\left(y_t^{(i)} = \left|y_t^{(i)}\right| e^{j\theta^{(i)}},\, q_t^{(i)} = q \mid q_{t-1}^{(i)} = q'\right) \tag{5.5}$$

$$= P(q' \to q) \cdot \sum_x P(x; I) \cdot \frac{K}{2\pi} \int_{\theta^{(i)} - \angle x - q - \frac{\pi}{K}}^{\theta^{(i)} - \angle x - q + \frac{\pi}{K}} P\left(\phi^*; \lambda_t^{(i)}\right) d\phi^* \tag{5.6}$$

where $P(\phi^*; \lambda)$ was given in (4.2) and $\lambda_t^{(i)}$ is approximated, using the estimate $\widehat{|a^{(i)}|}$ from (5.4), by:

$$\widehat{\lambda_t^{(i)}} = \frac{A\left|y_t^{(i)}\right| + B}{\sigma\sqrt{2}} \tag{5.7}$$

Thus, using the precomputed Markovian transition probabilities $P(q' \to q)$, as well as the extrinsics $P(x; I)$ fed back by the constituent turbo-decoder “D1” or “D2”, each Q-SISO is able to provide the desired extrinsic information $P_i(q; O)$ about the quantized channel phase in each diversity branch. Those L distinct vectors of extrinsic probabilities $P_i(q; O)$, $i = 1, \ldots, L$ are subsequently deinterleaved and passed to the turbo-decoder ("D1" or "D2"), as shown in Fig. 5.3.

At the first iteration, when no prior $P(x; I)$ is available, all inputs $P(x; I)$ to the Q-SISOs are set to zero (in the log domain), denoting equal probabilities, with the exception of points t in time which belong to a pilot slot. Since the pilot symbol is known *a priori*, each Q-SISO uses the most skewed pmf there, setting the probability of the pilot symbol to a very large number (certainty) and the others to zero. This special handling of the pilots also carries over to subsequent iterations of the estimation procedure. Thus, for pilots, the summation of (5.6) is trivial (only one possible x has non-zero probability). At times t corresponding to coded data and not pilots the summation of (5.6) is necessary to compute the correct branch metric $\gamma_t^{(i)}(q', q)$ and run the Forward-Backward algorithm in each Q-SISO.

At every time t, each constituent decoder ("D1" or "D2" in Fig. 5.3) receives from the L Q-SISOs after deinterleaving the L vectors $P_i(q; I)$, $i = 1, \ldots, L$, each of length K—the number of quantized phase states. These K-entry vectors $P_i(q; I)$, $i = 1, \ldots, L$, contain the soft information about the quantized channel phase $q^{(i)}$ on each of the diversity branches, so denote their entries:

$$P\left(q^{(i)}; I\right), \quad q^{(i)} = 0, \ldots, K-1, \quad i = 1, \ldots, L. \tag{5.8}$$

For ease of notation, boldface letters denote the L-length vectors of the received (deinterleaved) samples and the quantized phases: $\mathbf{y}_t = [y_t^{(1)} \ldots y_t^{(L)}]$ and $\mathbf{q}_t = [q_t^{(1)} \ldots q_t^{(L)}]$. Clearly, the "vector phase-state" $\mathbf{q}_t$ of the L-branch diversity channel can take one of any K^L possible values. Given the independence between diversity channels, the probability of the channel vector-state is:

$$P\left(\mathbf{q}_t = \mathbf{q}\right) = \prod_{i=1}^{L} P(q^{(i)}; I). \tag{5.9}$$

Thus, the constituent decoder can run the Forward-Backward algorithm on the code trellis, and compute the branch metric $\gamma_t(c', c)$, based on the vector observations $\mathbf{y}_t$. Since the channel estimates obtained from the Q-SISOs are not hard estimates $\hat{a}^{(i)}$ of the fading coefficients, but *soft* estimates, i.e. probabilities that the channel phase is in one of K sectors, the decoder performs soft-diversity combining. With this quantized approach, and denoting the code states as c' and c, each decoder ("D1" or "D2") computes the Forward-Backward branch metric $\gamma_t(c', c)$ as follows:

$$\begin{aligned}
\gamma_t(c', c) &= \Pr\left(\mathbf{y}_t, C_t = c \middle|\, C_{t-1} = c'\right) && (5.10)\\
&= P\left(u_t \text{ such that } c' \to c\right) \cdot P\left(\mathbf{y}_t \,|\, x(c' \to c)\right) && (5.11)\\
&= P(u; I) \cdot \sum_{\mathbf{q}} P\left(\mathbf{y}_t, \mathbf{q}_t = \mathbf{q} \,|\, x(c' \to c)\right) && (5.12)\\
&= P(u; I) \cdot \sum_{\mathbf{q}} P\left(\mathbf{q}_t = \mathbf{q}\right) \cdot P\left(\mathbf{y}_t \,|\, x(c' \to c), \mathbf{q}\right) && (5.13)\\
&= P(u; I) \cdot \sum_{q^{(1)},\ldots,q^{(L)}} \prod_{i=1}^{L} P(q^{(i)}; I) \cdot P\left(y_t^{(i)} \,|\, x(c' \to c), q^{(i)}\right) && (5.14)\\
&= P(u; I) \cdot \sum_{q^{(1)},\ldots,q^{(L)}} \prod_{i=1}^{L} P(q^{(i)}; I) \cdot \frac{K}{2\pi} \int_{\theta^{(i)} - \angle x - q - \frac{\pi}{K}}^{\theta^{(i)} - \angle x - q + \frac{\pi}{K}} P(\phi^*; \lambda_t^{(i)}) d\phi^*
\end{aligned}$$

Of the terms in the above formula, $P(u; I)$ is the extrinsic information about the input symbol u and is provided by the *other* constituent decoder, while $P(q^{(i)}; I)$ is provided by the i^{th} Q-SISO. The summation involves K^L distinct terms, each of which is the product of two terms, as shown in (5.14). Hence, the constituent decoder "D1" (or "D2") essentially performs soft combining of the quantized soft channel estimates coming from the estimators E1$_i$, $i = 1, \ldots, L$ (or E2$_i$, $i = 1, \ldots, L$), which are all identical Q-SISO modules.

Due to the soft combining of channel estimates, the complexity of the quantized approach is quite high. For $L = 2$ diversity branches at the receiver, every full iteration of the joint estimator and turbo-decoder involves $2L = 4$ Forward-Backward runs on the K-state Q-SISOs (8 states here) with branch metrics computed as in (5.5)-(5.6), as well as two Forward-Backward runs on the 8-state constituent decoders "D1" and "D2" with branch metrics computed as in (5.10)-(5.14). Note that, because of the operation in the log-domain, multiplications in the above formulas become summations and summations become the max* operation (2.13). However, complexity is still an issue, so we limit the number of quantized phases to $K = 8$ (twice the cardinality of the 4-PSK constellation). The performance of this receiver is presented in section 5.3.

5.2.2 Optimum filtering approach

This section describes an alternative approach for iterative joint channel estimation and decoding, based on optimum filtering of received symbols (only pilots at the first iteration, coded symbols and pilots alike in subsequent iterations). Iterative filtering solutions have been proposed in [21] and in [20] for low-rate turbo-codes with BPSK constellations. The treatment here is general, and in fact can also cover non-PSK constellations, unlike the quantized phase approach in section 5.2.1. Nevertheless, we limit our simulations in section 5.3 to the familiar 8-state, 4-PSK turbo-code of Fig. 4.4.

With the filtering approach, the solid feedback lines in Fig. 5.3 are active (the dashed lines refer to the quantized phase approach). The purpose of the channel estimation modules E1$_i$, E2$_i$, $i = 1, \dots, L$, is to obtain estimates for the complex channel gains $a_1^{(i)}$, $a_2^{(i)}$, $i = 1, \dots, L$, and provide those estimates (after deinterleaving) to the appropriate constituent decoder "D1" or "D2". For this purpose, each estimator E1$_i$ (or E2$_i$) performs optimum (Wiener) filtering of received symbols at every iteration.

Intuitively, as decoder iterations proceed and more reliable knowledge about the coded symbols x is obtained, the estimators are able to provide better estimates of the channel gains $a^{(i)}$, in turn contributing to a better performance by the constituent decoders.

In the first iteration, when no knowledge about the transmitted symbols x, other than the pilots, is available, the estimators E1$_i$, E2$_i$, $i = 1, \dots, L$ are pilot filters. These filters are identical for all $2L$ diversity branches, and are derived as in Appendix A, given the filter length, the Doppler rate $f_D T$, the number D of coded symbols between pilot slots, the number Z of pilot symbols per slot, and the SNR. Specifically, the pilot-only filter (POF) W_k^o (where $k = 0, 1, \dots, D-1$ specifies the time index within the coded data slot between two adjacent pilot slots that the filter W_k^o is intended for) is an FIR filter, represented as a horizontal vector in (A.2):

$$W_k^o = R_{a_k,\tilde{y}} \cdot R_{\tilde{y}}^{-1}, \quad k = 0, 1, \dots, D-1, \tag{5.15}$$

where the entries of vector $R_{a_k,\tilde{y}}$ and matrix $R_{\tilde{y}}$ are computed in Appendix A. Those D distinct POFs are computed once, at the beginning of the simulation, and subsequently used for the first iteration of every turbo-coded block, by all $2L$ estimators. They filter received samples corresponding to pilots only (denote them $\tilde{y}^{(i)}$ after derotation of $y^{(i)}$ with the known pilot symbol x) and produce channel estimates $a_1^{(i)}$, $i = 1, \dots, L$ (and $a_2^{(i)}$, $i = 1, \dots, L$) to be used by the constituent decoders “D1” (and “D2”respectively).

Now consider how the constituent decoder “D1” (the same holds for “D2”, so we suppress the subscripts) uses the channel estimates $a^{(i)}$, $i = 1, \dots, L$, after deinterleaving, to compute the metric $\gamma_t(c', c)$. In essence the decoder performs maximal ratio combining of the L received samples $y_t^{(i)}$, $i = 1, \dots, L$, collected in the vector

$\mathbf{y}_t$ as follows:

$$\begin{aligned}
\gamma_t(c', c) &= \Pr\left(\mathbf{y}_t, C_t = c \middle|\, C_{t-1} = c'\right) && (5.16)\\
&= P\left(u_t \text{ such that } c' \to c\right) \cdot P\left(\mathbf{y}_t \mid \hat{\mathbf{a}}_t, x(c' \to c)\right) && (5.17)\\
&= P(u; I) \cdot (-G_1) \cdot \|\mathbf{y}_t - \hat{\mathbf{a}}_t\, x(c' \to c)\|^2 && (5.18)\\
&= P(u; I) \cdot G_2 \cdot \left(2\mathcal{R}\left\{\mathbf{y}_t^* \hat{\mathbf{a}}_t\, x(c' \to c)\right\} - \|\hat{\mathbf{a}}_t\|^2 |x(c' \to c)|^2\right), && (5.19)
\end{aligned}$$

where $\hat{\mathbf{a}}_t$ is the L-length vector comprising the estimates $a^{(i)}$, $i = 1, \ldots, L$, and $\mathcal{R}\{\cdot\}$ denotes the real part, and G_1, G_2 are irrelevant nonnegative constants. Note that in the case of PSK transmission, where all symbols x are of equal energy, the metric (5.19) can take the simpler form:

$$\gamma_t(c', c) = P(u; I) \cdot \mathcal{R}\left\{\mathbf{y}_t^* \hat{\mathbf{a}}_t\, x(c' \to c)\right\}. \qquad (5.20)$$

It is obvious that, although the inner product $\mathbf{y}_t^* \hat{\mathbf{a}}_t$ in (5.20) above involves L complex multiplications, the metric derived above for the decoder in the iterative filtering approach is still much simpler than the one in (5.14) for the “quantized approach”.

However, some additional complexity ensues in the filtering approach after the first iteration. The reason is that the estimation modules E1$_i$, E2$_i$, $i = 1, \ldots, L$ need estimates of the coded symbols (call those estimates $\hat{x}$) and cannot exploit the vectors $P(x; O)$ of extrinsic information about x, which is what the decoders “D1” and “D2” provide. This is why the nonlinearity “NonLin” is included in the (solid) feedback paths of Fig. 5.3. The purpose of this nonlinearity is to use the vector of probabilities $P(x; O)$ for every t and provide a hard estimate $\hat{x}$ for the coded symbol x, such that the filters E1$_i$, E2$_i$ can use $\hat{x}$ to improve their channel estimates in the next iteration.

A simple way to obtain $\hat{x}$ is to simply choose as $\hat{x}$ the constellation point x_m with the maximum $P(x; O)$, or:

$$\hat{x} = x_m \Longleftrightarrow P(x_m; O) \geq P(x_l; 0), \quad l = 0, 1, \ldots, M-1,\ l \neq m, \qquad (5.21)$$

where M is the constellation size. We refer to this type of nonlinearity as hard tentative decoding. A better way to obtain $\hat{x}$ is to use the soft information in $P(x;O)$ in a more sophisticated fashion. Recall that the entries of the vector $P(x;O)$ at each time are the log-probabilities of every constellation point x. Hence, it makes sense to set:

$$\hat{x} = \sum_{l=0}^{M-1} \Pr(x_l) \cdot x_l = \sum_{l=0}^{M-1} e^{P(x_l;O)} \cdot x_l. \tag{5.22}$$

In the simulations results presented in the next section we use the nonlinearity of (5.22), but the performance degradation if the simpler (5.21) is used is very small.

After the estimates for the coded symbols $\hat{x}$ have been produced for the whole block, the receiver replicates the operations of the transmitter, by interleaving them and adding pilot symbols (refer to Fig. 5.3, solid feedback path). So, at the input of the estimation blocks E1$_i$, E2$_i$, $i = 1, \ldots, L$, we now have an approximated replica of the transmitted sequence. In all iterations but the first, the estimators use this sequence to derotate the received samples $y_1^{(i)}$, $y_2^{(i)}$, $i = 1, \ldots, L$, so that Wiener filtering of the derotated $\tilde{y}_1^{(i)}$, $\tilde{y}_2^{(i)}$ can follow, to produce new channel estimates $\hat{a}_1^{(i)}$, $\hat{a}_2^{(i)}$. We call each of those Wiener filters—they are the same on all $2L$ diversity branches—an "all-symbol filter" (ASF), to distinguish it from the pilot-only filter (POF) W^o of (5.15), which is used only at the first iteration.

The ASF is easier to compute than the POF, because it only filters derotated samples that passed through the channel at adjacent times, unlike the POF, which only filters pilots. Moreover, there is only a single ASF for every time t, while a different POF W_k^o was needed for every position $k = 0, 1, \ldots, D-1$ between pilot slots. Assume the ASF is an FIR filter with $2L_1 + 1$ coefficients, stored in the vector Z^o. Then, from linear estimation theory (see [34]) and given the SNR and Doppler rate, the optimum ASF is given by:

$$Z^o = E a_k \tilde{y}^* \cdot \left[E \tilde{y} \tilde{y}^*\right]^{-1} = R_{a_k,\tilde{y}} \cdot R_{\tilde{y}}^{-1}, \tag{5.23}$$

where, analogous to Appendix A, $\tilde{\mathbf{y}}$ is a vector containing $2L_1+1$ derotated consecutive received samples:

$$\tilde{\mathbf{y}} = [\tilde{y}_{k-L_1}\ \tilde{y}_{k-L_1+1} \ldots \tilde{y}_{k+L_1}]^T = \mathbf{a} + \tilde{\mathbf{n}} \tag{5.24}$$

Hence, the entries of the horizontal vector $R_{a_k,\tilde{y}}$ are:

$$R_{a_k,\tilde{y}}(n) = \mathcal{J}_o\left(2\pi f_D T \cdot |L_1 - n|\right), \quad n = 0, 1, \ldots, 2L_1, \tag{5.25}$$

where $\mathcal{J}_o(\cdot)$ is the zero-order modified Bessel function of the first kind and the matrix $R_{\tilde{y}}$ is:

$$R_{\tilde{y}} = R_a + 2\sigma^2 \mathbf{I}_{2L_1+1}, \tag{5.26}$$

where the matrix $R_a = E\mathbf{a}\mathbf{a}^*$ is symmetric and Toeplitz, with entries:

$$R_a(n,m) = \mathcal{J}_o\left(2\pi f_D T \cdot |n - m|\right), \quad n, m = 0, 1, \ldots, 2L_1. \tag{5.27}$$

The ASF Z^o operates for every time t and at every diversity branch to yield updated channel estimates:

$$\hat{a}_t^{(i)} = Z^o \cdot \left[\tilde{y}_{t-L_1}^{(i)}\ \tilde{y}_{t-L_1+1}^{(i)} \ldots \tilde{y}_{t+L_1}^{(i)}\right]^T, \quad i = 1, \ldots, L, \quad t = 0, 1, 2, \ldots, N-1,$$

which are subsequently deinterleaved and provided to decoder “D1” or “D2” for the next algorithm iteration. The above filtering equation ignores the “edge-effects” at the beginning and end of turbo-coded blocks of N symbols, where there are not enough samples on either side of the symbol of interest to support two-sided filtering (i.e. smoothing). The same is true for pilot-only filtering and the POF in (5.15), which is also a two-sided filter (smoother). However, this problem can easily be solved either via inclusion of a few additional pilots at the edges of each block, or by designing special optimum filters to take into account those edge-effects. This is a minor problem for the filtering approach (also noticed in [21]), and it does not exist at all in the “quantized approach” because of the Markov approximation of the channel phase.

The complexity of the “filtering approach” is significantly less than that of the quantized approach for reasonable lengths of the POFs ($2L_0Z$) and the ASF ($2L_1+1$). But the receiver structure of Fig. 5.3 remains valid and describes both algorithms on a high level. Here, the estimator blocks E1$_i$, E2$_i$, $i = 1, \dots, L$ are FIR filters and not Forward-Backward algorithms, so there are only two Forward-Backward algorithms to run per iteration, those of the constituent decoders.

5.3 Simulation results

This section presents the simulated BER performance of the “quantized approach” presented in section 5.2.1 and the “filtering approach” of section 5.2.2 in a flat correlated Rayleigh fading channel with diversity order of $L = 2$. The turbo-code used throughout is the same as in Chapter 4, with 8-state constituent encoders, as shown in Fig. 4.4. The blocklength is $N = 4100$, and pilots are injected into the coded data stream at a rate of $Z \geq 1$ pilots every D coded 4-PSK symbols. The generic diagram of the iterative diversity receiver is that of Fig. 5.3, with the estimation blocks E1$_i$, E2$_i$, $i = 1, 2$, and the decoders “D1” and D2” as described previously for the two estimation methods. Two groups of simulations are presented, for Doppler rates $f_DT = 0.01$ and $f_DT = 0.05$ in Figs. 5.5 and 5.6 respectively.

We observe that for both Doppler rates, the filtering approach provides better performance than the quantized approach by more than 1 dB, and is also less intensive computationally, as pointed out before. For the quantized approach we used the familiar Markov model for the channel phase with $K = 8$ phase states, while for the filtering approach the simulation parameters were $L_0 = 5$ pilots on either side for the POF (i.e. total of 10 pilot symbols) for both Doppler rates, and $L_1 = 16$ for $f_DT = 0.01$ and $L_1 = 10$ for $f_DT = 0.05$ for the ASF (i.e. totals of 33 and 21 filtered symbols respectively). The number of iterations was 12 for $f_DT = 0.01$, and 10 for $f_DT = 0.05$,

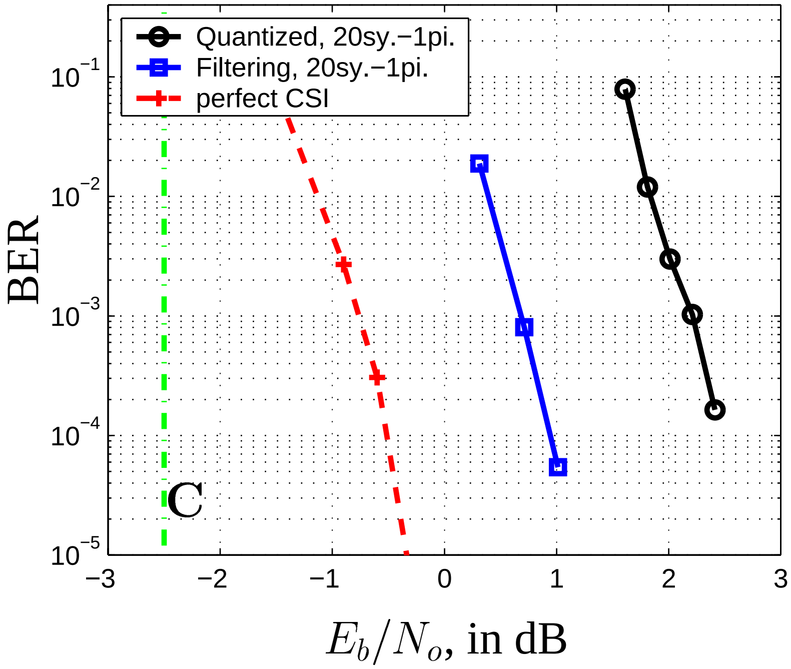

Figure 5.5: BER of turbo-code, for $f_D T = 0.01$ for the two channel estimation methods, and given perfect CSI. The vertical line marks the capacity given perfect CSI.

for both estimation methods, so the superior performance of the filtering approach in both Doppler rates comes with reasonable complexity.

In absolute values of SNR per information bit (E_b/N_o) the performance with both estimation methods (quantized and filtering) degrades for increasing Doppler rate, as seen in Figs. 5.5 and 5.6. Furthermore, the SNR gap between iterative estimation performance and performance achieved when perfect CSI is available at the receiver increases with increasing Doppler rate (e.g., with filtering, this SNR gap is 1.5 dB for $f_D T = 0.01$, and 3.2 dB for $f_D T = 0.05$). This happens despite the fact that perfect CSI performance itself improves with increasing Doppler, due to a larger amount of available time-diversity, and indicates, as noted also in Chapter 4, that the channel estimation problem becomes harder for increasing Doppler, which makes sense intu-

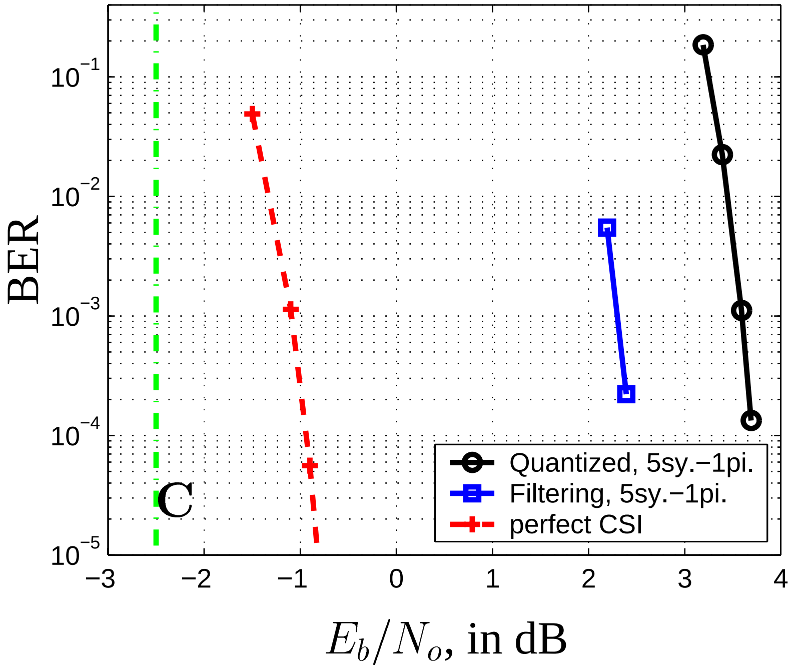

Figure 5.6: BER of turbo-code, for $f_D T = 0.05$ for the two channel estimation methods, and given perfect CSI. The vertical line marks the capacity given perfect CSI.

itively. In the limit of a channel fading independently, there is unlimited time-diversity to harvest given "genie-provided" CSI, but the estimation task becomes impossible in the absence of any time-correlation.

5.3.1 Capacity with receiver diversity

This section discusses channel capacity in the case where spatial diversity is available at the receiver. The results indicate that both algorithms discussed above indeed exploit the SNR advantage offered by diversity, and gain almost as much SNR because of it (with respect to operation without diversity) as the capacity improvement is. In the interest of keeping the capacity computation tractable, we restrict ourselves to time-independent fading (the assumption of independence across the L diversity channels always remains) and also assume perfect knowledge of the fading gains at the receiver.

Specifically, consider L-branch diversity reception in flat Rayleigh fading, where the received sample y_i at each branch is:

$$y_i = a_i \cdot x + n_i, \quad i = 1, \ldots, L, \tag{5.28}$$

and denote the SNR as $\rho = \frac{P_x}{N_o}$, where P_x is the average transmitted power of the constellation point x. Then, collecting all received values into a vector of length L:

$$\mathbf{y} = \mathbf{a} \cdot x + \mathbf{n}, \tag{5.29}$$

where all vectors $\mathbf{a}$ and $\mathbf{n}$ are assumed independent of each other and in time. The capacity of this vector channel, when there is no time constraint and given perfect channel knowledge at the receiver, is given by (see [2]):

$$C_L = \int \log_2(1 + \rho\, \mathbf{a}\mathbf{a}^*) P_{\mathbf{a}}(\mathbf{a}) d\mathbf{a}, \tag{5.30}$$

where $P_{\mathbf{a}}$ is the distribution of the fading vector $\mathbf{a}$. For instance, in the case of no fading (L-branch AWGN diversity) where $\mathbf{a} = \mathbf{1}_L$ always, we have that:

$$C_L^{\text{AWGN}} = \log_2(1 + \rho\, L), \tag{5.31}$$

in other words the intuitively pleasing result that the AWGN capacity with L diversity branches is the same as if the receiver has only one antenna, but the transmitter uses L times more power. In the specific case of $L = 2$, the SNR gain from diversity is 3 dB.

In Rayleigh fading, where each element (fading scale factor) a_i in the vector $\mathbf{a}$ is a zero-mean, unit variance complex Gaussian random variable —i.e. $a_i \sim \mathcal{N}_{\mathbb{C}}(0, 1)$— then it is expected that the SNR advantage due to diversity will be greater than 3 dB for $L = 2$, because of the “sphere-hardening” phenomenon. In other words, the L-fold receiver diversity helps in a dual fashion: it captures more of the transmitter power and stabilizes against channel spatial fluctuations [2]. This becomes obvious by writing the capacity of (5.30) with Rayleigh fading in the form:

$$C_L = \int \log_2 \left(1 + \rho \sum_{i=1}^{L} |a_i|^2 \right) P\left(|a_1|, \ldots, |a_L|\right) d|a_1| \cdots d|a_L|, \tag{5.32}$$

in which the argument of the logarithm points to the optimum combining receiver, the "maximal-ratio combiner". Fig. 5.7 shows the capacity against SNR for $L = 2$ and $L = 1$, and the separation between the two curves is greater than 3 dB for every SNR.

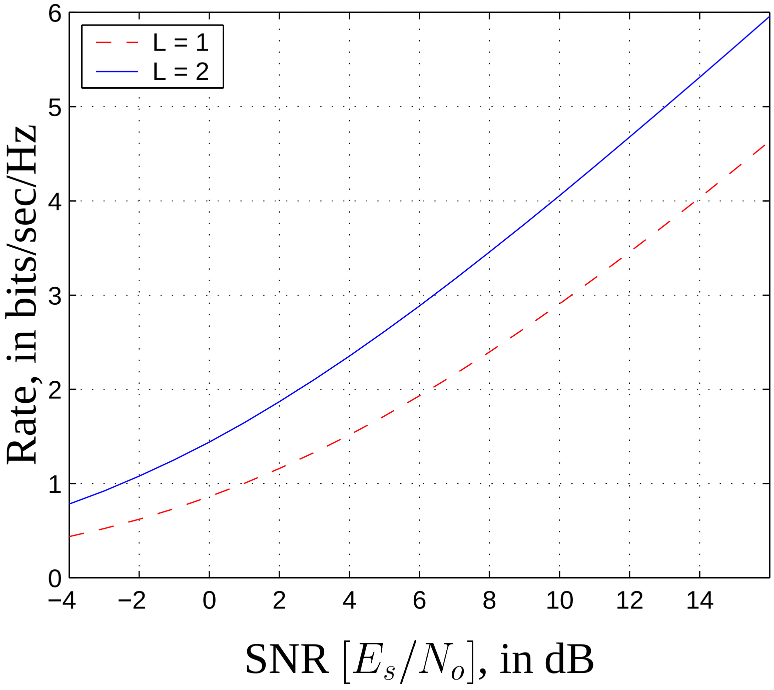

Figure 5.7: Capacity (with Gaussian inputs) for i.i.d. Rayleigh fading channels with receiver diversity orders of $L = 1$ and $L = 2$. Perfect channel knowledge at the receiver is assumed.

In particular, at the nominal rate of 1 bit/sec/Hz, where the turbo-code of this chapter operates (excluding the pilots) the diversity gain in capacity is 3.5 dB. And a comparison of the simulation results for the "quantized estimation" between Figs. 5.5 and 4.8, and also between Figs. 5.6 and 4.9, shows that the quantized algorithm in fact gains about 3-3.5 dB of SNR in both cases when the 2-fold diversity exists. The same is true for the “filtering approach” to iterative estimation, as became evident when we simulated this approach without diversity ($L = 1$).

For ease of comparison, Figs. 5.8 and 5.9 include results for Doppler rates $f_D T = 0.01$ and $f_D T = 0.05$ respectively, with diversity orders of $L = 1$ (dotted curves) and $L = 2$ (solid curves) of both receivers, along with the capacity vertical lines. It is clear that both iterative estimation algorithms benefit from the existence of 2-fold diversity approximately as much as the above capacity result would indicate (≈ 3.5 dB). In other words, both Figs. 5.8 and 5.9 show that the second branch of available spatial diversity at the receiver improves the simulated performance of both the “quantized” and the “filtering” iterative receivers by approximately the same amount that it enhances the channel capacity. The filtering approach maintains its superiority in performance over the quantized phase estimator both with and without diversity, as is obvious from the BER simulations in Figs. 5.8 and 5.9.

5.4 Conclusions

This first part of the dissertation (Chapters 2 through 5) discussed the problem of joint channel estimation and turbo-decoding in frequency-flat, time-correlated Rayleigh fading, without assuming the availability of perfect channel state information (CSI) at the receiver. Two methods based on the construction of a finite-state Markov model for the fading channel phase have been analyzed and simulated, with and without antenna diversity at the receiver. With the first method, the finite state machines of the channel and the code are combined to form a supertrellis, along which the channel and the data are jointly being estimated, without pilot symbols or channel interleaving. The second method employs separate trellises for decoding and phase estimation. This method uses pilot symbols and channel interleaving with higher rate codes, and provides good performance approaching a sequence of upper bounds to capacity with reasonable complexity. The estimation of channel phase and data is done jointly, on the supertrellis or on the separate trellises, via the Forward-Backward algorithm. Also, generalized iterative Wiener filtering is considered as an alternative for estimation, and shown to achieve good performance with high-rate trellis turbo-codes.

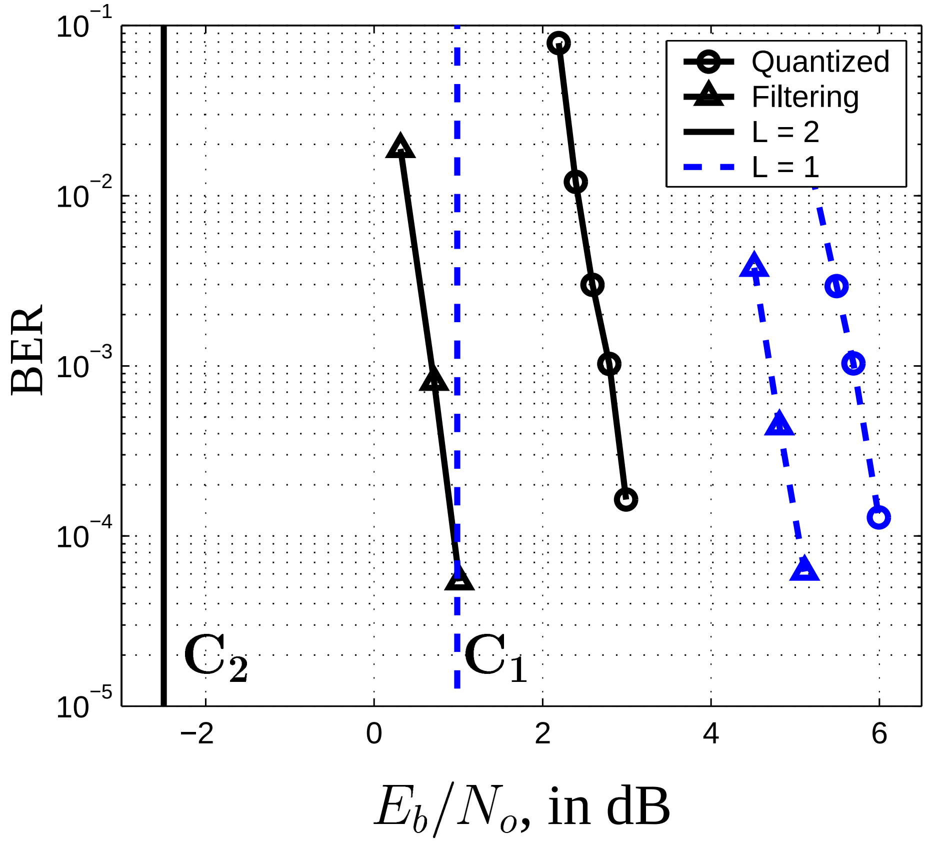

Figure 5.8: BER performance of turbo-code in flat Rayleigh fading with $f_D T = 0.01$, with diversity orders of $L = 2$ (solid curves) and $L = 1$ (dashed curves). The "quantized" approach for estimation is marked with "o", while the "filtering" approach with "$\triangle$". Vertical lines (solid and dashed) mark the respective capacities with Gaussian inputs and perfect CSI, for $L = 2$ and $L = 1$. Notice that pairs of similarly marked solid and dashed curves maintain an SNR distance of ≈ 3.5 dB, or that both quantized and filtering simulations improve with diversity about as much as capacity does.

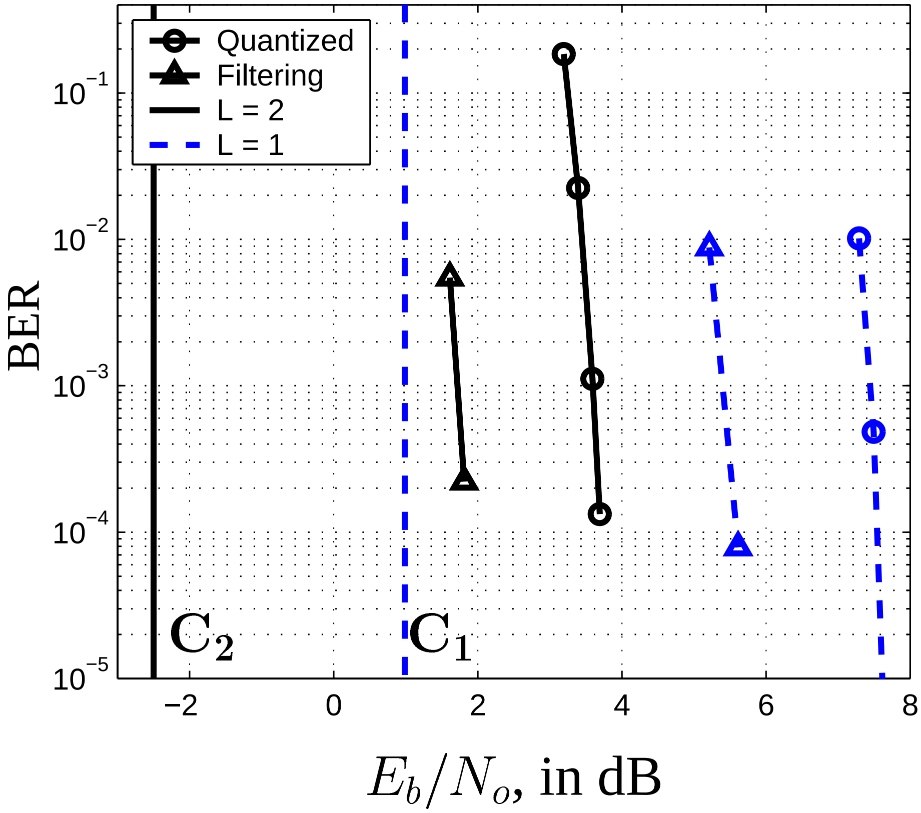

Figure 5.9: BER performance of turbo-code in flat Rayleigh fading with $f_D T = 0.05$. Naming conventions are the same as in Fig. 5.8. Again, notice that the second branch of diversity improves the simulations (dashed to solid curve with the same marker) by about as much as it improves the capacity (dashed to solid vertical line).

Part II

MIMO SYSTEMS IN FREQUENCY-SELECTIVE FADING

CHAPTER 6

MIMO Frequency-Selective Channel

6.1 Introduction

This second part of the dissertation addresses the problem of channel tracking and equalization for multi-input multi-output (MIMO) time-variant frequency-selective channels. These channels model the corrupting effects of inter-symbol interference (ISI), co-channel interference (CCI), and noise. The frequency selectivity of the channel arises in a MIMO (n_T, n_R) wireless system, where $n_T \geq 1$ is the number of transmitter antennas and $n_R \geq 1$ is the number of receiver antennas, as a result of relatively high transmission rates, whereby the transmission bandwidth exceeds the coherence bandwidth of the channel. Regarding the time-variant nature of the MIMO frequency-selective channel, this dissertation considers it to be significant within a packet of data, hence the need for channel tracking arises in order for the equalization to be effective. In other words, this and the next chapter consider the MIMO transmission problem for the important area of operation, where the transmission rate is high enough to generate resolvable multipath at the receiver, and at the same time the transmitted packet is long enough (or the transmission rate slow enough) to render an assumption of constant channel in every data burst inaccurate.

Most of the discussion of MIMO transmission in this and the next chapter is general enough to cover both the case of n_T independent users with one antenna each (which can be thought of as the multi-user detection problem, for instance in wideband multiple access systems [35], [36]), as well as the case of one user with coordinated transmissions through n_T antennas for higher data rate (which is akin to the systems of [2], [37]). This difference clearly has a big effect upon the choice of appropriate coding mechanisms for the MIMO system, discussed in Chapter 7, but does not affect the tracking procedure. For MIMO tracking we use a Kalman filter, aided by staggered decisions from a finite-length MMSE-DFE, which performs the task of equalization and separation of the sources.

An excellent review article [38] by Qureshi discusses adaptive equalization of a single-input single-output (SISO) dispersive channel ($n_T = n_R = 1$). For a fading SISO channel with ISI, a comprehensive review of the extensive research is [39]. In [40] we present a special case of the results in this dissertation, applicable to the SISO scenario. For array measurements at the receiver ($n_T = 1, n_R > 1$) an adaptive approach based on per-survivor-processing (PSP) is explored in [41]. The same case ($n_T = 1, n_R > 1$) but for flat fading (no ISI) was treated from the estimation and coding perspective in Chapter 5. But when more transmitters are sharing the bandwidth, there are two broad classes of techniques to combat co-channel interference (CCI) at the receiver. One is to suppress interference, possibly in an adaptive fashion, as in [42]. Another strategy is to decode all n_T data sequences simultaneously (e.g. [36]), possibly with a blind/adaptive approach [43]. The method we demonstrate in the next chapter embraces the second paradigm, with a few key differences from previous approaches.

First, we adopt the design of a finite-length MMSE-DFE from [44] for practical implementation. Then, we consider the channel taps to have significant time-variation from symbol to symbol, but with largely invariant specular mean and Doppler, which can be identified during a training phase. After that, in tracking mode, the Kalman filter and this finite MIMO DFE cooperate to adapt to the rapid channel variations.

It should be noted that, at least for the single-user (SISO) channel, Kalman-based estimation methods are quite common in the literature (e.g., [45] uses the extended Kalman filter to track a channel with unknown delays). Also, in [46] the Kalman approach is used to formulate extended forms of the Recursive Least-Squares (RLS) algorithm, and the tracking superiority of those is demonstrated compared to the standard RLS and Least Mean-Squares (LMS) algorithms.

In Chapter 7 we use a Kalman filter to track the time-variation of the MIMO channel taps. These taps are typically modeled as mutually uncorrelated circular complex Gaussian random processes, having locally constant means, due to large scale path loss, reflections and shadowing effects, as discussed in section 6.2. We assume the tap means known from a preceding training phase, and concentrate on tracking their time-variant part, which has autocorrelation properties corresponding to the wide-sense stationary and uncorrelated scattering "WSSUS" model of Bello [47]. If the tap means are zero, the channel is said to introduce Rayleigh fading (worst case), while a non-zero mean tap corresponds to Ricean fading. The Kalman channel estimator is aided by previous hard decisions about the transmitted symbols from all users, produced by the MIMO equalizer.

Assuming perfect knowledge of the MIMO channel, the optimum receiver is a maximum likelihood sequence estimator (MLSE), but its complexity is prohibitive, even for low order channels with a small number of inputs and outputs. In Chapter 7 we use the MIMO finite-length minimum-mean-squared-error decision-feedback equalizer (MMSE-DFE), developed in [44] and optimized for decision delay $\Delta \geq 0$. The choice of $\Delta > 0$ improves performance for a wide range of channels, as shown in [40] for the single-user channel. However, this delay poses the problem of channel prediction when combined with the Kalman tracking procedure mentioned above, because there is a time gap of Δ between channel estimates produced by the Kalman filter (aided by the delayed DFE decisions) and the channel estimates needed for the current DFE adaptation. We discuss simple methods to bridge this time gap, and show simulation results to demonstrate that the joint tracking and equalization algorithm proposed in Chapter 7 offers good performance. In fact, it outperforms conventional adaptive equalization algorithms, such as LMS or RLS, which do not have an explicit mechanism for incorporating the largely invariant channel statistics, such as the Doppler rate and the channel mean, in case they are known to the receiver from a previous training phase.

Finally, also in Chapter 7, we briefly outline channel coding strategies suitable for use with this channel estimation and equalization system. If the channel was constant and the n_T interfering data streams were perfectly decoupled and equalized, then the effective channel between transmitter and receiver after equalization would have a periodic (i.e. periodically time-varying) nature, as noticed in [48]. However, due to the estimation error by the Kalman filter and, more importantly, the finite length of the MIMO DFE, perfect decoupling is not possible. Our experiments show that while most of the ISI is cancelled, significant interference remains across the n_T data streams after equalization. Therefore, a space-time code designed in [37] outperforms a one-dimensional trellis code optimized for diversity and coding across transmitter antennas. Section 7.4 discusses the coding issue in more detail.

6.2 MIMO channel model

At every receiver antenna of the MIMO channel with n_T inputs and n_R outputs, a linear combination of all transmitted data sequences, each distorted by time-varying ISI, is observed under white Gaussian noise. Specifically, the observable $y_t^{(j)}$ from receiver j

(with $j = 1, \ldots, n_R$) at time t is:

$$y_t^{(j)} = \sum_{i=1}^{n_T} \sum_{m=0}^{\nu^{(i,j)}} c_m^{(i,j)}(t)\, x_{t-m}^{(i)} + v_t^{(j)} \tag{6.1}$$

where $c_m^{(i,j)}$ is the m^{th} tap of the impulse response of order $\nu^{(i,j)}$ between the i^{th} input $x^{(i)}$ and the j^{th} output $y^{(j)}$ of the MIMO channel. The complex baseband constellation point $x_{t-m}^{(i)}$ is transmitted by the i^{th} user at time $t - m$, and $v_t^{(j)}$ is the complex noise sample at the j^{th} receiver. In essence, there exist a total of $n_T n_R$ interfering, time-varying ISI channels $\mathbf{c}^{(i,j)}(t)$ (see Fig. 6.1 for a $(2, 2)$ system):

$$\mathbf{c}^{(i,j)}(t) = \left[c_0^{(i,j)}(t) \quad c_1^{(i,j)}(t) \ \ldots \ c_{\nu^{(i,j)}}^{(i,j)}(t)\right] \tag{6.2}$$

and each of their taps can be written as:

$$c_m^{(i,j)}(t) = \bar{c}_m^{(i,j)} + h_m^{(i,j)}(t), \quad m = 0, \ldots, \nu \tag{6.3}$$

where we define $\nu = \max_{i,j} \nu^{(i,j)}$, and set $c_m^{(i,j)}(t) = 0$ for $m > \nu^{(i,j)}$.

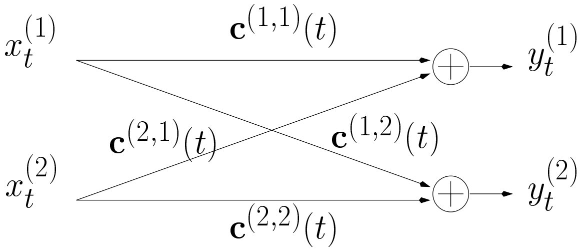

Figure 6.1: The interfering ISI channels in a $(2, 2)$ MIMO system.

The time-varying part $h_m^{(i,j)}(t)$ of each tap in (6.3) is a zero-mean, wide-sense-stationary complex Gaussian process, uncorrelated with any other $h_{m'}^{(i',j')}(t)$, and has time-autocorrelation properties governed by the Doppler rate $f_D T$, (T is the baud duration) as in [17]:

$$E\{h_m^{(i,j)}(t_1)[h_m^{(i,j)}(t_2)]^*\} \sim \mathcal{J}_o\left(2\pi f_D^{(i,j,m)} T |t_1 - t_2|\right) \tag{6.4}$$

where $\mathcal{J}_o(\cdot)$ is the zero-order Bessel function of the first kind. Notice that each of the $n_T n_R(\nu+1)$ taps varies independently (although this will not be essential in our development) and can have a different Doppler rate. More importantly, the autocorrelation functions are non-rational, hence no ARMA model is an exact representation of the time evolution of the channel taps. However, only the first few correlation terms (for small $|t_1 - t_2|$) are important for the design of any receiver. Thus, even low order autoregressive models, or even a simple Gauss-Markov model, can capture most of the channel tap dynamics and lead to effective tracking algorithms, as demonstrated below.

Analogous to a Single-Input, Single-Output (SISO) system with $n_T = n_R = 1$, we can write the MIMO channel input-output relationship in vector form as a matrix FIR filter. By collecting the outputs $y_t^{(j)}$ of (6.1) from all receiver antennas at time t into a n_R-dimensional column vector $\mathbf{y}_t$:

$$\mathbf{y}_t = \sum_{m=0}^{\nu} \mathbf{C}_m(t)\mathbf{x}_{t-m} + \mathbf{v}_t, \tag{6.5}$$

where $\mathbf{y}_t$ and $\mathbf{v}_t$ are column vectors of length n_R, $\mathbf{x}_{t-m}$ are column vectors of length n_T, and $\mathbf{C}_m(t)$ are $n_R \times n_T$ matrix channel taps (instead of the scalar SISO taps). Each of the matrices $\mathbf{C}_m(t)$, $m = 0, \ldots, \nu$ contains the tap $c_m^{(i,j)}(t)$ of (6.1) and (6.3) in its $(j,i)^{\text{th}}$ position. This formulation of the MIMO channel (6.5) is useful in the DFE design of section 7.1.2, but for the purpose of MIMO channel tracking via the Kalman filter, presented in section 7.1.1, we will need an alternative notation for the input-output relationship, of the form:

$$\mathbf{y}_t = \mathbf{X}_t \cdot \mathbf{c}_t + \mathbf{v}_t, \tag{6.6}$$

where the $n_R \times n_R n_T(\nu+1)$ data matrix $\mathbf{X}_t$ is a “wide” matrix with the transmitted symbols repeated diagonally, according to the Kronecker product:

$$\mathbf{X}_t = \left[x_t^{(1)} \ldots x_t^{(n_T)}\, x_{t-1}^{(1)} \ldots x_{t-1}^{(n_T)} \,\ldots\, x_{t-\nu}^{(1)} \ldots x_{t-\nu}^{(n_T)}\right] \otimes \mathbf{I}_{n_R} \tag{6.7}$$

and $\mathbf{c}_t$ is a long vector of length $n_T n_R(\nu+1)$ containing all the channel taps at time t, $\mathbf{c}_t = \bar{\mathbf{c}} + \mathbf{h}_t$:

$$\begin{aligned}\mathbf{c}_t = \Big[& c_0^{(1,1)}(t) \dots c_0^{(1,n_R)}(t) \dots \; c_0^{(n_T,1)}(t) \dots c_0^{(n_T,n_R)}(t) \dots \\ & c_\nu^{(1,1)}(t) \dots c_\nu^{(1,n_R)}(t) \dots \; c_\nu^{(n_T,1)}(t) \dots c_\nu^{(n_T,n_R)}(t)\Big]^T . \end{aligned} \tag{6.8}$$

With this setup, the channel is a complex Gaussian vector process $\mathbf{c}_t$ with dimensions $(n_T n_R(\nu+1)) \times 1$, which has a constant mean vector $\bar{\mathbf{c}}$. The time-variant part of the channel is the vector process $\{\mathbf{h}_t\}$. According to the WSSUS model of Bello [47], all the channel taps are independent, namely all the entries of vector $\mathbf{h}_t$ vary independently, according to the autocorrelation model of (6.4). If we let index k enumerate all the taps $k = 1, \dots, n_T n_R(\nu+1)$, and denote $f_D^{(k)} = f_D^{(i,j,m)}$ the Doppler of the m^{th} tap of the channel from input i to output j, then the normalized spectrum for each tap $\{h_t^{(k)}\}$ is:

$$S_k(f) = \begin{cases} \dfrac{1}{\pi f_D^{(k)} T} \dfrac{1}{\sqrt{1 - \left(\dfrac{f}{f_D^{(k)} T}\right)^2}}, & |f| < f_D^{(k)} T \\ 0, & \text{otherwise} \end{cases} \tag{6.9}$$

Exact modeling of the vector process $\{\mathbf{h}_t\}$ with an autoregressive (AR) model is impossible. For implementation of a Kalman filter, we approximate the MIMO channel variation $\{\mathbf{h}_t\}$ with the following multichannel AR process of order p, as done in [49] for $n_T = n_R = 1$:

$$\mathbf{h}_t = \sum_{l=1}^{p} \mathbf{A}(l)\mathbf{h}_{t-l} + \mathbf{G}\mathbf{w}_t, \tag{6.10}$$

where $\mathbf{w}_t$ is a zero-mean i.i.d. circular complex Gaussian vector process with correlation matrices $\mathbf{R}_{ww}(j)$ for every lag j given by $\mathbf{R}_{ww}(j) = E\{\mathbf{w}_t \mathbf{w}_{t+j}^*\} = \mathbf{I}_{n_T n_R(\nu+1)}\delta(j)$. Due to the WSSUS assumption, the matrices $\mathbf{A}(l)$, $l = 1, \dots, p$ and $\mathbf{G}$ of the model (6.10) must be diagonal. For the selection of their diagonal entries, various criteria of optimality can be adopted, such that the AR(p) model of (6.10) would be a "best-fit" to the true channel autocorrelation of (6.4). One such criterion can be to require the process (6.10) to be such that 90% of the energy spectrum of each tap is contained in the frequency range $|f| < f_D^{(k)}T$, as indicated by (6.9).

For simplicity we adopt a first-order AR model ($p = 1$) and denote $\mathbf{F} = \mathbf{A}(1)$. So, (6.10) becomes:

$$\mathbf{h}_t = \mathbf{F}\mathbf{h}_{t-1} + \mathbf{G}\mathbf{w}_t \tag{6.11}$$

Then we fix the diagonal entries of matrices $\mathbf{F}$ and $\mathbf{G}$ (call them f_k and g_k respectively) to capture the most essential parts of the channel variation, namely how "fast" and how "much" the time-varying part $h^{(k)}$ of each channel tap varies with respect to the mean of that tap $\bar{c}_k$. The speed of variation is determined by the Doppler, or equivalently by the relative velocity between the n_T antennas of the transmitter and the n_R antennas of the receiver. At least for the scenario of coordinated transmission, the assumption of equal Doppler rates $f_D^{(k)}T = f_DT$, $k = 1, \ldots, n_Tn_R(\nu + 1)$ makes intuitive sense, so we adopt it in the simulations, although the algorithm derivation certainly does not rely on that. The diagonal entries of $\mathbf{F}$ are all $f_k = f = \mathcal{J}_o\left(2\pi f_DT\right)$, and this choice sets the autocorrelation of the taps modeled by (6.11) to equal the true autocorrelation at unit lag. Obviously, larger Doppler rate f_DT implies smaller $f_k = f$, hence faster channel variation.

Having fixed the *rate* of channel variation via $\mathbf{F}$, the magnitude of variation of the k^{th} tap is then controlled by the diagonal entries g_k of $\mathbf{G}$, since the power of the time-variant part of each tap is $E|h^{(k)}|^2 = \frac{g_k^2}{1-f^2}$, from (6.11). The amount of variation of each tap with respect to the mean is expressed by the "specular-to-diffuse power ratio" K_k, as follows:

$$K_k \overset{\text{def}}{=} 10\log\left(\frac{|\bar{c}_k|^2}{E\{|h^{(k)}|^2\}}\right) = 10\log\left(\frac{|\bar{c}_k|^2}{g_k^2/(1-f_k^2)}\right) \tag{6.12}$$

The ratio K_k indicates the ratio of power of the k^{th} mean channel tap to the mean-squared power of the random, time-variant part of that tap, analogous to the Ricean factor defined in the wireless channel literature. Clearly, $K = -\infty$ dB corresponds to Rayleigh taps, while large positive values of K in dB represent almost no channel variation at all. In the simulations of Chapter 7, although again it is arbitrary, we choose equal values of $K_k = K$ for all the taps.

Although higher order models than (6.11) can be constructed for larger p, it turns out that this simple first-order approximation is enough to model the channel dynamics to the extent necessary for a receiver to operate. For perspective, in a 2.4 GHz transmission with baud rate of 20 KHz and Doppler frequency $f_D = 200$ Hz (corresponding to vehicular velocity of 90 Km/h or 56 mph), then $f_D T = 0.01$ and $f_k = 0.999$. Also, a value of $K = 6$ dB implies that the average power of each tap variation is one-fourth of the constant mean tap value.

For the SISO case (i.e. $n_T = 1, n_R = 1$) a useful method to obtain the sequence of matrices $\mathbf{A}(l),\ l = 1, \ldots, p$ during a training mode is provided in [49], via higher-(than-second)-order statistics (HOS). Their method is effective and requires only reasonable assumptions about the transmitted sequence and the noise. An analogous training method can be adopted for general MIMO channels. But the way we formulated the AR(1) model of (6.11) here, the information needed to construct the model is only the channel mean $\bar{\mathbf{c}}$, the Doppler rates, the ratios K_k and the noise variance. Hence, we assume that these quantities are known from a training phase, and focus on decision-aided tracking of the channel for relatively long time spans, without retraining.

CHAPTER 7

Receiver Structure and Performance

7.1 Receiver structure

The receiver uses a Kalman filter to track the channel and a DFE to equalize it. The Kalman filter assumes that the DFE hard decisions are correct and uses them to estimate the next channel value, while the DFE assumes correct Kalman filter channel estimates, and uses them in turn to equalize the channel. In general, the optimum decision delay $\Delta \geq 0$ can be determined analytically given a channel (see [44]). For a wide range of channels (including, but not limited to, non-minimum-phase channels), it turns out that a DFE producing decisions with $\Delta > 0$ is optimal. Even for the few channels where $\Delta = 0$ is best, it doesn't degrade performance to use a DFE with $\Delta > 0$, provided there are enough taps in the feedforward and feedback filters. Thus, it makes sense, particularly for time-varying channels like the ones treated here, to use decision delays $\Delta > 0$.

But when $\Delta > 0$, a time gap is created. At time t, when the last received vector is $\mathbf{y}_t$, the DFE produces the hard-decision $\hat{\mathbf{x}}_{t-\Delta}$. The staggered decisions cause the Kalman filter to operate with delay, that is, operate at time $t - \Delta$, since it only has available hard decisions from the DFE up to then. However, the DFE design still needs channel estimates up to time t. Thus the receiver needs to use channel prediction to bridge the time gap between the Kalman channel estimation and the channel estimates needed for the current DFE adaptation.

The proposed system block diagram of Fig. 7.1 shows the time succession of steps (1) through (4) below. The notation $\mathbf{z}_{n_1}^{n_2}$ (or $z_{n_1}^{n_2}$) means the collection of vector valued (or scalar) variables $\mathbf{z}_{n_1} \ldots \mathbf{z}_{n_2}$ (or $z_{n_1} \ldots z_{n_2}$). In Fig. 7.1 the flow of new information is clockwise, starting from top left, with each of the blocks corresponding to one of the following actions:

1. $\hat{\mathbf{h}}_{t-\Delta} = \mathcal{K}\big(\hat{\mathbf{h}}_{t-\Delta-1}, \mathbf{y}_{t-\Delta-1}, \hat{\mathbf{x}}_{t-\Delta-\nu-1}^{t-\Delta-1}\big)$
2. $\hat{\mathbf{h}}_{t-\Delta+1}^{t} = \mathcal{P}\left(\hat{\mathbf{h}}_{t-\Delta}, \mathbf{y}_{t-\Delta}^{t}\right)$
3. $\left[\mathbf{W}_t^{opt}, \mathbf{B}_t^{opt}\right] = \text{design DFE}(\hat{\mathbf{h}}_{t-N_f}^{t})$
4. $\hat{\mathbf{x}}_{t-\Delta} = \text{ DFE}(\mathbf{W}_t^{opt}, \mathbf{B}_t^{opt})$

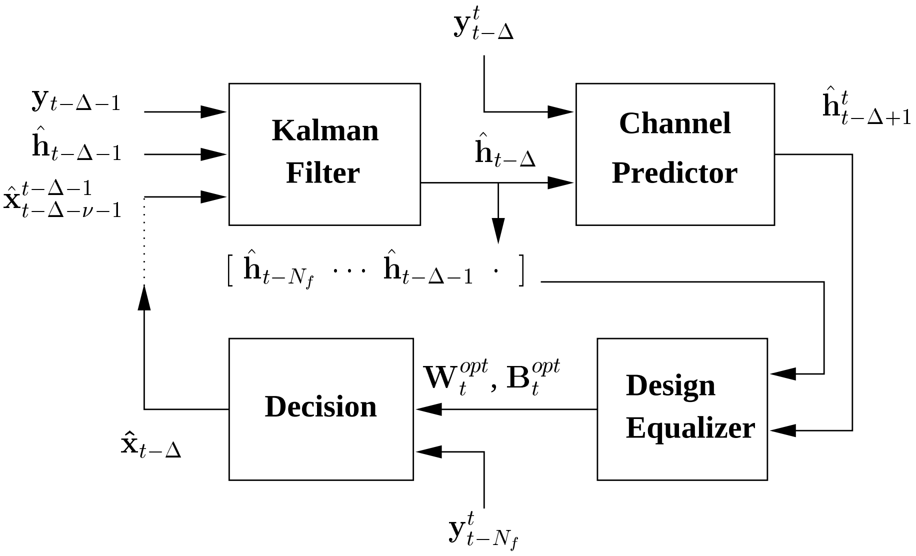
$\mathbf{y}_{t-\Delta}^{t}$
$\mathbf{y}_{t-\Delta-1}$
$\hat{\mathbf{h}}_{t-\Delta-1}$
$\hat{\mathbf{x}}_{t-\Delta-\nu-1}^{t-\Delta-1}$
Kalman Filter
$\hat{\mathbf{h}}_{t-\Delta}$
Channel Predictor
$\hat{\mathbf{h}}_{t-\Delta+1}^{t}$
$[\ \hat{\mathbf{h}}_{t-N_f}\ \cdots\ \hat{\mathbf{h}}_{t-\Delta-1}\ \cdot\ ]$
Decision
$\mathbf{W}_t^{opt}, \mathbf{B}_t^{opt}$
Design Equalizer
$\hat{\mathbf{x}}_{t-\Delta}$
$\mathbf{y}_{t-N_f}^{t}$

Figure 7.1: MIMO Receiver block diagram.

The iteration starts with the well-known Kalman filter recursions denoted by $\mathcal{K}(\cdot)$, which at time t yield the optimum linear estimator (based on our AR model) of the time-varying part of the channel $\hat{\mathbf{h}}_{t-\Delta}$ as it was at time $t-\Delta$. For that, the Kalman filter relies on the (assumed reliable) DFE decisions $\hat{\mathbf{x}}_{t-\Delta-1}, \ldots, \hat{\mathbf{x}}_{t-\Delta-\nu-1}$, the received vector $\mathbf{y}_{t-\Delta-1}$ and the previously estimated channel vector $\hat{\mathbf{h}}_{t-\Delta-1}$. In the second step, $\mathcal{P}(\cdot)$ denotes a predictor that may exploit the additional received vectors $\mathbf{y}_t, \ldots \mathbf{y}_{t-\Delta}$, along with the last Kalman estimate $\hat{\mathbf{h}}_{t-\Delta}$ to compute the sequence of Δ predicted channels $\hat{\mathbf{h}}_t, \ldots, \hat{\mathbf{h}}_{t-\Delta+1}$.

Those Δ predicted channels, along with the $N_f - \Delta$ most recent channel estimates from the Kalman filter, are used by the DFE design module (see Sect. 7.1.2) to design the optimum feedforward matrix filter, $\mathbf{W}_t^{opt}$, and the feedback matrix filter, $\mathbf{B}_t^{opt}$ of an MMSE DFE. Finally, the newly designed DFE decodes one more n_T-dimensional symbol $\hat{\mathbf{x}}_{t-\Delta}$, which is added to the collection of past (assumed reliable) decisions, which will help the Kalman filter make a new channel estimate $\hat{\mathbf{h}}_{t-\Delta+1}$ at the next iteration, taking place at time instant $t+1$. In the following subsections we look at the implementation of the two main receiver modules in greater detail.

7.1.1 Kalman tracking and channel prediction

For simplicity, we limit our discussion to the AR(1) channel model of (6.11), but the extension to higher order AR models is straightforward. The channel at time t has a constant (assumed known) mean $\bar{\mathbf{c}}$ and a zero-mean time-varying part $\mathbf{h}_t$, which follows the AR(1) model:

$$\mathbf{h}_{t+1} = \mathbf{F}\mathbf{h}_t + \mathbf{G}\mathbf{w}_t. \tag{7.1}$$

At time t, the (zero-mean) received vector $\mathbf{y}_t$ is given by:

$$\mathbf{y}_t = \mathbf{X}_t \cdot (\bar{\mathbf{c}} + \mathbf{h}_t) + \mathbf{v}_t. \tag{7.2}$$

Assuming the matrices $\mathbf{F}$ and $\mathbf{G}$ and the mean channel vector $\bar{\mathbf{c}}$ are known from a preceding training phase, and assuming the matrix of the most recent available decisions $\hat{\mathbf{X}}_{t-\Delta-1}$ to be equal to the true $\mathbf{X}_{t-\Delta-1}$ defined in (6.7), the receiver can use the Kalman filter to track the channel variation $\mathbf{h}_{t-\Delta}$, using as observable the vector $\mathbf{y}_{t-\Delta-1} - \hat{\mathbf{X}}_{t-\Delta-1}\bar{\mathbf{c}}$. The Kalman filter, operating with a delay Δ is described at time t by the series of equations [34]:

$$\begin{aligned}
\hat{\mathbf{h}}_{t-\Delta} &= \mathbf{F}\hat{\mathbf{h}}_{t-\Delta-1} + \mathbf{K}_{t-\Delta-1}\mathbf{e}_{t-\Delta-1} \\
\mathbf{e}_{t-\Delta-1} &= \mathbf{y}_{t-\Delta-1} - \hat{\mathbf{X}}_{t-\Delta-1}(\hat{\mathbf{h}}_{t-\Delta-1} + \bar{\mathbf{c}}) \\
\mathbf{K}_{t-\Delta-1} &= (\mathbf{F}\mathbf{P}_{t-\Delta-1}\hat{\mathbf{X}}^{*}_{t-\Delta-1})\mathbf{R}^{-1}_{e,t-\Delta-1} \\
\mathbf{R}_{e,t-\Delta-1} &= \mathbf{R}_{vv} + \hat{\mathbf{X}}_{t-\Delta-1}\mathbf{P}_{t-\Delta-1}\hat{\mathbf{X}}^{*}_{t-\Delta-1} \\
\mathbf{P}_{t-\Delta} &= \mathbf{F}\mathbf{P}_{t-\Delta-1}\mathbf{F}^{*} + \mathbf{G}\mathbf{G}^{*} \\
&\quad -\mathbf{K}_{t-\Delta-1}\mathbf{R}_{e,t-\Delta-1}\mathbf{K}^{*}_{t-\Delta-1}.
\end{aligned}$$

The above Kalman recursions implement the optimum linear estimator for the time-varying part of the channel $\mathbf{h}_{t-\Delta}$. The last reliable decision made by the DFE and used by the Kalman filter at this time is $\hat{\mathbf{x}}_{t-\Delta-1}$. For matrices $\mathbf{F}$ and $\mathbf{G}$ that are multiples of the identity (produced, for instance, by uncorrelated fading with the same Doppler and ratio K_k for all taps) fast algorithms for the above Kalman recursions can be pursued (see, e.g., [50]). Note that for the block-constant fading channel model adopted in the space-time literature [37], nothing else changes in the model of (7.1), except for setting $\mathbf{F} = \mathbf{I}$ and $\mathbf{G} = 0$, which simplifies the above Kalman recursions significantly. This makes the Ricean factors K_k in (6.12) useless, because if the channel remains unchanged for the whole block, the distinction between the mean $\bar{\mathbf{c}}$ and $\mathbf{h}$ in (6.8) is arbitrary. However, in this case of block constant channel, adaptation of the MIMO DFE at every time is not warranted. A few iterations of the algorithm at the beginning of each block should be enough to adapt the matrix coefficients to the constant channel. Then their values can remain fixed for the rest of the block.

In channels with smaller coherence time (higher Doppler) adapting the MIMO

DFE every time instant improves performance. For designing the DFE at time t (step 3), the N_f most recent channel estimates are needed, where N_f is the order of the matrix feedforward filter $\mathbf{W}^{opt}$ of the DFE. Up to time $t-\Delta$ channel estimates are available from the Kalman filter. But the last Δ channel vectors $\hat{\mathbf{h}}_t, \ldots, \hat{\mathbf{h}}_{t-\Delta+1}$ have to be predicted. The implementation of the prediction depends upon the SNR of operation and how fast the channel varies. For the block-constant channel or a very slowly varying one, the simplest choice is to assume that the channel remains constant over Δ sampling periods, that is:

$$\hat{\mathbf{h}}_t = \hat{\mathbf{h}}_{t-1} = \cdots = \hat{\mathbf{h}}_{t-\Delta} \tag{7.3}$$

where $\hat{\mathbf{h}}_{t-\Delta}$ is already provided by the Kalman filter.

More generally, the optimal linear predictions, given that the channel follows the AR(1) model of (7.1), but ignoring the additional received vectors $\mathbf{y}_t, \ldots, \mathbf{y}_{t-\Delta}$ are:

$$\hat{\mathbf{h}}_t = \mathbf{F}^{\Delta}\hat{\mathbf{h}}_{t-\Delta}, \ldots, \hat{\mathbf{h}}_{t-\Delta+1} = \mathbf{F}\hat{\mathbf{h}}_{t-\Delta} \tag{7.4}$$

where again $\hat{\mathbf{h}}_{t-\Delta}$ is the last Kalman channel estimate.

The received vectors $\mathbf{y}_t, \ldots, \mathbf{y}_{t-\Delta}$, which are also available, can be used to improve the prediction for a fast varying channel at high SNR. For example, one could formulate and optimize least-squares cost functions $J(\mathbf{h})$, forcing the predicted channel vectors $\hat{\mathbf{h}}_k, k = t, \ldots, t-\Delta+1$ to the vicinity of the values of (7.4), weighted by how well a certain $\hat{\mathbf{h}}_k$ “justifies” the received vectors $\mathbf{y}_t, \ldots, \mathbf{y}_{t-\Delta}$ (see [40]). We do not pursue this prediction avenue in this chapter, and all simulations are done using (7.4) for channel prediction.

7.1.2 DFE design

The design of the optimum MMSE feedforward and feedback matrix filters $\mathbf{W}^{opt}$ and $\mathbf{B}^{opt}$ of lengths N_f and N_b matrix taps respectively, as well as the optimum selection of the delay Δ for any (n_T, n_R) system is solved in [44] and will not be repeated here. It is an MMSE design, in the sense that it minimizes both the trace and the determinant of the autocorrelation matrix $\mathbf{R}_{ee}$ of the error vector $\mathbf{e}_t = \tilde{\mathbf{x}}_t - \mathbf{x}_t$, where $\tilde{\mathbf{x}}_{t-\Delta}$ is the vector with the n_T equalized soft values at time t, as seen in Fig. 7.2. For the design, the assumption is made that there is no error propagation, i.e. the hard decision vector $\hat{\mathbf{x}}_{t-\Delta}$ is the same as the transmitted vector $\mathbf{x}_{t-\Delta}$.

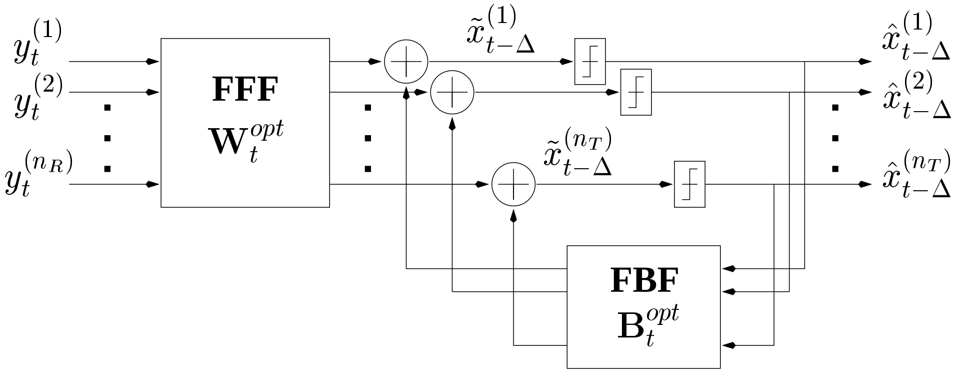
$y_t^{(1)}$
$y_t^{(2)}$
$y_t^{(n_R)}$
FFF
$\mathbf{W}_t^{opt}$
$\tilde{x}_{t-\Delta}^{(1)}$
$\tilde{x}_{t-\Delta}^{(n_T)}$
$\hat{x}_{t-\Delta}^{(1)}$
$\hat{x}_{t-\Delta}^{(2)}$
$\hat{x}_{t-\Delta}^{(n_T)}$
FBF
$\mathbf{B}_t^{opt}$

Figure 7.2: MIMO DFE block diagram.

In [44], various design methodologies are given, depending on whether there is a feedback filter or not (in which case the design is that of an MMSE linear MIMO equalizer). The choice of oversampling is also available without significant changes to the derivation. For the DFE an important design choice is whether *current* decisions of stronger users are available, or only past decisions from every user. The former case would correspond to a successive cancellation scheme, and would provide better performance at the cost of added complexity to order the n_T users according to their power before DFE operation.

Here we avoid the extra complexity by designing a symbol-spaced MIMO DFE where only past decisions for all users are available and go into the feedback matrix filter $\mathbf{B}^{opt}$. Clearly this choice of strictly causal feedback filtering has a consequence: while it permits almost perfect cancellation of the ISI and cross-ISI, it does not completely suppress residual cross-coupling. In other words, the i^{th} entry $\tilde{x}_t^{(i)}$ of the equalized vector $\tilde{\mathbf{x}}_t$ is almost devoid of the corrupting presence of all $x_{t-k}^{(j)}$, $k \neq 0, j = 1, \ldots, n_T$, but the presence of current other symbols $x_t^{(j)}$, $j \neq i$, in it is nulled somewhat less effectively.

We do not replicate the equations for optimum design of $\mathbf{W}^{opt}$ and $\mathbf{B}^{opt}$ here. Suffice it to say that an essential part of the DFE design at every time instant t is the formulation of the $n_R N_f \times n_T(N_f + \nu)$ block pre-windowed channel matrix $\mathbf{H}$:

$$\mathbf{H} = \begin{bmatrix} \hat{\mathbf{C}}_0^t & \cdots & \hat{\mathbf{C}}_\nu^t & \mathbf{0} & \cdots & \mathbf{0} \\ \mathbf{0} & \hat{\mathbf{C}}_0^{t-1} & \cdots & \hat{\mathbf{C}}_\nu^{t-1} & \mathbf{0} & \cdots \\ \vdots & & & & & \vdots \\ \mathbf{0} & \cdots & \mathbf{0} & \hat{\mathbf{C}}_0^{t-N_f+1} & \cdots & \hat{\mathbf{C}}_\nu^{t-N_f+1} \end{bmatrix} \tag{7.5}$$

where $\hat{\mathbf{C}}_m^k, m = 0, 1, \ldots, \nu,\ k = t, t-1, \ldots, t - N_f + 1$ are the estimates of the $n_R \times n_T$ channel matrices $\mathbf{C}_m(k)$ in (6.5). It is obvious that constructing $\mathbf{H}$ of (7.5) merely involves adding the constant part $\bar{\mathbf{c}}$ to the long vector estimates $\hat{\mathbf{h}}_k$, $k = t, t-1, \ldots, t - N_f + 1$ of the time-varying part of the channel (some of which are estimated via the Kalman filter and some are predicted), and then rearranging the resulting long vectors into the dimensions specified by Eq. (6.5). After the matrix $\mathbf{H}$ of (7.5) has been formed, the MIMO DFE design procedure described in [44] is straightforward, and also provides the correlation matrix $\mathbf{R}_{ee}$ of the error vector as a by-product. Fast Cholesky factorization improves the computational efficiency of this finite-length MIMO DFE design, playing a role parallel to that of spectral factorization for matrix filters of infinite length.

7.2 Baseline adaptive systems

In this section we outline conventional adaptive algorithms for the DFE, such as LMS and RLS for the case of n_T transmitters and n_R receivers. These adaptation mechanisms, unlike the Kalman-aided DFE presented above, do not estimate the channel explicitly. Instead, they adapt the DFE matrix taps, based on observed symbols from the time-variant channel, and hard decisions from the equalizer. LMS and RLS will serve as baseline systems, the performance of which will be compared to the Kalman-aided DFE through simulations in the next section. For both algorithms, consider the concatenation of the $n_T \times n_R N_f$ matrix FF filter and the $n_T \times n_T N_b$ matrix FB filter of the DFE into an $n_T \times (n_R N_f + n_T N_b)$ equalizer filter $\mathbf{Q} = [\mathbf{W} \quad \mathbf{B}]$. At time t, this equalizer filter $\mathbf{Q}_t$ operates on the column "regressor" vector $\mathbf{u}_t$ of length $n_R N_f + n_T N_b$:

$$\mathbf{u}_t = [\mathbf{y}_t^T \dots \mathbf{y}_{t-N_f+1}^T \; \hat{\mathbf{x}}_{t-\Delta-1}^T \dots \hat{\mathbf{x}}_{t-\Delta-N_b}^T]^T \tag{7.6}$$

The operation produces a vector $\tilde{\mathbf{x}}_{t-\Delta}$ of n_T soft values, which are then fed to n_T slicers, as in Fig. 7.2, producing a vector of hard decisions $\hat{\mathbf{x}}_{t-\Delta}$. Under the MMSE criterion, each row $\mathbf{q}_i, i = 1, \dots, n_T$ of the equalizer $\mathbf{Q}_t$ is responsible for the minimization of the cost function:

$$J(\mathbf{q}_i) = |x_{t-\Delta}^{(i)} - \mathbf{q}_i \cdot \mathbf{u}|^2 = |\hat{x}_{t-\Delta}^{(i)} - \mathbf{q}_i \cdot \mathbf{u}|^2, \quad i = 1, \dots, n_T, \tag{7.7}$$

with the high-SNR assumption of no decision errors. In the absence of knowledge of the correlations $R_{x^{(i)}\mathbf{u}} = Ex^{(i)}\mathbf{u}^*$ and $R_{\mathbf{u}} = E\mathbf{u}\mathbf{u}^*$, we can use the corresponding instantaneous approximations $\hat{x}^{(i)}\mathbf{u}^*$ and $\mathbf{u}\mathbf{u}^*$ in their place. This leads to the following LMS recursions, which iteratively approximate the least-mean-square solution (see [34]) separately for $i = 1, \dots, n_T$:

$$\mathbf{q}_i(t) = \mathbf{q}_i(t-1) + \mu[\hat{x}_{t-\Delta}^{(i)} - \mathbf{q}_i(t-1) \cdot \mathbf{u}_t]\mathbf{u}_t^*. \tag{7.8}$$

Those n_T simultaneous LMS recursions for the rows $\mathbf{q}_i$ of $\mathbf{Q}$ can be combined into one, for the entire DFE $\mathbf{Q}$:

$$\text{MIMO LMS: } \mathbf{Q}_t = \mathbf{Q}_{t-1} + \mu[\hat{\mathbf{x}}_{t-\Delta} - \mathbf{Q}_{t-1} \cdot \mathbf{u}_t]\mathbf{u}_t^*. \tag{7.9}$$

Similarly, considering n_T parallel RLS adaptations for each row, and this time using instantaneous approximations for the necessary correlation matrices in a Newton recursion (see [34]), we get:

$$\begin{aligned} \mathbf{q}_i(t) &= \mathbf{q}_i(t-1) + \left[\hat{x}^{(i)}_{t-\Delta} - \mathbf{q}_i(t-1) \cdot \mathbf{u}_t\right] \mathbf{u}_t^* P_t, \\ & \quad \text{for } i = 1, \dots, n_T, \quad \text{with :} \\ P_t &= \lambda^{-1} \cdot \left[P_{t-1} - \frac{\lambda^{-1} P_{t-1}\mathbf{u}_t\mathbf{u}_t^* P_{t-1}}{1 + \lambda^{-1}\mathbf{u}_t^* P_{t-1}\mathbf{u}_t}\right] \end{aligned}$$

which, again, can be combined into one matrix recursion for $\mathbf{Q}_t$:

$$\text{MIMO RLS: } \begin{array}{c} \mathbf{Q}_t = \mathbf{Q}_{t-1} + [\hat{\mathbf{x}}_{t-\Delta} - \mathbf{Q}_{t-1} \cdot \mathbf{u}_t]\, \mathbf{u}_t^* P_t \\ P_t = \lambda^{-1} \cdot \left[P_{t-1} - \dfrac{\lambda^{-1} P_{t-1}\mathbf{u}_t\mathbf{u}_t^* P_{t-1}}{1 + \lambda^{-1}\mathbf{u}_t^* P_{t-1}\mathbf{u}_t}\right] \end{array} \tag{7.10}$$

with initial condition $P_{-1} = \pi_o \mathbf{I}$ and $0 \ll \lambda \leq 1$.

Note that the recursive adaptation of (7.10) above is known to not only be an approximation to Newton's method with instantaneous values in the places of unknown auto- and cross-correlations, but also to be the exact solution of a weighted, regularized least-squares problem involving a block of observations and a single equalizer matrix $\mathbf{Q}$. In fact, with the obvious changes to accommodate the different dimensions of $\mathbf{Q}$, the RLS recursion of (7.10) with the update for P_t coming first, can easily be shown to be exactly equivalent to the more compact RLS recursions given in [34, Chap. 10] and [51, p. 569], with the update for P_t after the equalizer update:

$$\text{MIMO RLS (II):}\quad \begin{aligned} \gamma(t) &= \frac{1}{1+\lambda^{-1}\mathbf{u}_t^* P_{t-1}\mathbf{u}_t} \\ g_t &= \lambda^{-1}\mathbf{u}_t^* P_{t-1}\gamma(t) \\ \mathbf{Q}_t &= \mathbf{Q}_{t-1} + [\hat{\mathbf{x}}_{t-\Delta} - \mathbf{Q}_{t-1}\cdot\mathbf{u}_t]\cdot g_t \\ P_t &= \lambda^{-1}\cdot[P_{t-1} - P_{t-1}\mathbf{u}_t g_t] \end{aligned} \tag{7.11}$$

7.3 Simulation results

In all simulations presented in this section we implemented the Kalman-aided MIMO DFE algorithm outlined in section 7.1 and compared the performance of the system, as measured by its symbol error rate (SER) when transmitting 4-PSK constellation points through $(2,2)$ and single-user (i.e. $(1,1)$) Ricean fading channels. We assumed the channel mean to be known at the beginning of each block of N symbols per user and tracked with the Kalman filter thereafter. For comparison purposes the plots include (dashed lines) the SER performance with the receiver having access to “genie-provided” perfect channel information, as well as that of conventional adaptive receiver algorithms, such as the LMS and RLS of section 7.2, admittedly less computationally intensive than the tracking algorithm proposed in this chapter.

The SNR is set to be the same for both users (worst-case scenario, because having one user stronger than others facilitates decoding of *every* user). Also, all $n_T n_R$ mean interfering channels of (6.2) are normalized $||\bar{\mathbf{c}}^{(i,j)}||^2 = 1$, and all ratios K_k are chosen equal to a single K. Thus, with σ_v^2 being the noise variance at each receiver, the SNR plotted is the SNR of each interfering channel, neglecting co-channel interference:

$$\text{SNR} = 10\log\frac{1+10^{K/10}}{\sigma_v^2}, \tag{7.12}$$

since the input 4-PSK points are normalized to unit power. Clearly, for the $(2,2)$ example, the above definition of SNR corresponds to 3 dB higher SNR (i.e. $10\log n_T$)

than that defined in space-time systems (see [2]), because we allocate unit power to each transmitter antenna, thinking about individual uncoordinated users. For coordinated transmission, to maintain a fair comparison with conventional $(1,1)$ systems, input power must be split evenly among the n_T transmitter antennas, which lowers the SNR by $10 \log n_T$ dB.

In Fig. 7.3 the mean channels were the normalized versions of $(1+j)[1\ 0.8]$ and $(1+j)[1\ 0.3]$ for the direct paths, and $(1+j)[1\ \ -0.8]$ and $(1+j)[1\ \ -0.5]$ for the interfering paths, the Doppler rate was $f_D T = 0.01$ (resulting in an AR(1) coefficient $f = 0.999$) and the specular-to-diffuse power ratio was $K = 6$ dB. The indicated symbol-error rate (SER) performance represents unsupervised channel tracking for long blocks of $N = 5000$ symbols per user. The proposed Kalman-aided DFE performs less than 1 dB from perfect channel knowledge, while LMS adaptive DFE fails completely with such long blocklength. In Fig. 7.4 we kept the same *mean* $(2,2)$ channel, but increased the speed of variation ($f = 0.99$, resulting from $f_D T = 0.032$), set $K = 10$ dB, and reduced N to 500. Performance is generally better (for LMS as well), and still the proposed algorithm outperforms LMS adaptation of the DFE. In both cases, the DFE has $N_f = 3$ and $N_b = 1$ matrix taps, and $\Delta = 2$.

Figures 7.5 and 7.6 show simulation results for a $(1,1)$ system with mean channel $(1+j)[1\ \ \ 2.5]$, $K = 10$ dB for both taps, and a DFE with $\Delta = 5$, and $N_f = 7$ and $N_b = 1$ scalar taps. In both figures the Doppler rate is $f_D T = 0.01$. However, in Fig. 7.5 the channel is indeed the AR(1) model with $f = 0.999$ (derived from $f_D T = 0.01$), while in Fig. 7.6 the channel is in fact generated according to Bello's model with the statistics described in (6.4), and is only approximated by the AR model of (7.1) with $f = 0.999$. As expected, the Kalman-aided DFE performs better when the channel is truly AR(1), as modeled by the receiver.

In both Fig. 7.5 and 7.6 we observe that the proposed Kalman-aided DFE outper-

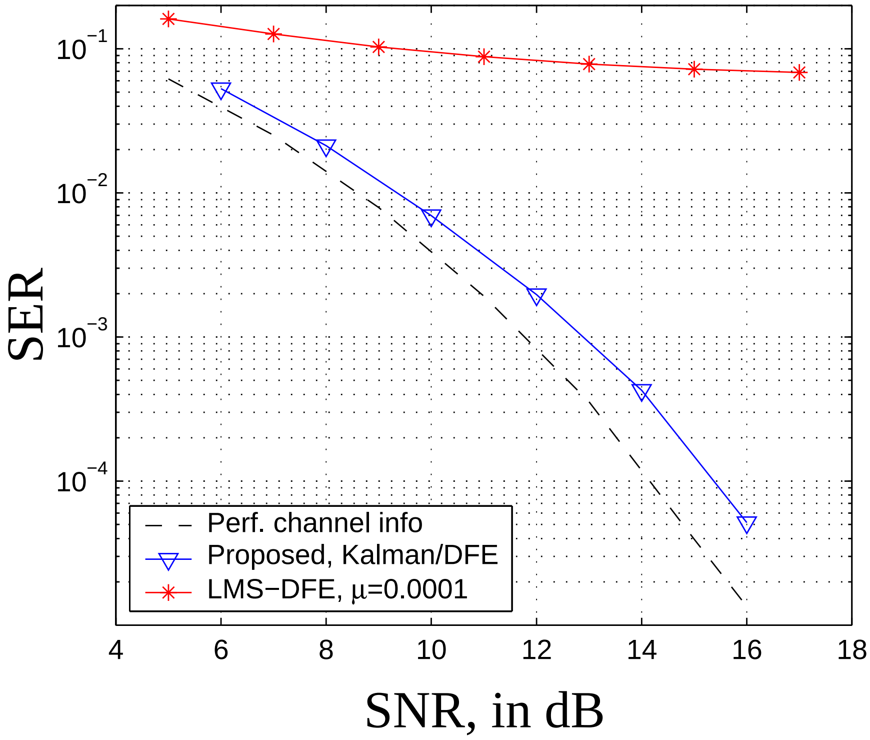

Figure 7.3: Performance of $(2, 2)$ system vs. SNR. Blocklength $N = 5000$, channel derived from $f_D T = 0.01$, $K = 6$ dB. RLS performance is very bad for such long blocks and is not shown.

forms conventional LMS/RLS adaptive algorithms. It is perhaps surprising that the superiority of the proposed algorithm is more pronounced in the second case (Fig. 7.6), where the AR(1) model is an approximation of the true channel. In that case, the Kalman-aided MIMO DFE provides much better results than plain LMS/RLS adaptations, which do not have an explicit mechanism of incorporating known channel statistics, and only rely on careful selection of the parameters μ and λ to perform the best tracking they can. So, exploiting the knowledge of largely invariant channel parameters (i.e. the mean and Doppler) to form a first-order autoregressive model for the channel offers a significant performance improvement, while in Fig. 7.5 the small gains with respect to LMS/RLS probably do not justify the higher complexity of

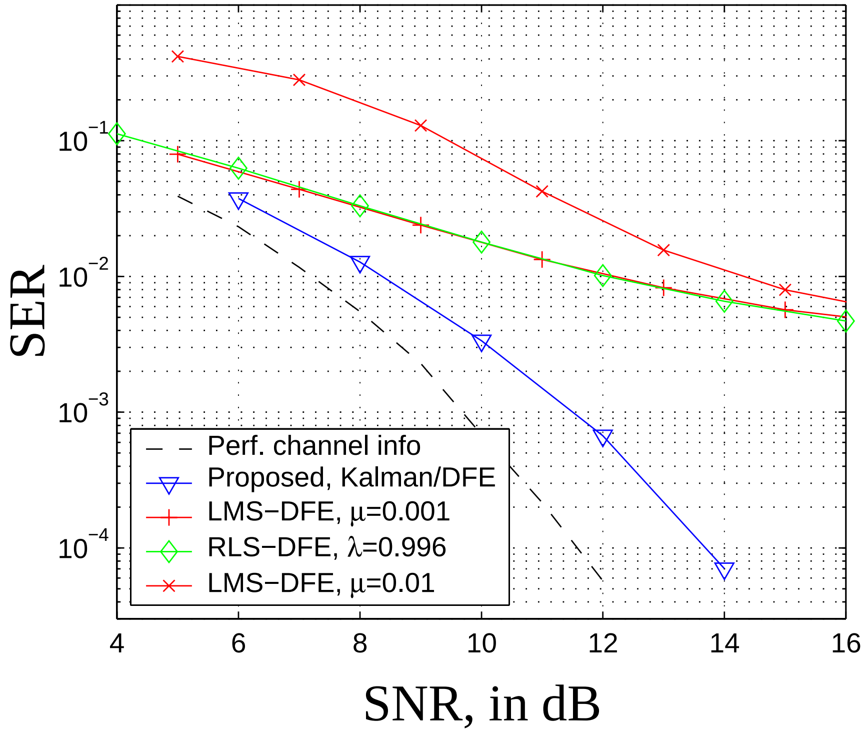

Figure 7.4: Performance of $(2,2)$ system vs. SNR. Blocklength $N = 500$, channel derived from $f_D T = 0.032$, $K = 10$ dB. Both LMS and RLS exhibit similar tracking performance, much worse than the Kalman filter.

Kalman tracking.

The simulation results in Fig. 7.7 provide some insight on the issue of how the magnitude and speed of the channel variation affect the system performance. Again, we control the rate of variation by the Doppler, and thus by the selection of parameter $f = \mathcal{J}_o\,(2\pi f_D T)$ in the model of (6.11), and the magnitude of variation with respect to the channel mean by the Ricean factor K of (6.12). Fig. 7.7 shows the SNR required for the system to reach a symbol error rate (SER) of 10^{-3} for given pairs of the abscissa K and the Doppler. We observe the intuitively obvious fact that as K decreases and the Doppler rate $f_D T$ increases, the problem becomes harder, and more SNR is required

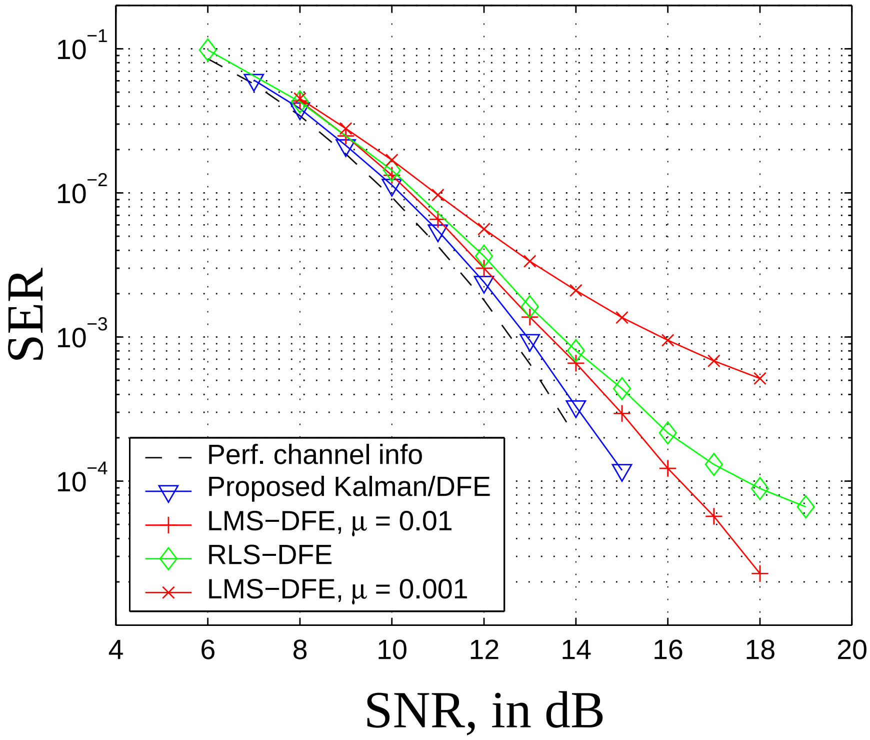

Figure 7.5: Performance of $(1, 1)$ system vs. SNR. Blocklength $N = 500$, on AR(1) channel derived from $f_D T = 0.01$. $K = 10$ dB.

for 10^{-3} performance. Also, for a given Doppler, reducing K causes an error floor and SER $= 10^{-3}$ is never achieved, no matter how high the SNR. The situation is much worse with the adaptive algorithms RLS and LMS, whose corresponding curves are not included for clarity.

Furthermore, we observe that the same conclusions are true when the Kalman filter is simulated with *correct* decisions (dashed curves in Fig. 7.7), rather than decisions from the MIMO DFE (solid curves). This proves that the problematic performance in channels with small mean (e.g. Rayleigh channel taps, whereby $K = -\infty$) coupled with rapid variation (high $f_D T$, small coefficients f) is not due to failure of the DFE, meaning increased error propagation. In fact, idealized simulations in which the DFE

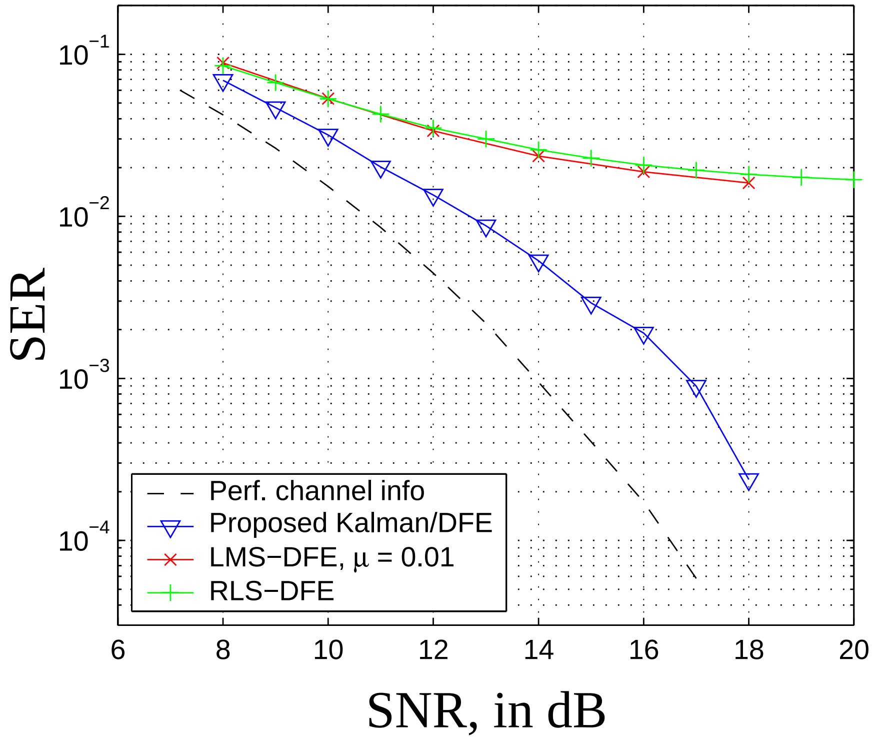

Figure 7.6: Performance of $(1, 1)$ system vs. SNR, in real Ricean channel with $f_D T = 0.01$ and $K = 10$ dB. Blocklength $N = 200$.

is provided with perfect channel knowledge show good equalization performance regardless of the speed (large $f_D T$) and magnitude (low K) of the channel variation. This confirms that the MIMO DFE is an efficient equalization mechanism, as long as correct channel estimates are available.

Rather, what fails under the harsh conditions of low-K/high-Doppler is the Kalman tracking. This Kalman tracking failure for rapid channel variation does not mean that channel estimates diverge. The Kalman filter still follows the true tap trajectories, only with a higher mean-squared error, high enough that the channel estimates it produces are sufficiently wrong, such that the MIMO DFE cannot equalize any more. It should be noted, however, that it takes quite violent tap fluctuation (low-K/high-$f_D T$)

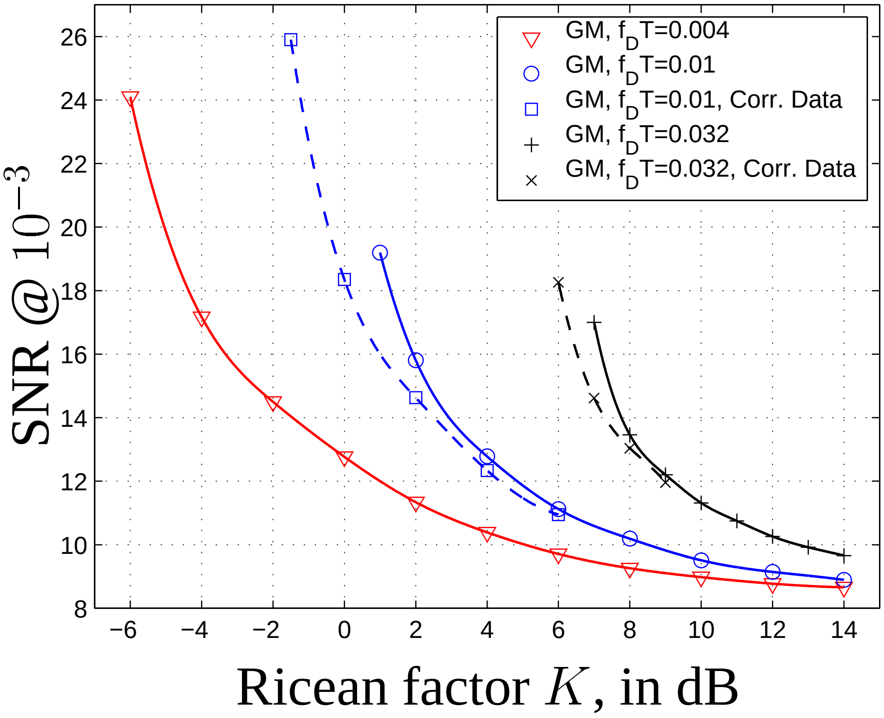

Figure 7.7: SNR required for the $(2, 2)$ system to reach SER $= 10^{-3}$ for different channel conditions, i.e. Ricean factor K and Doppler rate. The channel is time-varying according to the Gauss-Markov (GM) model of (6.11).

to cause the Kalman filter to ineffectively track the taps, while the baseline LMS/RLS adaptive algorithms exhibit high error floor for much milder channel conditions, and never outperform the Kalman filter tracking. An additional observation for perspective is that in the limit of very low K and very high $f_D T$, the channel tap values become effectively i.i.d., which makes any attempts for channel estimation futile by definition.

7.4 Coding

When the n_T transmitter antennas belong to individual, uncoordinated, yet assumed synchronous users, each of them uses a separate trellis code. Hence, the Kalman tracking ideas of section 7.1 can be used in a variety of ways, depending on available complexity and desired performance at the receiver. The simplest solution is to do hard trellis decoding for each individual user, using the decisions $\hat{x}^{(i)}$, $i = 1, \ldots, n_T$ produced by the MIMO DFE. A better approach is to use the soft values $\tilde{x}^{(i)}$, $i = 1, \ldots, n_T$ before the slicers in Fig. 7.2 as input to n_T independent soft trellis decoders, while of course continuing to provide the hard decisions $\hat{\mathbf{x}}$ to the feedback section of the DFE and the Kalman estimator.

Both the above methods however would suffer from error propagation, because the DFE produces errors in bursts that can defeat the error correcting capabilities of the individual trellis codes. If the system can tolerate the added latency, one way to overcome the bursty errors from the DFE is to introduce interleaving of the outputs of each encoder at the transmitters, and the corresponding deinterleaving operations on each of the n_T streams of soft values prior to the n_T decoders at the receiver [52]. A good way to get around this problem without added latency, but with increased receiver complexity is per-survivor processing (PSP, see [53]), whereby there is one combination of Kalman filter and MIMO DFE for every combination of survivor paths between the n_T independent trellis decoders. Specifically, if we keep s survivor paths for every trellis decoder, the number of necessary Kalman/DFE combinations is s^{n_T}, and each of those functions in the way described in section 7.1. The simple solution with a single Kalman/DFE followed by n_T soft trellis decoders mentioned above is a special case of this last arrangement, with $s = 1$ survivor path kept per user.

In the case of a single user with n_T transmitter and $n_R = n_T$ receiver antennas for increased data rate, the correct choice of a coding scheme to fit with the channel tracking and equalization mechanism discussed in section 7.1 is not obvious. If the channel were to remain constant for the whole block, and if we could assume perfect cancellation of ISI and CCI, then the effective vector channel $\mathbf{x} \rightarrow \tilde{\mathbf{x}}$ could be thought of as n_T parallel channels, each with different SNR. Thus, a 1-dimensional trellis code, coding *across* transmitter antennas would encounter a periodically time-varying channel, as noticed for the layered interference cancellation scheme in [48]. Good trellis codes for periodic channels have been designed in [54] and [55]. However, this is not the case, since the MIMO channel is neither constant nor perfectly known, and ISI and CCI cannot be perfectly cancelled. The finite MIMO DFE of section 7.1.2 precludes this by definition. Hence, a periodic code optimized for PECL and PPD (see [54]) is a suboptimal choice, as confirmed from the coded simulation results marked with "□" in Fig. 7.8. Such a code might provide better performance if the MIMO DFE is designed for successive interference cancellation, as described in [44].

To take into account the time variation of the effective channel $\mathbf{x} \rightarrow \tilde{\mathbf{x}}$ with a 1-D code, we chose to optimize this code for diversity. Namely, for the given 4-PSK modulation and 8 code states, we performed an exhaustive search over all rate-1/2 codes aimed at maximizing the effective code length (ECL, often referred to as the minimum time-diversity of the code) and the product distance (PD). The best such code is described by the polynomials $g_1(D) = 1 + D + D^2$, $g_2(D) = 1 + D^2 + D^3$ and has ECL $= 4$ and PD $= 64$ for a Gray-labeled 4-PSK constellation with unit power. The curve marked with "$\diamond$" in Fig. 7.8 shows its BER performance with an 8-state Viterbi decoder of traceback depth 14 (the same as for the periodic 1-D code optimized for PECL and PPD above), fed by the soft equalized values prior to the DFE slicers.

Clearly, both 1-D trellis codes provide a big coding gain with respect to the raw error rate at the slicers, although many important details have been ignored at decoding, such as the time-correlation of the noise after the matrix feedforward filter. The diversity code performs better than the code optimized for periodic channels.

As shown in Fig. 7.8 it is possible to do better than both the 1-D trellis codes

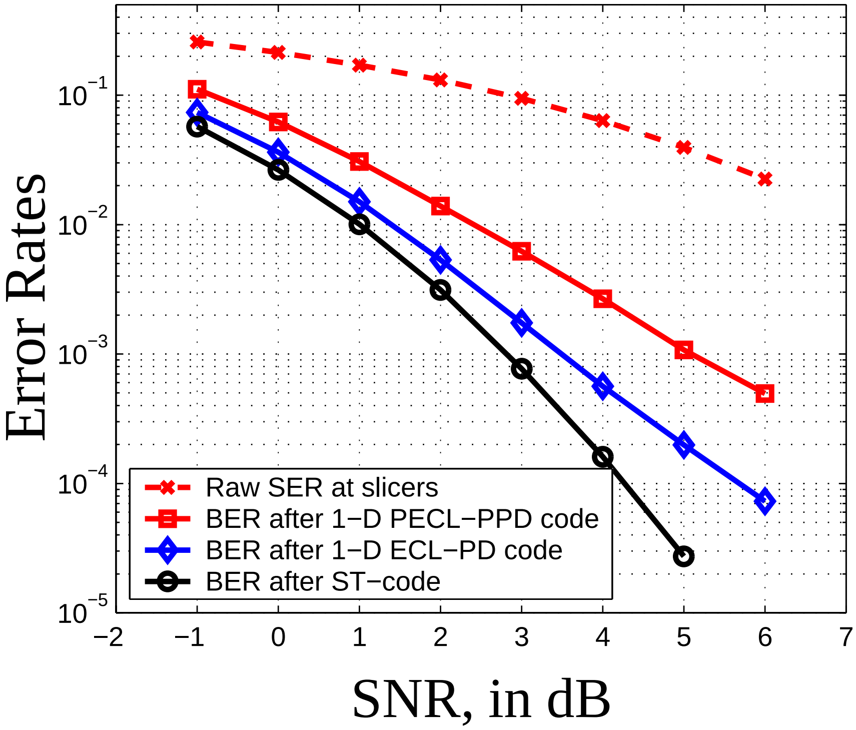

Figure 7.8: BER performance for the $(2, 2)$ system with three different codes with 8 states (the best periodic code, the best diversity code and the best space-time code), using the soft values prior to the DFE slicers. The channel remains the same as in section 7.3, with Ricean factor $K = 10$ dB, and Doppler rate $f_D T = 0.01$. Similar results are obtained with different parameters.

discussed above, by using a space-time code [37]. To realize this, recall from the discussion in section 7.1.2 that the error vector $\mathbf{e} = \tilde{\mathbf{x}} - \mathbf{x}$ prior to the slicers remains correlated with a correlation matrix $\mathbf{R}_{ee}$, which is provided by the DFE design algorithm. Even if we disregard the (small) correlation of this error vector in *time*, the correlation across the n_T interfering channels indicated by the non-zero off-diagonal elements of $\mathbf{R}_{ee}$ suggests that residual CCI exists after the MIMO equalizer. In other words, the proposed Kalman-aided MIMO DFE has not turned the effective channel

$\mathbf{x} \to \tilde{\mathbf{x}}$ into n_T non-interfering parallel channels, in which case the use of an appropriate 1-D trellis code would be a good choice.

Instead, the vector channel $\mathbf{x} \to \tilde{\mathbf{x}}$ has been turned into a “flat” MIMO channel, having CCI but mostly devoid of ISI and cross-ISI. Thus, the 8-state space-time code designed in [37] (see Fig. 5(a) there) is the best coding choice, as shown by the simulation in Fig. 7.8. For comparison with equal complexity with the 1-D codes above, we kept the traceback depth of the vector Viterbi decoder to 7, since in this case every trellis step corresponds to two steps of each 1-D code.

A final note concerns the decoding metric for the Viterbi decoder in both situations (1-D codes and space-time code). Since we are aware of the correlation across transmitted symbols, the correct metric for assumed transmitted vector $\mathbf{x}_k$ and “received” equalized vector $\tilde{\mathbf{x}}$ is not $||\tilde{\mathbf{x}} - \mathbf{x}_k||^2$. Rather, it is expressed by:

$$M(k) = (\tilde{\mathbf{x}} - \mathbf{x}_k)^* \mathbf{R}_{ee}^{-1} (\tilde{\mathbf{x}} - \mathbf{x}_k), \tag{7.13}$$

where $\mathbf{R}_{ee}$ is the error vector correlation matrix, which is provided as a by-product of the MIMO DFE design. The computation of the metric of (7.13) was implemented for both the space-time trellis decoder and the two 1-D trellis decoders. In the latter case one just needs to combine two trellis steps in one, effectively producing a rate-$2/4$ trellis code, transmitting two 4-PSK symbols at a time, very similar to the space-time code. Since essentially the same decoding is implemented, it is clear that the improved BER performance of the space-time code has to do solely with its ability to combat residual interference more effectively than the 1-D codes, which are encoding across transmitter antennas. This is not surprising, because the 1-D trellis codes were designed to provide diversity (periodic or not, respectively) and were not intended to overcome the coupling of interfering streams of data like the space-time code.

7.5 Conclusions

This second part of the dissertation (Chapters 6 and 7) discussed a receiver structure to track and equalize a MIMO frequency selective fading channel. A Kalman filter was used for tracking the channel, and an MMSE DFE, optimized for decision delay $\Delta \geq 0$ to equalize the channel and suppress CCI. The time gap between channel estimates produced by the Kalman filter and those needed for the DFE adaptation was bridged by using a simple prediction module. This algorithm, in exchange for larger complexity when compared to simple LMS/RLS updates of the DFE, offers improved performance and good tracking behavior for long unsupervised blocks, close to the performance of the idealistic case where perfect channel information is available at the receiver. Additionally, appropriate trellis coding options compatible with this method for tracking and equalization were discussed.

CHAPTER 8

Conclusions and Future Work

This dissertation presented algorithms to estimate fading in a wireless channel, while simultaneously decoding a turbo-code in flat fading (first part) or equalizing a MIMO frequency-selective channel (second part).

Turbo-decoding in flat and frequency selective fading, without assuming prior knowledge of the channel, has recently attracted the attention of researchers as wireless applications become more dominant and processing capabilities of receivers increase. Some examples are the work in [56] proposing adaptive SISO decoders, differential detection in [57], which deteriorates at high Doppler, as well as the research in [21] and [20], which is similar to the iterative Wiener filtering approach in Chapter 5 of this dissertation.

Areas for future research include performance in conjunction with complexity, taking into account implementation issues such as fixed point arithmetic in digital signal processors and timing jitter. Further research should also explore accurate capacity computation for the fading models discussed in Chapter 3, with nonzero autocorrelation for infinite lag. Research attempts in this domain include the capacity of finite-state Markov channels in [29], which is computationally cumbersome and still only an approximation, the bounds derived here in Chapter 4, as well as work in [27] for other correlation models, and [58] in a more general setting. Computing channel capacity corresponding to different algorithms of channel acquisition will provide an absolute measure for performance evaluation in any Doppler rate and SNR operation point.

For the problem of achieving reliable communication in a MIMO time-varying frequency-selective channel, treated in the second part of this dissertation, the research effort has been increasing in the past few years, as the market demands ever higher data rates in a difficult wireless environment. This dissertation presents an algorithm for channel tracking and equalization based on Kalman filtering and a MIMO MMSE DFE of finite length, but a number of issues remain open. For instance, initial training of the MIMO equalizer (before going into tracking mode) discussed in [59], is a significant area for further research. But more importantly, code design must be done for MIMO systems such that the code is compatible with the signal processing strategy for interference avoidance and cancellation, see [60] and [61, 62] and [48], seeking a code that will help approach the vast capacities promised in [2]. Significant research contributions in this domain are the space-time codes of [37], as well as the work in [63] and the combination of space and time diversity in [64], but much remains to be done, particularly if the great error-correcting potential of turbo-codes is also to be exploited in the MIMO environment.

On a different note, as signaling rates inevitably increase, the inter-symbol interference in the channel becomes more severe, and then equalization is no longer a practical solution, because of the overhead associated with training long complex equalizers (e.g. a MIMO DFE). In this case, the signaling paradigm of MIMO multicarrier modulation as in [65] is probably more appropriate, since it provides more natural coding options that can approach capacity. Besides, the channel then becomes flat (viewed in the frequency domain), which facilitates both estimation and equalization, apart from the positive impact on the design of an appropriate channel coding scheme.

APPENDIX A

Estimation from Pilot Symbols

Let a sequence $\{x_t\}$ of multiplexed coded data and known pilot symbols be transmitted in a flat Rayleigh fading channel. Then, the observed sequence is $y_t = a_t \cdot x_t + n_t$, where x_t is a pilot (a known symbol) if $t \mod (D + Z) < Z$, and an unknown coded symbol if $t \mod (D + Z) \geq Z$. This arrangement assumes that the transmitter sends frames of D consecutive coded symbols between frames of Z consecutive pilot symbols, and in this dissertation all symbols come from a PSK constellation and thus have unit energy.

The purpose of an optimum (in the minimum mean-square sense) pilot-only filter (POF) at the receiver is to operate on the observations corresponding to pilots and render optimum channel estimates $\hat{a}_k$, $k = 0, 1, \ldots, D-1$ for the times t corresponding to unknown transmitted data. If the one-sided length of the POF is L_0 pilot slots (therefore a total of $2L_0Z$ pilot symbols), then there are D distinct optimum POFs W_k^o, $k = 0, 1, \ldots, D-1$, each operating on L_0Z symbols on both sides of the channel estimate for time k. In fact, due to symmetry in time, these D POFs (horizontal vectors) W_k^o, $k = 0, 1, \ldots, D-1$ are mirrored versions of each other for indices k that are equidistant from 0 and $D-1$.

Since only observations coming from pilot symbols are going to be filtered, we can equally well filter the *derotated* versions $\tilde{y}$ of the pilot symbols, after the effect of the pilot x has been removed, namely:

$$\tilde{y} = a + \tilde{n}. \tag{A.1}$$

Observe that since pilots have unit energy, this derotation does not affect the noise statistics, so $\tilde{n}$ are still i.i.d. complex Gaussian random variables with variance σ^2 per dimension.

Collecting all the relevant derotated observations $\tilde{y}$ in a column vector $\tilde{\mathbf{y}}$ of length $2L_0Z$, the problem is to optimally estimate a_k, $k = 0, 1, \ldots, D-1$ from $\tilde{\mathbf{y}} = \mathbf{a} + \tilde{\mathbf{n}}$. Fig. A.1 gives an example of a received stream, and the pilot-filtering operation for $D = 5$, $Z = 3$, $L_0 = 2$. Note that in this appendix we ignore the "edge-effects" that occur when the channel coefficients to be estimated are located close to the edges of a block of data, where the receiver might not have access to L_0 pilot slots on either side of the desired channel coefficient. In other words, the derivations below require L_0 pilot slots (of Z symbols each) on either side of the frame of D coded data symbols, for which the channel gains a_k, $k = 0, 1, \ldots, D-1$ are being estimated. The special cases that occur when fewer than L_0 pilot slots exist on one side are straightforward to obtain.

From linear estimation theory it is well-known that since the complex vectors $\mathbf{a}$, $\tilde{\mathbf{n}}$ and $\tilde{\mathbf{y}}$ are zero-mean, the optimum linear estimator of the scalar a_k (and also the optimum estimator when nonlinear estimators are considered, since all variables are complex Gaussian) is:

$$W_k^o = Ea_k\tilde{y}^* \cdot \left[E\tilde{y}\tilde{y}^*\right]^{-1} = R_{a_k,\tilde{y}} \cdot R_{\tilde{y}}^{-1}, \quad k = 0, 1, \ldots, D-1 \tag{A.2}$$

where $R_{a_k,\tilde{y}}$ is a horizontal vector of length $2L_0Z$ with entries:

$$R_{a_k,\tilde{y}}(i) = \mathcal{J}_o\left(2\pi f_D T \cdot \text{index}(i,k)\right), \tag{A.3}$$

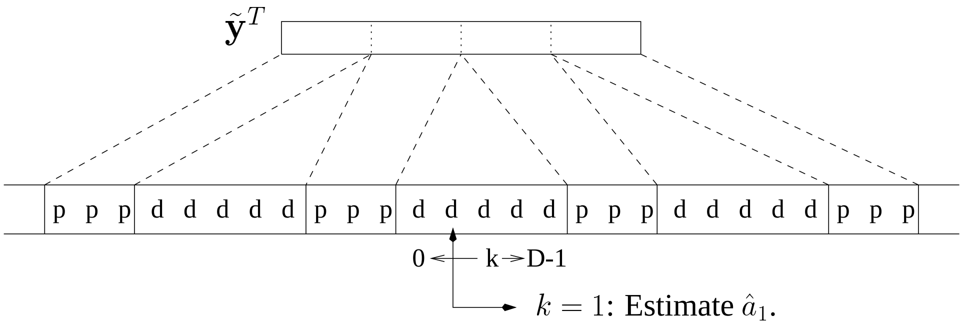
$\tilde{\mathbf{y}}^T$
p p p d d d d d p p p d d d d d p p p d d d d d p p p
0 ← k → D-1
$k = 1$: Estimate $\hat{a}_1$.

Figure A.1: Collection of the derotated observables corresponding to pilots into the vector $\tilde{\mathbf{y}}$ for $D = 5$, $Z = 3$, $L_0 = 2$. "p" denotes observation corresponding to a pilot symbol, while "d" denotes an observation due to a coded data symbol. The optimum filters W_k^o, $k = 0, 1, \ldots, D-1$, operate on $\tilde{\mathbf{y}}$ to estimate a_k, $k = 0, 1, \ldots, D-1$.

where $\mathcal{J}_o(\cdot)$ is the zero-order modified Bessel function of the first kind and

$$\text{index}(i,k) = \begin{cases} (L_0 - \lfloor i/Z \rfloor - 1) \cdot D + (L_0 Z - i) + k, & 0 \le i < L_0 Z \\ (\lfloor i/Z \rfloor - L_0) \cdot D + (i - L_0 Z) + D - k, & L_0 Z \le i < 2L_0 Z \end{cases} \tag{A.4}$$

The covariance matrix of the vector $\tilde{\mathbf{y}}$ is:

$$R_{\tilde{y}} = R_a + 2\sigma^2 \mathbf{I}_{2L_0 Z}, \tag{A.5}$$

where the matrix $R_a = E\mathbf{a}\mathbf{a}^*$ is symmetric but not Toeplitz, since the symbols corresponding to the fading coefficients inside the vector $\mathbf{a}$ were not necessarily adjacent in the initial data stream. The entries of the matrix R_a are:

$$R_a(i,j) = \mathcal{J}_o\left(2\pi f_D T \cdot [D \cdot |\lfloor i/Z \rfloor - \lfloor j/Z \rfloor| + |i-j|]\right), \quad i,j = 0, \ldots, 2L_0 Z - 1. \tag{A.6}$$

To verify the non-Toeplitz structure of the matrix R_a, observe that:

$$R_a(0,2) = \mathcal{J}_o\left(2\pi f_D T \cdot 2\right) \neq \mathcal{J}_o\left(2\pi f_D T \cdot (D+2)\right) = R_a(1,3). \tag{A.7}$$

From (A.2) and using (A.3)–(A.6) it is straightforward to compute the D distinct optimum POFs W_k^o, each of which provides the estimates:

$$\hat{a}_k = W_k^o \cdot \tilde{\mathbf{y}}, \quad k = 0, 1, \ldots, D-1. \tag{A.8}$$

The minimum mean-squared error (m.m.s.e.) of the estimation is (see, for instance, [34]):

$$\begin{aligned} E|\tilde{a}_k|^2 &\overset{\mathrm{def}}{=} E|a_k - \hat{a}_k|^2 && \text{(A.9)} \\ &= 1 - R_{a_k,\tilde{y}} R_y^{-1} R_{a_k,\tilde{y}}^* && \text{(A.10)} \\ &= 1 - W_k^o \left(R_a + \mathbf{I}_{2L_0Z}\right)(W_k^o)^*, && \text{(A.11)} \end{aligned}$$

and the average m.m.s.e. due to estimation from pilots can be obtained:

$$\text{MSE} = \sum_{k=0}^{D-1} E|\tilde{a}_k|^2, \tag{A.12}$$

which is the quantity plotted against SNR in Fig. 3.3.

APPENDIX B

Proof of Theorem 1

This appendix contains the proof of Theorem 1. Although in section 4.2 we only use the bounds $I_{UB}(D)$ for the constrained capacity with i.i.d. 4-PSK inputs, these bounds are in fact general and also apply for any input distribution, including the capacity achieving Gaussian. For this reason, in the following proof we use the symbol $h(.)$ for the entropy of the input variable X, implying differential entropy, while for X coming from a 4-PSK constellation the symbol $H(.)$ for the entropy of a discrete random variable is more appropriate. We first show that the sequence $I_{UB}(D)$, $D = 0, 1, 2, \dots, \infty$ decreases in D, or:

$$
\begin{aligned}
& I_{UB}(D) \geq I_{UB}(D+1) \\
\iff \quad & \frac{1}{D} \cdot \left[h\left(X_1^D \mid Q_0, Q_{D+1}\right) - h\left(X_1^D \mid Q_0, Y_1^D, Q_{D+1}\right)\right] \geq \qquad \text{(B.1)} \\
& \frac{1}{D+1} \cdot \left[h\left(X_1^{D+1} \mid Q_0, Q_{D+2}\right) - h\left(X_1^{D+1} \mid Q_0, Y_1^{D+1}, Q_{D+2}\right)\right] \\
\iff \quad & \frac{1}{D} \cdot h\left(X_1^D \mid Q_0, Y_1^D, Q_{D+1}\right) \leq \qquad \text{(B.2)} \\
& \frac{1}{D+1} \cdot h\left(X_1^{D+1} \mid Q_0, Y_1^{D+1}, Q_{D+2}\right) \\
\iff \quad & \frac{1}{D} \cdot \sum_{i=1}^{D} h\left(X_i \mid Q_0, X_1^{i-1}, Y_1^D, Q_{D+1}\right) \leq \qquad \text{(B.3)} \\
& \frac{1}{D+1} \cdot \sum_{i=1}^{D+1} h\left(X_i \mid Q_0, X_1^{i-1}, Y_1^{D+1}, Q_{D+2}\right)
\end{aligned}
$$

where (B.1) is the definition of mutual information, (B.2) follows from the fact that the input X is i.i.d. and independent of all the channel states Q, while (B.3) is the chain rule for entropy. Now observe two facts, which hold for $i = 1, \dots, D$:

$$h\left(X_i \mid Q_0, X_1^{i-1}, Y_1^D, Q_{D+1}\right) \leq h\left(X_i \mid Q_0, X_1^{i-1}, Y_1^{D+1}, Q_{D+2}\right) \tag{B.4}$$

because conditioning reduces entropy, and also:

$$\begin{aligned} h\left(X_i \mid Q_0, X_1^{i-1}, Y_1^D, Q_{D+1}\right) &= h\left(X_{i+1} \mid Q_1, X_2^i, Y_2^{D+1}, Q_{D+2}\right) \\ &\leq h\left(X_{i+1} \mid Q_0, X_1^i, Y_1^{D+1}, Q_{D+2}\right) \end{aligned} \tag{B.5}$$

by stationarity and the fact that conditioning reduces entropy. Therefore, if we denote the terms of the sums in the LHS and RHS of (B.3) $l_i, i = 1, \dots, D$ and $r_i, i = 1, \dots, D+1$ respectively for notational convenience, then (B.4) implies $l_i \leq r_i, i = 1, \dots, D$ and (B.5) implies $l_i \leq r_{i+1}, i = 1, \dots, D$. So, assuming $r_{\max} = r_k$, we have:

$$\begin{aligned} \frac{1}{D} \cdot \sum_{i=1}^{D} l_i &= \frac{1}{D+1} \cdot \left[\frac{1}{D}\sum_{i=1}^{D} l_i + D \cdot \left(\frac{1}{D}\sum_{i=1}^{D} l_i\right)\right] \\ &\leq \frac{1}{D+1} \cdot \left[r_{\max} + D \cdot \left(\frac{1}{D}\sum_{i=1, i\neq k}^{D+1} r_i\right)\right] \qquad \text{(B.6)} \\ &= \frac{1}{D+1} \cdot \sum_{i=1}^{D+1} r_i \qquad \text{(B.7)} \end{aligned}$$

where (B.6) follows from (B.4) and (B.5). This proves (B.3) and with it the claim that $I_{UB}(D)$ is decreasing in D. Also, $I_{UB}(D)$ is non-negative, hence it has a limit. We now show that this limit is, in fact, C_{FSMC}, or in other words that the bound $I_{UB}(D)$, $D = 0, 1, 2, \dots$ is asymptotically tight.

$$\begin{aligned} &\frac{1}{D} \cdot I\left(X_1^D; Y_1^D \mid Q_0, Q_{D+1}\right) - \frac{1}{D} \cdot I\left(X_1^D; Y_1^D\right) = \\ &\quad = \frac{1}{D} \cdot \left[H\left(X_1^D \mid Y_1^D\right) - H\left(X_1^D \mid Y_1^D, Q_0, Q_{D+1}\right)\right] \\ &\quad = \frac{1}{D} \cdot I\left(X_1^D; Q_0, Q_{D+1} \mid Y_1^D\right) \geq 0 \end{aligned} \tag{B.8}$$

so $I_{UB}(D)$ upperbounds every term in the sequence $1/n \cdot I(X_1^n; Y_1^n)$, $n \geq D$ and hence also upperbounds C_{FSMC}, from (4.16). Finally, it is easy to see that the bounds

$I_{UB}(D)$, $D = 0, 1, 2, \ldots$ are asymptotically (in D) tight, by examining the difference term:

$$\begin{aligned}
\frac{1}{D} \cdot I\left(X_1^D; Q_0, Q_{D+1} \mid Y_1^D\right) = \qquad & \qquad\qquad\qquad\qquad\qquad\qquad\qquad\qquad\qquad\qquad\qquad\qquad\qquad\qquad \text{(B.9)} \\
= \quad & \frac{1}{D} \cdot \left[H\left(Q_0, Q_{D+1} \mid Y_1^D\right) - H\left(Q_0, Q_{D+1} \mid X_1^D, Y_1^D\right)\right] \\
\leq \quad & \frac{1}{D} \cdot H\left(Q_0, Q_{D+1} \mid Y_1^D\right) && \text{(B.10)} \\
\leq \quad & \frac{1}{D} \cdot H\left(Q_0, Q_{D+1}\right) && \text{(B.11)} \\
\leq \quad & \frac{2 \log K}{D} && \text{(B.12)}
\end{aligned}$$

which converges to zero, as D grows without bound.

REFERENCES

[1] C. Berrou, A. Glavieux, and P. Thitimajshima. Near Shannon limit error-correcting coding and decoding: Turbo-codes (1). In *ICC '93*, pages 1064–1070, 1993.

[2] G. J. Foschini and M. J. Gans. On limits of wireless communications in a fading environment when using multiple antennas. *Wireless Personal Communications*, 6:311–35, 1998.

[3] S. Benedetto and G. Montorsi. Unveiling turbo codes: Some results on parallel concatenated coding schemes. *IEEE Trans. on Inform. Theory*, 42(2):409–428, March 1996.

[4] E. K. Hall and S. G. Wilson. Design and analysis of turbo-codes on Rayleigh fading channels. *IEEE Journal on Sel. Areas in Comm.*, 16(2):160–174, Feb. 1998.

[5] C. Fragouli and R. Wesel. Symbol-interleaved parallel concatenated trellis coded modulation. *1999 IEEE Communication Theory Miniconference in conjunction with ICC 99, Vancouver, BC, Canada*, 6-10 June 1999.

[6] C. Fragouli. *Turbo-Code Design for High Spectral Efficiency*. PhD thesis, UCLA, 2000.

[7] S. Benedetto , D. Divsalar, G. Montorsi, and F. Pollara. Parallel concatenated trellis coded modulation. *IEEE International Conference on Communications, ICC 1996, Dallas, TX*, 2, June 1996.

[8] S. Benedetto , D. Divsalar, G. Montorsi, and F. Pollara. A soft-input soft-output APP module for the iterative decoding of concatenated codes. *IEEE Communications Letters*, 1(1):22–4, Jan. 1997.

[9] S. Benedetto , D. Divsalar, G. Montorsi, and F. Pollara. Soft-input soft-output modules for the construction and distributed iterative decoding of code networks. *Europ. Trans. on Telecom.*, 9(2):155–172, March-April 1998.

[10] C. Fragouli and R. Wesel. Turbo encoder design for symbol-interleaved parallel concatenated trellis coded modulation. *to appear in IEEE Transactions on Communications*, 2000.

[11] P. Robertson and T. Wörz. Bandwidth-efficient turbo trellis-coded modulation using punctured component codes. *IEEE Journal on Sel. Areas in Comm.*, 16(2):206–18, Feb. 1998.

[12] L. R. Bahl, J. Cocke, F. Jelinek, and J. Raviv. Optimal decoding of linear codes for minimizing symbol error rate. *IEEE Trans. on Inform. Theory*, 20(2):284–287, March 1974.

[13] L. E. Baum, T. Petrie, G. Soules, and N. Weiss. A maximization technique occuring in the statistical analysis of probabilistic functions of Markov chains. *Ann. Math. Stat*, 41:164–171, 1970.

[14] L. R. Rabiner and B.-H. Juang. *Fundamentals of Speech Recognition*. Prentice Hall, Englewood Cliffs, N.J., 1993.

[15] R. H. Clarke. A statistical theory of mobile radio reception. *Bell Syst. Tech. J.*, pages 957–1000, July 1968.

[16] W. C. Y. Lee. *Mobile Communications Engineering*. McGraw Hill, NY, 1982.

[17] W. C. Jakes, Jr. *Microwave Mobile Communications*. John Wiley & Sons, NY, 1974.

[18] H. S. Wang and N. Moayeri. Finite-state Markov channel: A useful model for radio communication channels. *IEEE Trans. on Veh. Tech.*, 44(1):163–171, February 1995.

[19] H. S. Wang and P. C. Chang. On verifying the first-order Markovian assumption for a Rayleigh fading channel model. *IEEE Trans. on Veh. Tech.*, 45(2):353–357, May 1996.

[20] H. J. Su and E. Geraniotis. Improved performance of a PSAM system with iterative filtering and decoding. *Thirty-Sixth Annual Allerton Conference on Communication, Control and Computing*, pages 156–166, Sept. 1998.

[21] M. C. Valenti and B. D. Woerner. Refined channel estimation for coherent detection of turbo-codes over flat fading channels. *Electronics Letters*, 34(17):1648–9, Aug. 1998.

[22] A. Papoulis. *Probability, Random Variables and Stochastic Processes, 3rd Ed.* McGraw-Hill, 1991.

[23] J. K. Cavers. An analysis of pilot symbol assisted modulation for Rayleigh fading channels. *IEEE Trans. on Veh. Tech.*, 40(4):686–693, Nov. 1991.

[24] A. G. Dabak, S. Hosur, and T. Schmidl. Iterative channel estimation for wideband CDMA systems. *Thirty-Sixth Annual Allerton Conference on Communication, Control and Computing*, pages 441–9, Sep. 1998.

[25] R. G. Gallager. *Information Theory and Reliable Communication*. New York: Wiley, 1968.

[26] L. H. Ozarow, Shlomo Shamai, and A. D. Wyner. Information theoretic considerations for cellular mobile radio. *IEEE Trans. on Veh. Tech.*, 43(2):369–378, May 1994.

[27] G. Kaplan and Shlomo Shamai. Achievable performance over the correlated Rician channel. *IEEE Trans. on Comm.*, 42(11):2967–2978, Nov. 1994.

[28] M. Mushkin and I. Bar-David. Capacity and coding for the Gilbert-Elliott channels. *IEEE Trans. on Inform. Theory*, 35(6):1277–1290, Nov. 1989.

[29] A. J. Goldsmith and P. P. Varaiya. Capacity, mutual information, and coding for finite-state Markov channels. *IEEE Trans. on Inform. Theory*, 42(3):868–886, May 1996.

[30] J. G. Proakis. *Digital Communications, Third Edition*. McGraw-Hill, 1995.

[31] R. Price and P. E. Green, Jr. A communication technique for multipath channels. *Proceed. IRE*, 46:555–70, March 1958.

[32] P. A. Bello. Performance of some RAKE modems over the nondisturbed wide band HF channel. *Proc. of 1989 IEEE Military Commun. Conf. (MIL-COM)*, pages 39.3.1–39.3.4, September 1989.

[33] G. D. Forney, Jr. and G. Ungerboeck. Modulation and coding for linear Gaussian channels. *IEEE Trans. on Inform. Theory*, 44(6):2384–2415, Oct. 1998.

[34] T. Kailath, A. H. Sayed, and B. Hassibi. *Linear Estimation*. Prentice Hall, NJ, 2000.

[35] A. Duel-Hallen. A family of multiuser decision-feedback detectors for asynchronous code-division, multiple-access channels. *IEEE Trans. on Comm.*, pages 421–34, Feb/Mar/April 1995.

[36] M. Honig, U. Madhow, and S. Verdú. Blind adaptive multiuser detection. *IEEE Trans. on Inform. Theory*, 41(4):944–60, July 1995.

[37] V. Tarokh, N. Seshadri, and A. R. Calderbank. Space-time codes for high data rate wireless communication: Performance criterion and code construction. *IEEE Trans. on Inform. Theory*, 44(2):744–65, March 1998.

[38] S. U. H. Qureshi. Adaptive equalization. *Proc. of the IEEE*, 73(9):1349–87, Sept. 1985.

[39] D. P. Taylor, G. M. Vitetta, B. D. Hart, and A. Mämmelä. Wireless channel equalisation. *Europ. Trans. on Telecom.*, 9(2):117–43, March-April 1998.

[40] C. Komninakis, C. Fragouli, A.H. Sayed, and R.D. Wesel. Channel estimation and equalization in fading. *Proc. of 33rd Asilomar Conference on Signals, Systems and Computers*, pages 1159–1163, Oct. 1999.

[41] G. Paparisto and K. M. Chugg. PSP array processing for multipath fading channels. *IEEE Trans. on Comm.*, 47(4):504–7, April 1999.

[42] S. N. Diggavi, B. C. Ng, and A. Paulraj. An interference suppression scheme with joint channel-data estimation. *IEEE Journal on Sel. Areas in Comm.*, 17(11):1924–39, Nov. 1999.

[43] Y. Li and K. J. R. Liu. Adaptive blind source separation and equalization for multiple-input/multiple-output systems. *IEEE Trans. on Inform. Theory*, 44(7):2864–76, Nov. 1998.

[44] N. Al-Dhahir and A. H. Sayed. The finite-length multi-input multi-output MMSE-DFE. *IEEE Trans. on Signal Processing*, 48(10):2921–36, Oct. 2000. (see also Proc. of 33-rd Asilomar Conference on Signals, Systems and Computers, pp. 207–209, Oct. 1999).

[45] R. A. Iltis. Joint estimation of PN code delay and multipath using extended Kalman filter. *IEEE Trans. on Comm.*, 38(10):1677–1685, Oct. 1990.

[46] S. Haykin, A. H. Sayed, J. R. Zeidler, P. Yee, and P. C. Wei. Adaptive tracking of linear time-variant systems by extended RLS algorithms. *IEEE Trans. on Signal Processing*, 45(5):1118–1128, May 1997.

[47] P. A. Bello. Characterization of randomly time-variant linear channels. *Trans. on Communication Systems*, CS(11):360–393, Dec. 1963.

[48] G. J. Foschini. Layered space-time architecture for wireless communication in a fading environment when using multi-element antennas. *Bell Labs Technical Journal*, pages 41–59, Autumn 1996.

[49] M. K. Tsatsanis, G. B. Giannakis, and G. Zhou. Estimation and equalization of fading channels with random coefficients. *Signal Processing*, 53(2-3):211–229, Sept. 1996.

[50] A. H. Sayed and T. Kailath. Extended Chandrasekhar recursions. *IEEE Trans. on Aut. Control*, 39(3):619–623, Mar. 1994.

[51] S. Haykin. *Adaptive Filter Theory, 3rd edition*. Prentice Hall, NJ, 1996.

[52] M. Vedat Eyuboğlu. Detection of coded modulation signals on linear, severely distorted channels using Decision-Feedback noise prediction with interleaving. *IEEE Trans. on Comm.*, 36(8):401–9, April 1988.

[53] R. Raheli, A. Polydoros, and C.-K. Tzou. Per-survivor processing: a general approach to MLSE in uncertain environments. *IEEE Trans. on Comm.*, 43(2-4, pt. 1):354–64, Feb.-April 1995.

[54] R. D. Wesel and J. M. Cioffi. Trellis code design for periodic interleavers. *Communications Letters*, 3(4):103–5, April 1999.

[55] R. D. Wesel, X. Liu, and W. Shi. Trellis codes for periodic erasures. *IEEE Trans. on Comm.*, 48(6):938–47, June 2000.

[56] A. Anastasopoulos and K. M. Chugg. Adaptive soft-input soft-output algorithms for iterative detection with parametric uncertainty. *IEEE Trans. on Comm.*, 48(10):1638–49, Oct. 2000.

[57] I. D. Marsland and P. T. Mathiopoulos. Multiple differential detection of parallel concatenated convolutional (turbo) codes in correlated fast Rayleigh fading. *IEEE Journal on Sel. Areas in Comm.*, 16(2):265–75, Feb. 1998.

[58] M. Medard. The effect upon channel capacity in wireless communications of perfect and imperfect knowledge of the channel. *IEEE Trans. on Inform. Theory*, 46(3):933–46, May 2000.

[59] T. L. Marzetta. BLAST training: Estimating channel characteristics for high capacity space-time wireless. *in Proc. of Thiry-Seventh Annual Allerton Conference on Communication, Control, and Computing, Monticello, IL, USA, 23-25 Sept. 1998.*, pages 431–40, 1998.

[60] V. Tarokh, A. Naguib, N. Seshadri, and A. R. Calderbank. Combined array processing and space-time coding. *IEEE Trans. on Inform. Theory*, 45(4):1121–8, May 1999.

[61] G. J. Foschini, G. D. Golden, R. A. Valenzuela, and P. W. Wolniansky. Simplified processing for high spectral efficiency wireless communication employing multi-element arrays. *IEEE Journal on Sel. Areas in Comm.*, 17(11):1841–52, Nov. 1999.

[62] P. W. Wolniansky, G. J. Foschini, G. D. Golden, and R. A. Valenzuela. V-BLAST: an architecture for realizing very high data rates over the rich-scattering wireless channel. *in Proc. of 1998 URSI International Symposium on Signals, Systems, and Electronics, Pisa, Italy, 29 Sept.-2 Oct. 1998*, pages 295–300, 1998.

[63] S. L. Ariyavisitakul. Turbo space-time processing to improve wireless channel capacity. *In proceedings of ICC 2000, N. Orleans, LA*, pages 1238–42, 18-22 June 2000.

[64] A. R. Calderbank, G. Pottie, and N. Seshadri. Cochannel interference suppression through time/space diversity. *IEEE Trans. on Inform. Theory*, 46(3):922–32, May 2000.

[65] G. G. Raleigh and J. M. Cioffi. Spatio-temporal coding for wireless communication. *IEEE Trans. on Comm.*, 46(3):357–66, March 1998.